Doctoral Dissertation

Meniscus Splitting in Polysaccharide Dispersions and Preparation of pH-Responsive Materials

NGUYEN THI KIM LOC

Supervisor: Okeyoshi Kosuke

Division of Advanced Science and Technology
Japan Advanced Institute of Science and Technology
[Materials Science]

September 2025

Referee-in-chief: Associate Professor Dr. Okeyoshi Kosuke

Japan Advanced Institute of Science and Technology

Referees:

Professor Dr. Yamaguchi Masayuki

Japan Advanced Institute of Science and Technology

Professor Dr. Matsumura Kazuaki

Japan Advanced Institute of Science and Technology

Professor Dr. Oshima Yoshifumi

Japan Advanced Institute of Science and Technology

External Referees:

Professor Dr. Miyata Takashi

Kansai University

Abstract

Biological materials are abundant in nature, forming the structural foundation of both plant and animal bodies. With the growing demand for sustainable alternatives to synthetic plastics, natural polymers have attracted increasing attention. Among these, chitosan, which is produced by the deacetylation of chitin, stands out for its excellent biocompatibility, biodegradability, and functional versatility. Although hierarchical structures such as nanofibers and twisted architectures have been extensively explored, achieving controlled anisotropic microstructures at the millimeter scale remains a significant challenge. Overcoming this limitation is essential for expanding the potential applications of chitosan in the development of sustainable materials.

In order to create a three-dimensionally organized microstructure, a chitosan network was recreated from an aqueous solution using the meniscus splitting approach. When deposited at the millimeter scale, the resultant chitosan membrane demonstrated practical anisotropic pH-responsive hydrogel characteristics. Capillary forces caused chitosan to undergo ordered deposition during the evaporation of the aqueous solution from a confined region, creating a membrane with directed microstructures and microlayers. This membrane formed between two air-liquid interfaces, as opposed to solid-liquid and air-liquid interfaces, where cast films form. Consequently, directed swelling in aqueous environments and reversible/irreversible swelling-deswelling transitions were seen in membranes with ordered microstructures, based on the pH range that is controlled. Furthermore, the evaporative interface created a non-equilibrium state for both dissolved molecules and geometrically asymmetric macrostructures, similar to crystal growth. While multiple-nuclei generation has been observed, the relative positioning of nuclei and dominant influencing factors remain unclear. This study investigates meniscus splitting with multiple nucleation events, focusing on symmetry breaking and asynchronous nucleus formation.

Keywords: polysaccharides, pH-responsive, sysmmetry breaking, evaporation, synchronous/asynchronous nucleation

Preface

This dissertation is submitted in partial fulfillment of the requirements for the degree of Doctor of Philosophy at the Japan Advanced Institute of Science and Technology (JAIST), Japan. It presents the research findings on “Meniscus splitting in polysaccharide dispersions and preparation of pH-responsive materials”. The study was conducted under the supervision of Prof. Okeyoshi Kosuke at the Graduate School of Advanced Science and Technology, JAIST, between October 2022 and September 2025.

This research presents a comprehensive comparison between theoretical predictions and experimental observations regarding the process of solvent evaporation, analyzed through computational calculations. Furthermore, it explores the formation of multiple nuclei during solvent evaporation, emphasizing the role of symmetry breaking and the asynchronous emergence of dissipative structures. The study aims to deepen the understanding of these fundamental mechanisms, which are crucial for controlling material properties in various applications, such as thin-film fabrication and polymer assembly.

The primary objective of this thesis is to investigate the three-dimensional structural organization of chitosan under drying conditions. This research explores how self-assembly mechanisms, influenced by drying parameters such as humidity, temperature, and solvent evaporation rate, contribute to the formation of hierarchical structures. Additionally, the study examines the role of environmental factors, particularly pH variations, in modulating the physicochemical properties and responsiveness of the resulting chitosan-based materials. Understanding these aspects is crucial for developing functional biomaterials with tailored properties for applications in drug delivery, wound healing, and tissue engineering. Relevant information from existing literature has been referenced appropriately throughout the text to provide context and support for the findings. To the best of the author's knowledge, this work introduces original ideas, novel experimental results, and a unique presentation approach. Furthermore, every effort has been made to ensure the integrity and authenticity of the research, with no part of this thesis being plagiarized.

Nguyen Thi Kim Loc

Graduate School of Advanced Science and Technology,
Japan Advanced Institute of Science and Technology,
September 2025

Acknowledgements

I would like to sincerely thank my supervisor, Prof. Okeyoshi Kosuke, at the Graduate School of Advanced Science and Technology, Japan Advanced Institute of Science and Technology, for granting me the opportunity to be his student. His insightful guidance, valuable suggestions, and constructive feedback played a crucial role in the successful completion of this work. His unwavering trust in my abilities served as a constant source of motivation, enabling me to remain focused throughout my research and the writing of this thesis.

Besides my advisor, I would like to express my sincere thanks to my second supervisor, Prof. Masayuki Yamaguchi, and Prof. Oshima Yoshifumi, who served as my minor research advisor. I would also like to thank the members of the review committee Prof. Yamaguchi Masayuki (JAIST), Prof. Matsumura Kazuaki (JAIST), Prof. Oshima Yoshifumi (JAIST), Miyata Takashi (Kansai University), who have spent their valuable time to read the thesis and agreed to be a part of the review committee.

Research is a demanding and enduring journey that requires a high level of technical expertise and in-depth scientific discussions. I would like to express my sincere gratitude to Prof. Matsuba Go (Yamagata University), Prof. Hara Mitsuo (Yamagata University), and Prof. Ikemoto Yuka (Japan Synchrotron Radiation Research Institute, Hyogo) for their kind support in the measurement of WAXS, SAXS, and IR, Mr. Ito Nobuaki and Ms. Kobayashi Shoko from the Center for Nano Materials and Technology (JAIST) for their invaluable guidance and assistance with SEM analysis. Additionally, I deeply appreciate all the members of the Okeyoshi Lab for their support, insightful discussions, and collaboration. Their timely contributions, teamwork during critical deadlines, and the memorable moments we shared have made this research experience truly enriching.

Lastly, I would like to express my heartfelt gratitude to my family for their unwavering support, encouragement, and positivity, especially during difficult times. I dedicate this work to my parents, whose steadfast belief in me and my ambitions has been a constant source of strength. Their trust in my abilities continues to inspire me to dream bigger and work harder toward my goals.

Nguyen Thi Kim Loc

Graduate School of Advanced Science and Technology,
Japan Advanced Institute of Science and Technology,
September 2025

Table of Contents

Chapter 1

General Introduction

1.1. Self-assembled soft matter

The term "soft matter" was first introduced to describe a wide range of materials made up of big macromolecules such as colloidal particles, polymers, and surfactants, which have the remarkable ability to spontaneously organize into structured and ordered systems without the need for external guidance. This self-organization, known as self-assembly, is one of the defining features of soft matter and is driven by a delicate balance of fundamental intermolecular forces, such as electrostatic, hydrogen bonding, hydrophobic, and van der Waals interactions. These forces, while individually weak compared to covalent bonds, collectively guide macromolecular units into complex and functional arrangements. What makes soft matter especially distinct from traditional forms of matter is that it is not composed of individual atoms or small molecules, but rather of macromolecular aggregates with spatial dimensions typically ranging from ome nanometer (nm) to one micrometer (μm). This scale allows for behavior that bridges the gap between molecular chemistry and bulk material science.

Soft matter systems exhibit unique physical properties that often do not fit neatly into the conventional definitions of solids or liquids. For example, materials like gels and foams can retain shape like solids under low stress but flow like liquids when a threshold is exceeded, displaying what is known as viscoelastic behavior. Additionally, liquid crystals, another type of soft matter, flow like a liquid but exhibit directional optical properties due to their ordered internal structure. One of the most intriguing aspects of soft matter is its responsiveness to external stimuli, this sensitivity makes soft matter ideal for an extensive range of practical applications, spanning from drug delivery systems and biological membranes to smart coatings, flexible electronics, and soft robotics. In biological systems, soft matter plays a foundational role; for instance, cell membranes, proteins, and DNA are all governed by the same principles of self-assembly and soft interactions that define this field. Because of its interdisciplinary nature, drawing from physics, chemistry, biology, and materials science, soft matter continues to be a vibrant and rapidly growing area of research, offering profound understanding of the behavior of intricate systems and enabling innovations in both industrial technology and biomedical engineering.[1]

In the context of soft matter, “soft” refers to materials that can easily change shape or deform under relatively small forces, as opposed to hard materials like metals or ceramics. Soft matter systems are often sensitive to their environment, like temperature, concentration, and external fields, which allows them to exhibit a wide range of behaviors and structures, including those that are not mechanical. While hard matter exhibits some resistance to external stress and conditioned changes like ambient temperature, light, and pressure, soft matter materials easily flow and deform in response to such external stimuli. They can change phases when deformed and can be either elastic, viscous, or both. Complex systems like soft matter exhibit a wide variety of nonlinear effects. People are interested in the study of soft matters for the same reason.

Use toothpaste as an illustration. When placed on a toothbrush, it behaves like a solid, yet when squeezed from a tube, it flows like a fluid. Because soft matter contains a wide variety of characteristics that fall midway between those of solids and liquids, it is challenging to define precisely. Soft matter can take on numerous forms due to these characteristics. Surfactants, liquid crystals, colloids, foams, and polymer solutions are examples of typical materials classified as "soft materials". Liquid crystals are ordered soft materials made up of self-organized molecules that may be utilized as novel functional materials for bioactive, catalytic, optical, sensory, and electron, ion, or molecular transport. They can be found in a variety of commonplace items, including tofu, milk, and yogurt, as well as paints, soaps, and fabrics (**Fig. 1.1**), except for strong structures like bones and teeth.

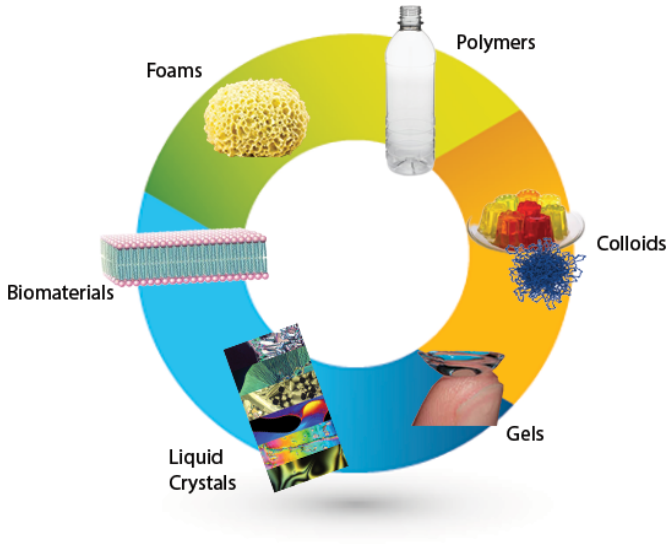

Figgure 1.1. Soft matter example.[1]

When molecules or pre-synthesised nanoparticles spontaneously assemble into highly ordered structures via non-covalent interactions, this is referred to as self-assembly. There are five widely recognized principles that define self-assembly. First, molecular recognition is crucial, requiring specific interactions between molecules or structures to generate organized patterns. Second, self-assembly depends on a delicate balance of attractive and repulsive forces, which are generally weak but essential for stability. Third, the participating entities must have mobility to facilitate interactions and mass migration. Fourth, self-assembly typically takes place in solution or on a smooth surface or interface, where components can freely organize. Lastly, self-assembled structures are generally reversible, as they primarily involve non-covalent interactions and, in some cases, covalent bonds. Reversibility is thought to be a universal characteristic of self-assembly due to extensive research on biological and organic self-assembled systems. But as studies move into the inorganic realm, emerging studies suggest that some self-assembled structures

can be irreversible. This evolving understanding challenges conventional assumptions and sheds light on the complexity of self-assembly, particularly in the realm of inorganic materials.

There are various categories into which self-assembly mechanisms can be divided, with the broadest distinction being between static and dynamic self-assembly. Additionally, self-assembly can be categorized as chemical, physical, or colloidal, as well as guided (directed or templated) self-assembly. Further classifications are based on size (atomic, molecular, or colloidal) and the nature of interactions (interfacial or biological). Guided self-assembly encompasses a wide range of subcategories, including methods such lithography/masking, surface wetting, patterned substrates, electric or magnetic fields, and seeding. These approaches allow for greater control over the organization and arrangement of materials. On the other hand, conventional self-assembly includes supramolecular self-assembly, which involves amphiphile self-assembly (such as lipids, peptide amphiphiles, block copolymers, and hierarchical structures), as well as layer-by-layer assembly and other established techniques. Among nanoscale assembly techniques, top-down approaches have been a focal point of research for many years. However, methods such as lithography and etching encounter significant challenges, including high costs, slow processing speeds, and limitations imposed by the diffraction limit. These constraints hinder the scalability and efficiency of top-down fabrication, prompting increased interest in alternative approaches like bottom-up self-assembly, which offers greater precision, cost-effectiveness, and the potential for large-scale production of nanoscale materials. Self-assembly is a bottom-up approach in which multiple subunits spontaneously aggregate to form larger, well-defined, functional structures with distinct properties. This process is influenced by various factors, including temperature, pH, and electrolyte concentration, which regulate the stability and organization of the assembled structures. The ability to control self-assembly has led to the creation of innovative materials for a variety of uses. In regenerative medicine, self-assembled materials are being designed for biomimetic scaffolds, drug delivery, and tissue engineering, while in electronics, self-assembly is playing a key role in nanofabrication, sensors, and advanced functional materials. These advancements underscore the importance of self-assembly in creating next-generation materials for both biological and technological innovations.[2]

For example, these two transitions can be observed separately when they occur at different transition temperatures. By choosing the right transition behavior, these gels' phase-separated structures can be managed (**Fig. 1.2**). A randomly distributed fiber network arises in an isotropic medium (**Fig. 1.2B**) if the gelator's fibrous self-assembly takes place at a temperature higher than the liquid crystal component's isotropic–anisotropic transition temperature (**Type I, Fig. 1.2A**). In contrast, when the gelator assembles within the liquid-crystalline phase (**Type II, Fig. 1.2A**), the system develops an oriented liquid-crystalline gel is produced via an orientated self-assembled fiber network. This difference in structural organization

directly impacts the physical and functional properties of the gels, making them valuable for various applications in liquid crystal-based materials. The self-assembled fibers align along the twisted structure of the liquid crystals (**Fig. 1.3**) when the anisotropic self-assembly of nematic composites (**Fig. 1.2**) occurs within twisted nematic cells. These oriented-structure nematic gels show quick and intense electro-optical reactions. Type II gels have potential applications as light-scattering electro-optical materials in reverse mode. Specifically, nematic physical gels forming homeotropically oriented structures remain transparent in the absence of an electric field but become turbid when the field is applied. Additionally, it has been studied how self-assembling fibers affect the electro-optical performance of orientated ferroelectric smectic composites. These fibers' promise for sophisticated optical applications is demonstrated by their ability to modulate driving voltages and control hysteresis in electro-optical responses when incorporated into ferroelectric liquid crystals.[3]

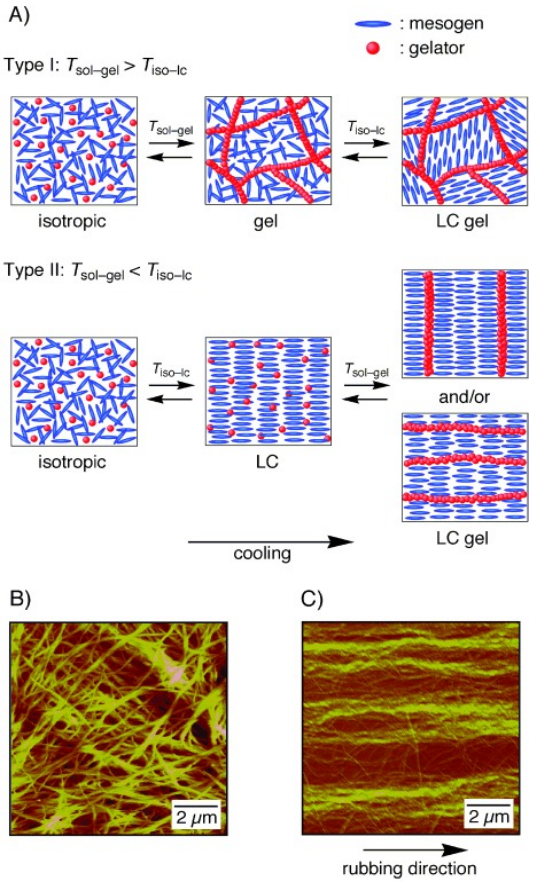

Figure 1.2. A. Two types of structural changes of liquid-crystalline physical gels. $T_{sol-gel}$: sol–gel transition temperature. T_{iso-lc}: isotropic–anisotropic transition temperature. **B.** AFM image of fibrous aggregates formed in an isotropic phase through Type I phase behavior. **C.** AFM image of oriented fibers formed in a homogeneously oriented nematic phase through Type II phase behavior.[3]

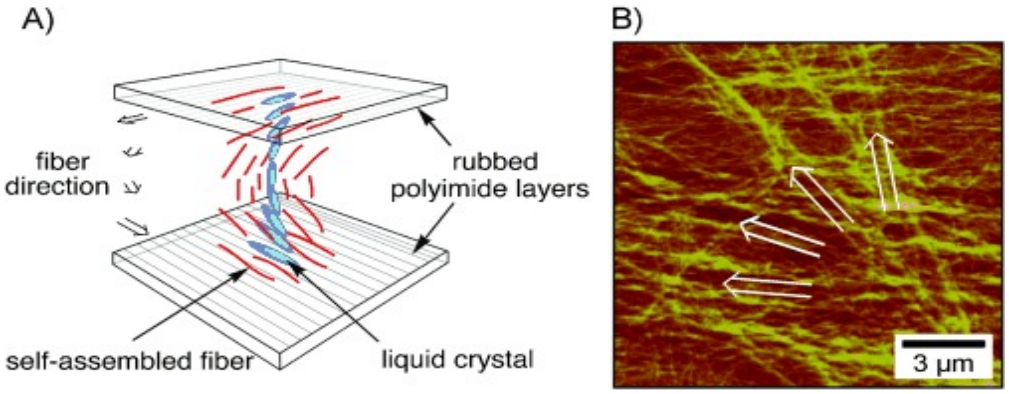

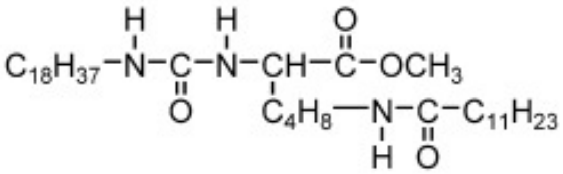

83

Gelators

Figure 1.3. A. Schematic illustration of a twisted nematic cell containing oriented nanofiber networks; **B.** AFM image of the oriented fibrous aggregates of **83** formed in a twisted nematic cell.[3]

1.2. Bio-inspired anisotropic structural materials

Bio-inspired anisotropic structural materials are a group of engineered materials that emulate the directional properties commonly observed in natural systems. In nature, many biological structures, including bone, wood, insect exoskeletons, and nacre (mother-of-pearl), exhibit anisotropy, meaning that their mechanical, optical, or transport properties vary depending on the direction in which force or stimuli are applied. This anisotropy allows these natural materials to combine high strength, toughness, and efficiency while remaining lightweight. For example, wood is an excellent natural analog to human trabecular bone, as its modulus, which is typically in the range of hundreds of megapascals (MPa), overlaps with the 10–3000 MPa range found in trabecular bone. Structurally, wood is composed mainly of cellulose, hemicellulose, and lignin, which together form a complex, hierarchically organized architecture that gives wood its strength and anisotropic behavior. Because of these characteristics, researchers have explored wood as a template for scaffold fabrication in bone tissue engineering. By selecting various types of wood and using delignification processes to remove specific components such as lignin, it is possible to create porous, interconnected, and directionally aligned scaffolds that mimic the structural and mechanical environment of bone. These wood-derived scaffolds offer multiple advantages: they are biocompatible,

mechanically robust, and cost-effective, as well as sustainable due to the abundance and renewability of natural wood resources. Compared to many synthetic biomaterials, wood provides a naturally occurring, highly organized framework that requires less processing and can potentially support **c**ell growth, nutrient transport, and vascularization in engineered tissues. **Figures 1.4A and 1.4B** illustrate how these bioinspired scaffolds are made, including the kinds of natural wood utilized and the delignification processes, highlighting the potential of nature-based strategies in advancing regenerative medicine and materials science.[4]

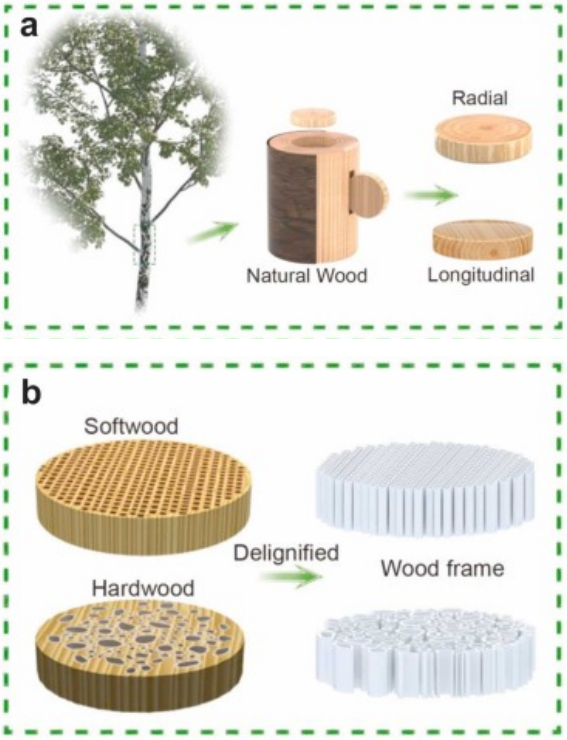

Figure 1.4. A. Schematic of two main types of wood frames, radial and longitudinal, that are generally used for processing; **B.** Process of delignification. The delignified wood can be used as frames for polymer infiltration.[4]

Nature-inspired materials are designed to replicate specific properties found in biological systems, offering advantages across multiple fields. These materials can be classified based on their benefits into biological, chemical, electrical, mechanical, sustainable, or multifunctional categories (**Fig. 1.5**). This classification helps in systematically organizing breakthroughs in bioinspired material design.[5] One remarkable example of nature's complex structural optimization is the Bouligand structure, a helicoidal arrangement of fibers resembling twisted plywood. There are several biological materials that include this structure, including the exoskeletons of insects and crustaceans, where it provides enhanced mechanical

strength, impact resistance, and energy dissipation. The periodic helicoidal stacking of longitudinal fiber layers enables these biological systems to withstand significant stress while maintaining lightweight and flexible properties. By studying and mimicking such hierarchical structures, researchers aim to develop advanced bioinspired materials for applications in structural engineering, protective coatings, biomedical implants, and high-performance composites. These materials can provide superior mechanical resilience, adaptive properties, and sustainability, making them highly valuable across multiple technological domains.[6]

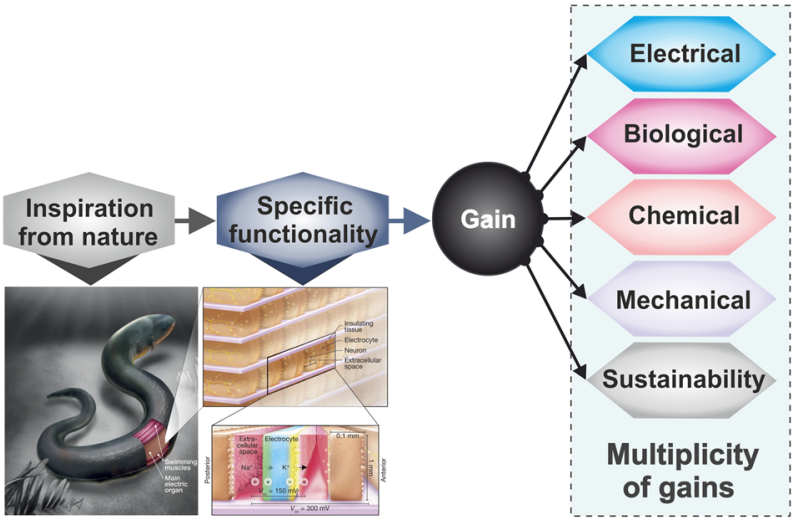

Figure 1.5. Categorisation of nature inspired mateirals based on different type of gains. The figure illustrate the source or the inspiration from nature translating to a specific functionality governing the type of gain which motivates the development of a specific type of a nature inspired material.[5]

Many natural structural materials found in biological systems, including skeleton, muscle, wood, tendon, and shell, have hierarchically organized structures that are essential for adaptation to complicated environments, such as surface mass transport, actuation, lubrication, and self-defense. It is very challenging to replicate such well-ordered hierarchical formations in synthetic hydrogels since the polymer chains disintegrate uniformly in aquatic environments. For example, following flow-induced alignment of the random PVA polymer chains, a kosmotropic salt solution promoted significant aggregation and crystallization, producing a single-composition hydrogel that is anisotropic and has a very compact, well-aligned structure (**Fig. 1.6A**). The hierarchical multiscale structures of the anisotropic fibrous hydrogel, which extend from the molecular to the macroscopic scale, are depicted in **Fig. 1.6B**. The hydrogel's anisotropic fibrous structure was made up of hydrogel fibers that were firmly layered at the microscale (**Fig. 1.6C**).[7]

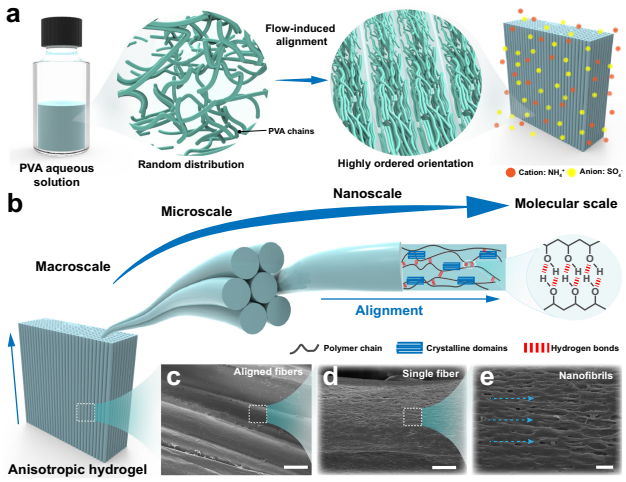

Figure 1.6. Highly aligned hierarchical fibrous hydrogels inspired by natural structural materials. **A.** Randomly distributed PVA polymer chains transform into a highly oriented hydrogel network by flow-induced alignment. **B.** Schematic illustration of anisotropic hydrogels with multiscale hierarchical architectures from macroscale to molecular scale. Multiscale magnified SEM images showing the preferentially aligned fiber structures. The scale bars for **C–E** are 100, 10, and 2 μm, respectively.[7]

Besides, a deacetylation of chitin generates chitosan (CS), a polysaccharide of amino acids with competitive bioactivities.[8] CS's hemostatic, antibacterial, anti-inflammatory, and antioxidant properties make it a functional biomaterial with more potential applications than cellulose.[9] Similar to cellulose-based materials,[10] advanced materials based on chitosan that have an anisotropic structure can also be created via electrospinning, prestretching and drying, or directional freezing.[11] For example, The radial direction of the silanized chitosan aerogel, which is perpendicular to the freezing direction, shows little thermal energy, whereas the axial direction, which is parallel to the freezing direction, shows a noticeably high thermal energy. This anisotropy permits axial heat dispersion and radial thermal insulation,[12] which permits more consistent dispersion of heat through the aerogel and protects against local heating-induced damage to the aerogel (**Fig. 1.7**).

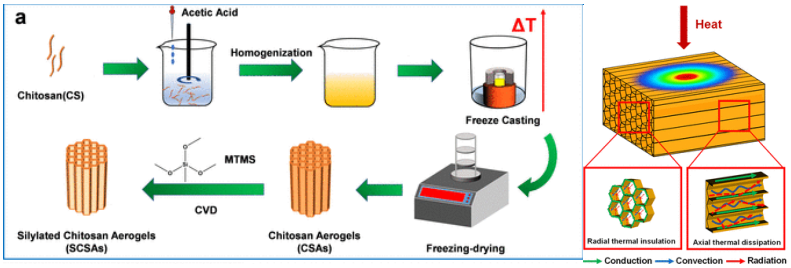

Figure 1.7. Schematic illustration of the chitosan molecular structure and the fabrication process of anisotropic aerogel.[12]

1.3. Preparation of polysaccharide membrane with oriented structure

A "polysaccharide membrane with oriented structure" describes a membrane composed of a natural polymer known as a polysaccharide, in which the polymer chains are aligned in a particular direction. This organized arrangement enhances the membrane's properties, such as increased mechanical strength or directional permeability, based on the achieved orientation.

One study explores sacran, a high-molecular-weight polysaccharide with unique properties like liquid crystallinity and self-assembly. A novel self-similar assembly method is proposed, where sacran forms uniaxially oriented fibrils that reorient into nanoplatelets and stack via nanolayering **(Fig. 1.8)**. Controlled evaporation and capillary forces drive the formation of a structured thin film, analyzed using electron microscopy.[13]

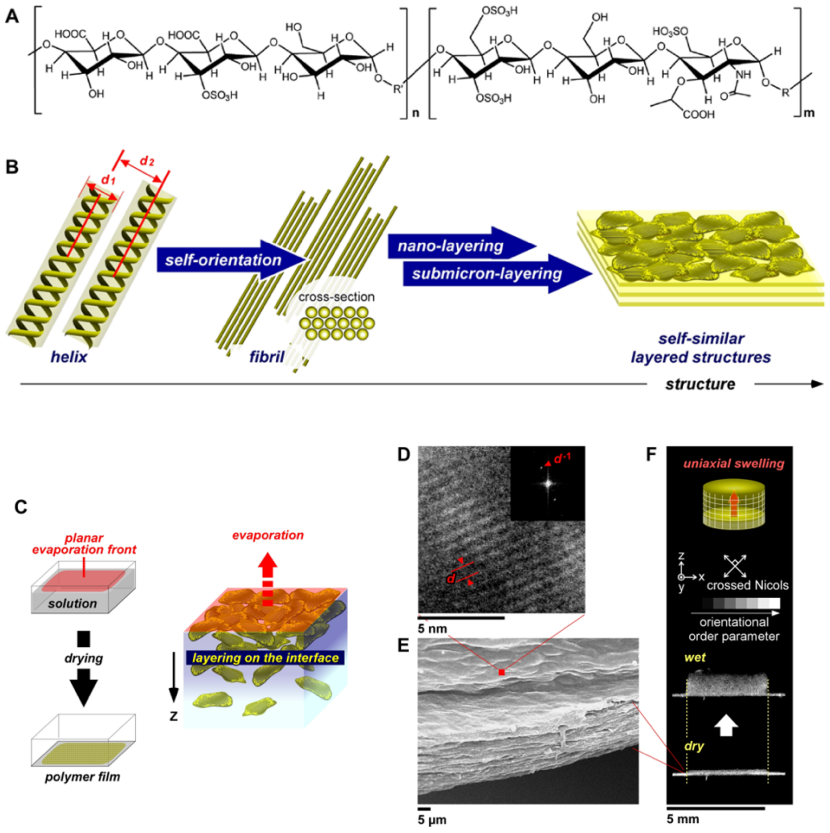

Figure 1.8. Schematic representation of structural hierarchy in the megamolecular polysaccharide, *sacran*. A. Chemical structure of *sacran*. **B.** Drying-induced formation of hierarchical structures of *sacran* polymer film through molecular self-orientation, nanolayering, and submicron layering. **C.** Preparation of a polymer film by drying the aqueous solution. **D.** TEM image, in top view, of the dried film and the FFT analytical data (inset). **E.** SEM image showing a cross-sectional view of the dried film. **F.** Microscopic images in cross-polarized light of hydrogel expansion, from a dry to a wet state showing uniaxial swelling without any lateral constraints.[13]

Polysaccharides have gained attention for their environmental adaptability, biocompatibility, and medical applications. They play a key role in advanced soft materials, such as drug delivery systems and flexible paper devices. While polysaccharides have unique self-assembly properties at nano- and micrometer scales, their hierarchical structures are rarely utilized due to difficulties in controlling their assembly. Reconstructing their self-assembled structures in vitro could enhance our understanding of their morphological changes and lead to new bio-inspired materials with regulated nano-scale architectures.[14] One example investigates the non-equilibrium self-assembly of sacran, a high-molecular-weight polysaccharide, during controlled evaporation. Sacran forms rod-like microdomains that fuse into a milliscale macrodomain at the air-liquid crystal (LC) interface, similar to natural anisotropic structures like vascular bundles. The study explores how drying environments influence structural formation, using top-side-open cells to control evaporation. A hierarchical deposition law is proposed to explain the formation of megastructures in 3D space (**Fig. 1.9**).[15]

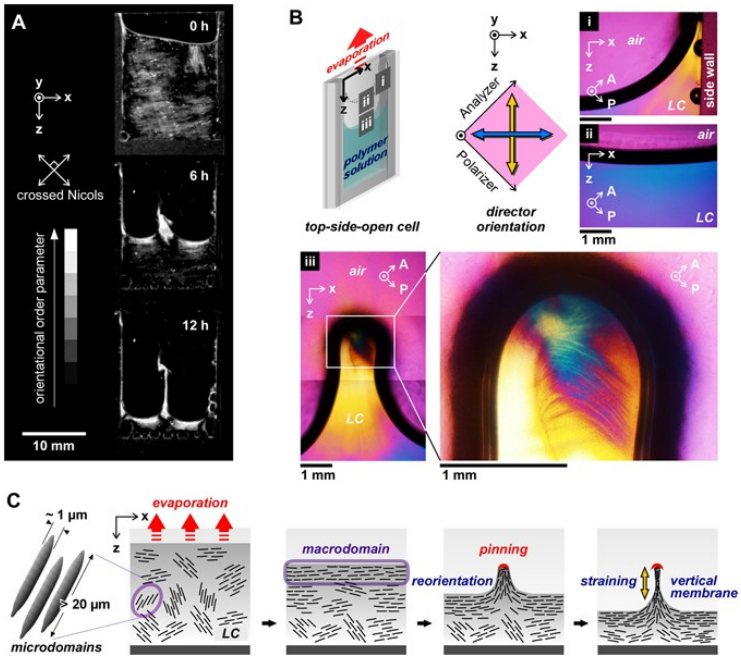

Figure 1.9. Interfacial instability of the polysaccharide liquid crystalline (LC) solution during drying in limited space. A. Side views of a sacran solution during drying process under cross-polarized light. **B.** Polarized microscopic images of the solution near the air-LC interface after 3h (area i and ii) and 6h of drying (area iii). The images were observed through a retardation plate, λ=530 nm with crossed Nicols in the illustrated directions. **C.** Schematic illustration for formation of vertical membranes by drying of a LC polymer solution in limited space with a narrow gap. Rod-like microdomains orient from the air-LC interface parallel to the contact line in the drying process. By drying in limited space, the non-equilibrium state between deposition and hydration near the interface causes pinning and vertical membrane formation between the narrow gap. The Z direction is parallel to the direction of gravity. The gap between glass slides is Δy_0=1mm. Initial concentration of sacran: 0.5wt%. Drying atmosphere: 60 °C under air pressure.[15]

In addition, Budpud et al. investigated a method for polysaccharide self-assembly by analyzing its morphological characteristics. Their study revealed that polysaccharides have the ability to form distinctive twisted fibers at both nanometer and micrometer scales (**Fig. 1.10**). This unique structural formation is significantly influenced by the air–water interface and capillary forces, which are essential to microfiber deposition during the drying process. The research further examined the deposition behavior of these fibers and their dynamic response to capillary forces, shedding light on the mechanisms governing their self-assembly. Moreover, a crosslinked polysaccharide film was developed to demonstrate its sensitivity to environmental conditions, particularly humidity. The study found that the microfiber structures exhibited spring-like deformations in response to humidity gradients, indicating their potential for applications in humidity-sensitive materials, sensors, and actuators.[16]

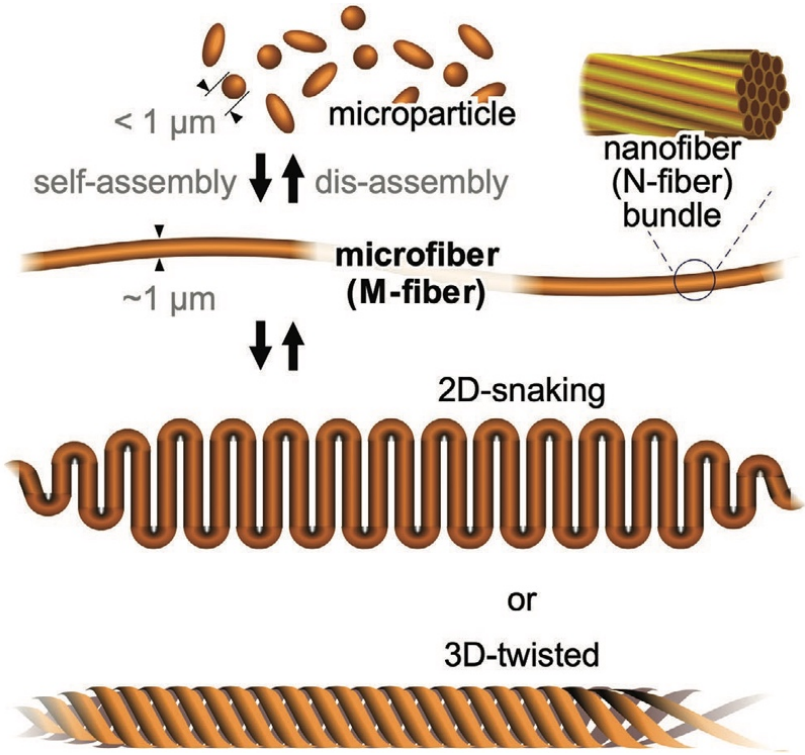

Figure 1.10. Schematic illustration of sacran fiber morphological changes. The upper section of the figure illustrates particle shapes with ≈1 μm diameter at low concentration and self-assembled microfiber with ≈1 μm diameter at high concentration, as well as the micrometer-scale fiber (M-fiber) as a bundle of nanometer-scale fibers with ≈50 nm dia- meter (N-fiber). The lower section of the figure illustrates the trans- formation of the M-fiber into 2D snaking and 3D twisted structures upon drying.[16]

1.4. Meniscus splitting method

Recently, several methods, such as pre-stretching and drying,[17] directional freezing,[18] and electrospinning,[19] have been reported for the preparation of polysaccharide-based materials with

anisotropic microstructures.[20–21] In contrast to these methods, we originally developed a meniscus splitting method[22–27] for preparing a three-dimensionally ordered polymer membrane by developing viscous fingering phenomena.[28–31] Under the control of temperature and humidity, the evaporative interface of the polymer solution/dispersion from a cell induces the orientation of polymeric microfibers along the contact line of the interface by capillary force. During water evaporation, the concentrated polymer at the interface bridges the millimeter-scale gap between the two substrates and forms vertical membranes. The limitation for the bridging distance is basically ~2 mm, depending on the capillary length.[28] Notably, the dried membranes exhibit microstructures that are oriented parallel to the gap direction and layered microstructures in the thickness direction. These three-dimensionally ordered anisotropic architectures have been demonstrated in several types of polysaccharides, such as pectin, sacran, and xanthan.[22-27, 32–33] (**Fig. 1.11**)

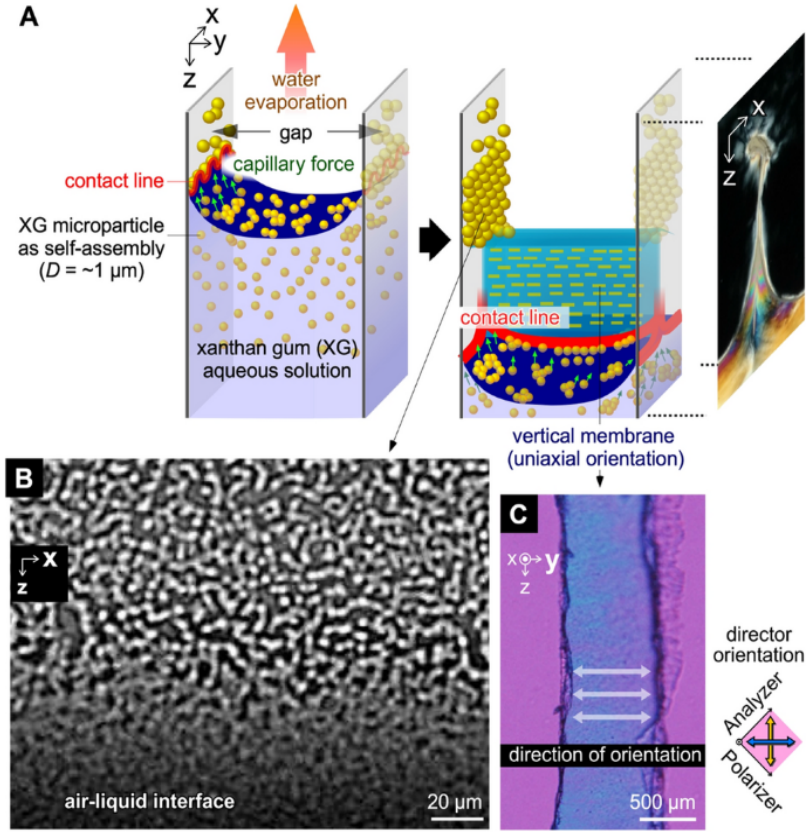

Figure 1.11. Deposition of polysaccharide microparticles from evaporative air–LC interface. **A.** Schematic of microparticle depositions on evaporative air–LC interface and vertical membrane formation. **B.** Optical microscopic images of XG deposited on a substrate. Initial concentration of XG: 0.5 wt%. Drying at 60 °C. **C.** Microscopic image of dried vertical membrane through crossed Nicols with a first-order retardation plate (λ = 530 nm). Inner dimensions of the cell: (X-width, Y-thickness, Z-depth) = (15 mm, 1 mm, ~ 20 mm).[28]

1.5. Anisotropic swelling/deswelling hydrogels

Anisotropic hydrogels can undergo shape morphing and produce anisotropic responses when exposed to external stimuli. There are many techniques used to create the anisotropic structures of hydrogels, including microfabricated structures, additive fillers, polymer-chain networks, and macroscopic assembly, are mostly ascribed to the anisotropic distribution of structures and components. The following are the main design and manufacturing techniques used to create hydrogels with anisotropy: gravity, electric and magnetic fields, local patterning, shear flow, polymer-chain alignment, and the production of layered structures.[34-36] Besides, different swelling tendencies in hydrogels will result in different physical characteristics, making them appropriate for a variety of biological uses. Especially, over the years, high-swelling hydrogels have grown in popularity for medication delivery, tissue regeneration, and full-thickness skin wound healing because of their ability to swell, which improves blood and bodily fluid absorption, nutrient and metabolite transfer, and drug diffusion and release. However, swelling under physiological environments would unavoidably result in noticeable macroscopic deformation and significantly decrease the hydrogels' conductivity, tissue adherence, and mechanical strength, among other physical properties. Therefore, non-swelling hydrogels have performed incredibly well in filling and healing the empty areas of some interior tissues or organs, as well as being used as bioadhesive sealants in surgical procedures, bioelectronic apparatus, and other applications.[37]

Hydrogels exhibit fascinating properties, one of which is their ability to undergo bending motion by utilizing the water they contain. This phenomenon has been harnessed in various applications, including soft robotics and biomedical devices. One promising approach to achieving bending motion in hydrogels involves manipulating their internal water distribution. Recent research has demonstrated an electroactive hydrogel capable of bending even outside of aqueous environments by leveraging a cationic polymer network (**Fig. 1.12**). This hydrogel operates by utilizing its high water absorption capacity and intrinsic ionic conductivity to drive internal water movement asymmetrically. Specifically, the cationic network facilitates the migration of water molecules toward one side of the hydrogel, leading to localized swelling on that side while the opposite side shrinks. This asymmetric deformation results in a bending motion. Such bending behavior is particularly advantageous for applications like robotic grippers, where controlled and reversible shape changes are essential for grasping and manipulating objects. Additionally, this technology has potential implications in soft actuators, biomimetic devices, and responsive materials, further expanding the functional versatility of hydrogels in real-world application.[35]

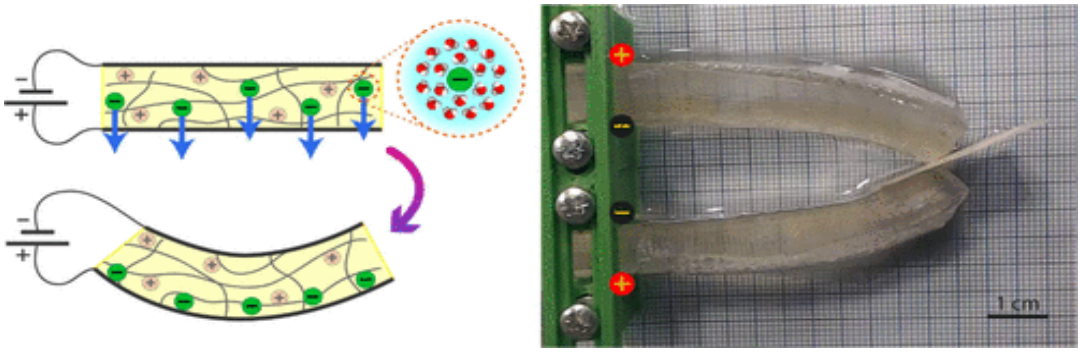

Figure 1.12. Bending response of our cationic hydrogel under air conditions. The free anions (chlorides) drag the free water contained inside the hydrogel toward the positive electrode, originating a gradient of swelling that bends the hydrogel bar toward the negative electrode. This behavior can be applied to build soft grippers: two parallel hydrogel bars actuated with opposite electric fields (in this case, with the negative pole inside due to the hydrogel's nature). The electrodes are simple aluminum foil sheets attached to the hydrogel.[35]

1.6. Objective of this research

The main objective of this research is to analyze and quantify the variations in the interface positions of a specific polymer solution during solvent evaporation using the meniscus splitting method. This involves observing how the polymer behaves under controlled conditions and identifying the primary elements that affect the movement and stability of the interface. To achieve this, we will develop mathematical models that incorporate fundamental equations describing the system dynamics. These models, when combined with experimental data, will allow us to predict and validate the interface behavior accurately. The ultimate goal is to ensure that the derived equations align closely with observed experimental trends, thereby providing a reliable framework for understanding meniscus splitting in polymer solutions.

In the chapter 3, after solvent evaporation, a vertical membrane forms as a result of interface fluctuations and boundary recognition. This membrane serves as a structural foundation for further analysis of the nucleation process. Depending on the conditions, either a single nucleus (N1) or two nuclei (N1 and N2) may emerge, leading to variations in membrane growth. The shift in the interface position and symmetry breaking play crucial roles in determining whether nucleation occurs synchronously or asynchronously. Finally, we developed a three-dimensionally ordered chitosan network and engineered a chitosan hydrogel capable of anisotropic swelling and deswelling in response to pH variations. Besides, we analyzed the anisotropic nano- and microstructures in the dried membranes using different methods such as polarized optical microscopy, scanning electron microscopy (SEM), wide- and small-angle X-ray scattering (WAXS and SAXS), as well as polarized attenuated total reflection infrared spectroscopy.

In this thesis, we focused on three main topics on the following,

I) Building the theoretical and experimental model of pure water and λ-carrageenan solution using the meniscus splitting method based on the depth change of cell via time-course change during solvent evaporation process.

II) Demonstrating multiple nucleations by focusing on misalignments from symmetry and synchronicity.

III) Reconstructing a chitosan network with a three-dimensional order and designed a chitosan hydrogel that exhibited anisotropic swelling/deswelling with pH changes.

Chapter 2

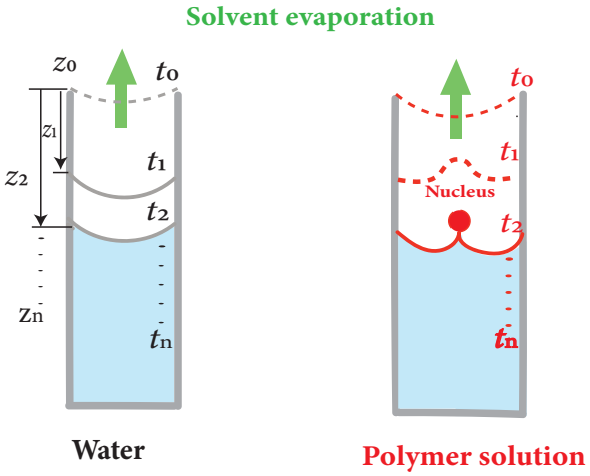

Chapter 3

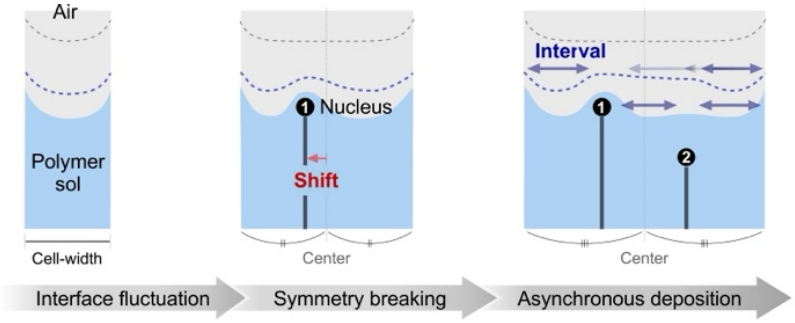

Chapter 4

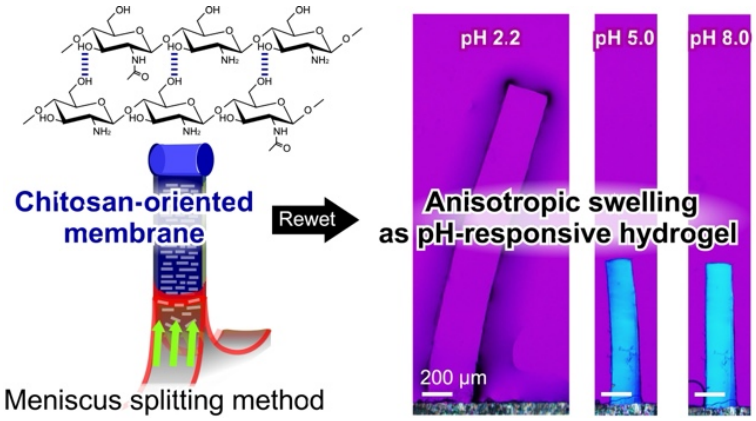

Figure 1.13. Summary the schematic illustration of this study.

References

[1] Alexandros Chremos, Self Assembly in Soft Matter, Doctor of Philosophy, University of Edinburgh, 2008.

[2] Campos, M. T.; Pires, L. S.; Magalhães, F. D.; Oliveiracd, M. J.; Pinto, A. M. Self-assembled inorganic nanomaterials for biomedical applications. *Nanoscale* **2025**, *17*, 5526-5570.

[3] Kato, T.; Mizoshita, N.; Kishimoto, K. Functional Liquid-Crystalline Assemblies:Self-Organized Soft Materials. *Angew. Chem. Int. Ed*. **2006**, *45*, 38 –68.

[4] Chen, J. Current advances in anisotropic structures for enhanced osteogenesis. *Colloids Surf. B Biointerfaces*. **2023**, *231*, 113566.

[5] Katiyar, N. K.; Goel, G.; Hawi, S.; Goel, S. Nature-inspired materials: Emerging trends and prospects. *NPG Asia Mater*. **2021**, *13*, 56.

[6] Zengqian, L.; Zhefeng, Z.; Robert, O. Ritchie. Structural Orientation and Anisotropy in BiologicalMaterials: Functional Designs and Mechanics. *Adv. Funct. Mater*. **2020**, *30*, 1908121.

[7] Zhu, S.; Wang, S.; Huang, Y.; Tang, Q.; Fu, T.; Su, R.; Fan, C.; Xia, S.; Lee, P. S.; Lin, Y. Bioinspired structural hydrogels with highly ordered hierarchical orientations by flow-induced alignment of nanofibrils, *Nat. Commun*. **2024**, *15*, 118.

[8] Yang, G.; Hou, X.; Lu, J.; Wang, M.; Wang, Y.; Huang, Y.; Liu, Q.; Liu, S.; Fang, Y. Enzymatic modification of native chitin and chitin oligosaccharides by an alkaline chitin deacetylase from Microbacterium esteraromaticum MCDA02. *Int. J. Biol. Macromol*. **2022**, *203*, 671–678.

[9] Cheng, Y.; Cheng, G.; Xie, C.; Yin, C.; Dong, X.; Li, Z.; Zhou, X.; Wang, Q.; Deng, H.; Li, Z. Biomimetic silk fibroin hydrogels strengthened by silica nanoparticles distributed nanofibers facilitate bone repair. *Adv. Healthc. Mater*. **2021**, *10* (9), 2001646.

[10] Nirmala, R., Il, B. W.; Navamathavan, R.; El-Newehy, M. H, Kim, H. Y. Preparation and characterizations of anisotropic chitosan nanofibers via electrospinning. *Macromol. Res*. **2011**, *19* (4), 345.

[11] Wu, J.; Yun, Z.; Song, W.; Yu, T.; Xue, W.; Liu, Q.; Sun, X. Highly oriented hydrogels for tissue regeneration: design strategies, cellular mechanisms, and biomedical applications. *Theranostics*. **2024**, *14* (5):1982-2035.

[12] Xiao, W.; Wang, P.; Song, X.; Liao, B.; Yan, K.; Zhang, J-J. Facile fabrication of anisotropic chitosan aerogel with hydrophobicity and thermal superinsulation for advanced thermal management. *ACS Sustainable Chemistry & Engineering,* **2021**, *9* (28), 9348–9357.

[13] Okeyoshi, K.; Joshi, G.; Rawat, S.; Sornkamnerd, S.; Amornwachirabodee, K.; Okajima, K. M.; Ito, M.; Kobayashi, S.; Higashimine, K.; Oshima, Y.; Kaneko, T. Drying-Induced Self-Similar Assembly of Megamolecular Polysaccharides through Nano and Submicron Layering. *Langmuir* **2017,** *33* (20), 4954-4959.

[14] Jabeen, N.; Atif, M. Polysaccharides based biopolymers for biomedical applications: A review. *Polym Adv Technol*. **2024**, *35*, e6203.

[15] Okeyoshi, K.; Okajima, M. K.; Kaneko, T. Emergence of polysaccharide membrane walls through macro-space partitioning via interfacial instability. *Sci Rep* **2017**, *7*, 5615.

[16] Budpud, K.; Okeyoshi, K.; Okajima, K. M.; Kaneko. T. Vapor-Sensitive Materials from Polysaccharide Fibers with Self-Assembling Twisted Microstructures. Small **2020***, 16,* 2001993.

[17] Ye, D.; Lei, X.; Li, T.; Cheng, Q.; Chang, C.; Hu, L.; Zhang, L. Ultrahigh Tough, Super Clear, and Highly Anisotropic Nanofiber-Structured Regenerated Cellulose Films. *ACS Nano* **2019**, *13*, 4843−4853.

[18] Chen, Y.; Zhou, L.; Chen, L.; Duan, G.; Mei, C.; Huang, C.; Han, J.; Jiang, S. Anisotropic nanocellulose aerogels with ordered structures fabricated by directional freeze-drying for fast liquid transport. *Cellulose* **2019**, *26*, 6653–6667.

[19] Cheng, G.; Yin, C.; Tu, H.; Jiang, S.; Wang, Q.; Zhou, X.; Xing, X.; Xie, C.; Shi, X.; Du, Y.; Deng, H.; Li, Z. Controlled Co-delivery of Growth Factors through Layer-by-Layer Assembly of Core−Shell Nanofibers for Improving Bone Regeneration. *ACS Nano* **2019**, *13*, 6372−6382.

[20] Wang, N.; Wang, X. X.; Yan, K.; Song, W.; Fan, Z.; Yu, M.; Long, Y. Z. Anisotropic Triboelectric Nanogenerator Based on Ordered Electrospinning. *ACS Appl. Mater. Interfaces*, **2020**, *12*, 46205−46211.

[21] Hecht, M.; Soberats, B.; Zhu, J.; Stepanenko, V.; Agarwal, S.; Greiner, A.; Würthner. F. Anisotropic microfibres of a liquid-crystalline diketopyrrolopyrrole by self-assembly-assisted electrospinning. *Nanoscale Horiz*. **2019**, *4*, 169-174.

[22] Okeyoshi, K.; Okajima, M. K.; Kaneko, T. Emergence of Polysaccharide Membrane Walls Through Macro-space Partitioning Via Interfacial Instability. *Sci. Rep*. **2017**, *7*, 5615.

[23] Okeyoshi, K.; Joshi, G.; Okajima, M. K.; Kaneko, T. Formation of Polysaccharide Membranes by Splitting of Evaporative Air-LC Interface. *Adv. Mater. Inter*. **2018**, *5*, 1701219.

[24] Okeyoshi, K.; Shinhama, T.; Budpud, K.; Joshi, G.; Okajima, M. K.; Kaneko, T. Micelle-mediated Self-assembly of Microfibers Bridging Millimeter-scale Gap to Form Three-dimensional-ordered Polysaccharide Membranes. *Langmuir* **2018**, *34*, 13965−13970.

[25] Okeyoshi, K.; Yamashita, M.; Sakaguchi, T.; Budpud, K.; Joshi, G.; Kaneko, T. Effect of Evaporation Rate on Meniscus Splitting with Formation of Vertical Polysaccharide Membranes. *Adv. Mater. Inter*. **2019**, *6*, 1900855.

[26] Joshi, G.; Okeyoshi, K.; Mitsumata, T.; Kaneko, T. Micro-deposition Control of Polysaccharides on Evaporative Air-LC Interface to Design Quickly Swelling Hydrogels. *J. Colloid Interf. Sci*. **2019**, *546*, 184−191.

[27] Okeyoshi, K.; Yamashita, M.; Budpud, K.; Joshi, G.; Kaneko, T. Convective meniscus splitting of polysaccharide microparticles on various surfaces. *Sci. Rep*. **2021**, *11*, 767.

[28] Brzoska, J. B.; Brochard-Wyart, F.; Rondelez, F. Exponential Growth of Fingering Instabilities of Spreading Films Under Horizontal Thermal Gradients. *Europhys. Lett*. **1992**, *19*, 97−102.

[29] Lajeunesse, E.; Martin, J.; Rakotomalala, N.; Salin, D. 3D Instability of Miscible Displacements in a Hele-Shaw Cell. *Phys. Rev. Lett*. **1997**, *79*, 5254−5257.

[30] Kataoka, E. D.; M. Troian, M. S. Patterning liquid flow on the microscopic scale. *Nature* **1999**, *402*, 794–797.

[31] de Gennes, P. G.; Brochard-Wyart, F.; Quéré, D. Capillarity and Wetting Phenomena: Drops, Bubbles, Pearls, Waves; *Springer*, 2003.

[32] Wu, L.; Saito, I.; Hongo, K.; Okeyoshi, K. Recognition of Spatial Finiteness in Meniscus Splitting Based on Evaporative Interface Fluctuations. *Adv. Mater. Inter*. **2023**, *10*, 2300510.

[33] Saito, I.; Wu, L.; Hara, M.; Ikemoto, Y.; Kaneko, T.; Okeyoshi, K. Anisotropic Responses with Cation Selectivity in Hierarchically Ordered Polysaccharide Networks. *ACS Appl. Polym. Mater*. **2022**, *4*, 7054−7060.

[34] Chen, Z.; Wang, H.; Cao, Y.; Chen, Y.; Akkus, O.; Liu, H.; Cao, C. Bio-inspired anisotropic hydrogels and their applications in soft actuators and robots. *Matter*. **2023**, *6*, 3803–3837.

[35] Chen, Y.; Zhang, Y.; Li, H.; Shen, J.; Zhang, F.; He, J.; Lin, J.; Wang, B.; Niu, S.; Han, Z.; Guo, Z. Bioinspired hydrogel actuator for soft robotics: Opportunity and challenges. *Nano Today*. **2023**, *49*, 101764.

[36] López-Díaz, A.; Vázquez, A. S.; Vázquez, E. Hydrogels in Soft Robotics: Past, Present, and Future., *ACS Nano*. **2024,** *18*, 20817−20826.

[37] Feng, W.; Wang, Z. Tailoring the Swelling-Shrinkable Behavior of Hydrogels for Biomedical Applications. *Adv. Sci*. **2023**, *10*, 2303326.

Chapter 2

Time course changes of interface positions of polymer solution in meniscus splitting

2.1. Theoretical equation introduction

Liquid evaporation is a fundamental physical phenomenon that plays an important part of a variety of biological, environmental, and industrial processes. It serves as the driving force behind various applications such as inkjet printing, microfluidic device operation, coating technologies, particle self-assembly, and drug delivery systems. Understanding the dynamics of evaporation is vital for controlling and optimizing outcomes in these systems, particularly in scenarios involving thin-film formation, solute crystallization, and capillary-driven flows. These dynamics not only influence material deposition and surface patterning but also affect the overall efficiency and precision of advanced manufacturing techniques. One particularly interesting aspect of evaporation is the behavior of confined liquids, where solvent evaporation leads to changes in liquid depth over time. This can significantly alter the morphology, concentration gradients, and physical behavior of the remaining solution. The meniscus evolution, or the curved liquid-air interface formed during evaporation, is of special interest in confined geometries such as Hele-Shaw cells or microchannels. As the solvent evaporates, changes in the meniscus affect capillary forces, surface tension gradients, and phase transitions, which can induce fluid instabilities, self-organizing structures, or even pattern formation at the micro- and nanoscales. Studying these phenomena provides valuable insights into fluid mechanics, interface science, and soft matter physics. For instance, detailed analysis of evaporation-induced flow and meniscus deformation can help predict and control solute transport, particle alignment, and crystal nucleation, which are essential for fabricating structured materials and membranes with desired properties. Moreover, insights gained from such studies have implications in biological systems (e.g., tear film dynamics, skin hydration), environmental processes (e.g., soil moisture evaporation), and the development of smart materials for sensors, actuators, and biomedical devices.

In this research, we aim to establish comprehensive theoretical and experimental frameworks to investigate the evaporation-driven meniscus dynamics in both pure water and polymer solution. λ-carrageenan, a naturally derived sulfated polysaccharide widely utilized in pharmaceutical and biomedical fields, modifies critical physical parameters of the solution, including viscosity, surface tension, and diffusivity. These changes, in turn, significantly influence the evaporation kinetics and interface behavior of the liquid, making it an ideal candidate for exploring the interplay between biopolymer properties and meniscus evolution. To analyze this behavior, we employ the meniscus splitting technique, which enables high-resolution observation and quantification of interface deformation and depth profile variations during solvent loss. Through this approach, we seek to determine how the presence of λ-carrageenan affects the stability, symmetry, and self-organization of the liquid interface under evaporative conditions. This includes examining the formation of structural patterns, capillary effects, and phase transitions that arise due to concentration gradients and differential drying rates. Ultimately, this study is expected to provide valuable

insights into evaporation-induced morphological transitions in soft matter systems. The findings have potential implications across a variety of domains, including microfluidic device design, coating and printing technologies, and targeted drug delivery systems, where precise control over liquid behavior and interface stability is essential. Understanding the dynamic response of biopolymer solutions under evaporation can also aid in the development of smart hydrogel systems and bioinspired materials tailored for advanced biomedical applications.[1-13]

Interpretation of the model (**Fig. 2.1**):

- The diagram likely represents liquid behavior within a confined space (such as a polymer solution in a capillary system).
- As time progresses, the meniscus moves from z_0 to z_1, influenced by pressures P_0 and P_1.
- The presence of a sinusoidal curve suggests variations in capillary flow, possibly due to evaporation, diffusion, or capillary forces.
- The mass of water, M_{water}, indicates that the amount of liquid in the system plays a role in these dynamics.

This model could be useful for studying controlled liquid flow in capillary-based systems, such as polymer deposition, biological fluid transport, or hydrogel swelling mechanisms.

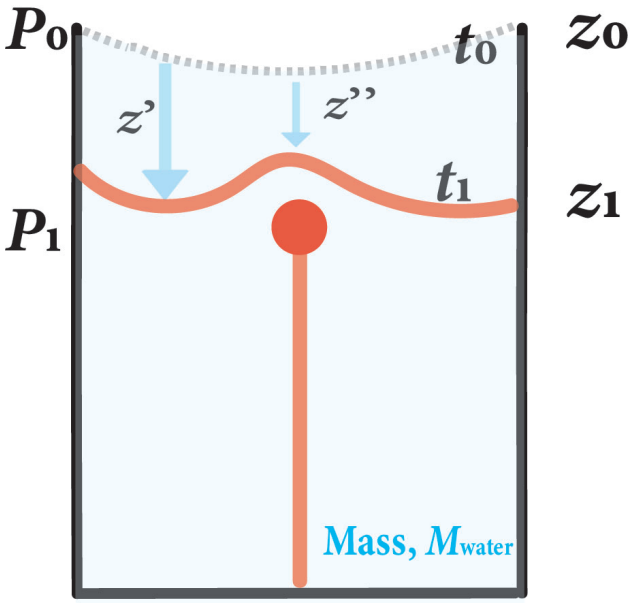

Figure 2.1. Schematic illustration of the nucleation and deposition process induced by meniscus splitting.

Theoretical equation of pure water[8]

$$\frac{dz}{dt} = \frac{P_{\mathrm{atm}} M_{water} D_{water}}{RTz\rho_{\mathrm{water}}} \ln \frac{1}{1 - \frac{P_{water}}{P_{\mathrm{atm}}}}$$

Theoretical equation of aqueous polymer solution[8]

$$\frac{dz}{dt} = \frac{-M_{\mathrm{polymer}} P_{\mathrm{atm}} D_{\mathrm{polymer}} \ln[\frac{(P_{\mathrm{atm}} - P_{\mathrm{water}})}{(P_{\mathrm{atm}} - P_1)}]}{\rho_{\mathrm{polymer}} RTz}$$

Assumptions for the derivation of the depth evolution:

Two above equations were obtained by adapting a simplified 1D drying model based on previous studies (e.g., Stefan-type models and constant-rate evaporation assumptions), which are commonly applied in systems with constrained geometries like Hele-Shaw cells. The objective is to describe the temporal evolution of the interfacial depth, z(t), during solvent evaporation.

To derive and apply these equations, the following assumptions were made:

The interfacial depth function z(t) is assumed to be continuous and differentiable over time, enabling the use of differential equations to describe its evolution.

The air–liquid interface is assumed to remain smooth and clearly visible throughout the drying process. This allows for definition of z(t) at each time point.

The temperature and relative humidity in the drying chamber are kept constant and homogeneous via environmental controls. As a result, the evaporation rate is primarily a function of the liquid properties and interfacial dynamics, rather than external fluctuations.

2.2. Materials and Methods

2.2.1. Materials

λ-carrageenan is a type of carrageenan which can be extracted from marine edible red algae with a M_w of 1.92 x 10^6 g/mol, was acquired from Japan's Wako Pure Chemical Industries.

2.2.2. Drying experiments for spatiotemporal analysis

The aqueous solution at ~25 ℃ was poured into a topside open cell, which is a type of Hele-Shaw cell. The cells were placed in a ~ 1 L observation box under controlled temperature and humidity using a

temperature-controlled air circulation pump. The internal temperature of the box was controlled by using two methods: one involved connecting a heat pen to a circulating tube, and the other involved attaching a rubber heater to the inner walls of the box. The relative humidity in the box was controlled by maintaining a constant temperature and ensuring air circulation. The correlation between temperature and relative humidity was verified, confirming the ability to sustain consistent humidity during the drying experiments. Throughout the drying process, the samples were observed through glass windows, and images were captured at certain time intervals (10 min). The interfacial positions (X, Z) were determined by establishing the top corner of the cell as the coordinate origin (O).

2.3. The effect of polymer solution on evaporation rate

2.3.1. Theoretical/Experimental curve of pure water

Fig. 2.2 schematically illustrates the evaporation process of pure water in a vertical system over time. At the initial time $t = 0$, the system is fully saturated, with the air–water interface located at height z_0. As evaporation proceeds, water is removed from the surface, causing the air–water interface to shift to a lower position. At a later time t_1, the interface has shifted to a new position z_1, as indicated by the blue curve. The evaporation continues over time, with the water front progressively moving to depths z_2, z_3, and eventually reaching z_s at t_∞, which represents a steady or quasi-steady state. Throughout the process, evaporation occurs unidirectionally from the top surface, driven by the concentration gradient between the liquid surface and the ambient air. This setup provides a clear visual representation of the capillary-driven and evaporation-controlled dynamics occurring during the drying of pure water.

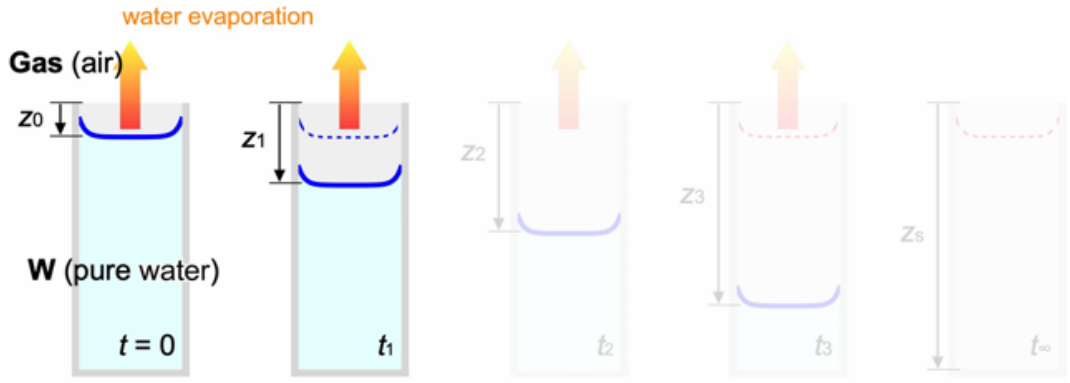

Figure 2.2. The model of evaporation rate for pure water in a Hele-Shaw cell.

Theoretical equation[8]

$$\frac{dz}{dt} = \frac{P_{\text{atm}} M_{\text{water}} D_{\text{water}}}{RTz\rho_{water}} \ln \frac{1}{1 - \frac{P_{water}}{P_{\text{atm}}}}$$

$$K = \frac{P_{\text{atm}} M_{water} D_{\text{water}}}{RT\rho_{water}} \ln \frac{1}{1 - \frac{P_{water}}{P_{\text{atm}}}}$$

Integrating the equation from $t = 0$ to t_1

$$K \int_0^{t1} dt = \int_{z0}^{z1} z dz$$

$$K_{t1} = \frac{(z_1^2 - z_0^2)}{2}$$

$$t_1 = \frac{1}{2K}(z_1^2 - z_0^2)$$

$$\rightarrow \; z_1 = \sqrt{2Kt_1 + z_0^2} \qquad (1)$$

Where:

P_{atm}: ambient atmospheric pressure (mmHg)

P_{water}: vapor pressure of pure water at temperature T (mmHg)

R: gas law constant (R= 8.314 J mol^{-1} K^{-1})

ρ_{water}: density of pure water at T (g cm^{-3})

D_{water}: the diffusivity of pure water at temperature T (cm^2 s^{-1})

M_{water}: the molecular weight of pure water (g mol^{-1})

t_1: time during which the meniscus falls from z_0 to z_1 (min)

z_0: distance from the mouth of the capillary to the meniscus at $t = 0$ (mm)

z_1: distance from the mouth of the capillary to the meniscus at t_1 (mm)

How to calculate z_1

40 ℃

By choosing z_0 = 1 mm, based on the experimental value, the period from 0 to 1500 minutes was used for for the theoretical analysis.

$$K = \frac{P_{\text{atm}} M_{water} D_{\text{water}}}{RT\rho_{water}} \ln \frac{1}{1 - \frac{P_{water}}{P_{\text{atm}}}} = \frac{760 \times 18 \times 0.324}{8.314 \times 313.15 \times 0.992} \ln \frac{1}{1 - \frac{55.3}{760}} = 0.13$$

$$z_1 = \sqrt{2Kt_1 + z_0^2} = \sqrt{0.26t_1 + 1^2}$$

60 ℃

By choosing z_0 = 1 mm, based on the experimental value, the period from 0 to 380 minutes was used for for the theoretical analysis.

$$K = \frac{P_{\text{atm}} M_{water} D_{\text{water}}}{RT\rho_{water}} \ln \frac{1}{1 - \frac{P_{water}}{P_{\text{atm}}}} = \frac{760 \times 18 \times 0.4772}{8.314 \times 333.15 \times 0.983} \ln \frac{1}{1 - \frac{149.4}{760}} = 0.52$$

$$z_1 = \sqrt{2Kt_1 + z_0^2} = \sqrt{1.05t_1 + 1^2}$$

At 40 ℃ and 60 ℃, the vapor pressure of pure water (P_{water}) is 55.3 and 149.4 mmHg, respectively. The diffusivity of water vapor (D_{water}) in air at these temperatures is 0.324 $cm^2\ s^{-1}$ and 0.477 $cm^2\ s^{-1}$, respectively, indicating that water molecules diffuse more rapidly in air as temperature increases. Additionally, the density of liquid water (ρ_{water}) decreases slightly from 0.992 g cm^{-3} at 40°C to 0.983 g cm^{-3} at 60°C due to thermal expansion. The evaporation coefficient, *K*, which represents the rate of mass transfer during the evaporation process, is given as 0.123 at 40 ℃ and increases significantly to 0.525 at 60 ℃. This suggests that evaporation occurs at a much faster rate at the higher temperature due to increased molecular motion and higher vapor pressure, which drives the phase transition from liquid to gas.[1-10]

Using **Equation (1)** and experimental data, we can determine the characteristic evaporation depth, the z_1 for both temperature conditions. The theoretical and experimental evaporation curves, as shown in **Figure 2.3**, exhibit strong agreement, validating the mathematical model used to explain the process of

evaporation. Moreover, the total evaporation time for pure water varies significantly with temperature. At 40 °C, the complete evaporation of a given water sample takes approximately 1500 minutes, whereas at 60 °C, the evaporation time is considerably shorter, around 400 minutes. This significant reduction in evaporation time at the higher temperature aligns with the observed increase in vapor pressure, diffusivity, and evaporation coefficient, which collectively enhance the rate of phase change.

The higher K value at 60 °C reflects the increased evaporation speed due to the combined effects of higher vapor pressure, greater diffusivity, and reduced density. This analysis confirms that temperature plays a crucial role in evaporation, with higher temperatures accelerating the process due to increased vapor pressure and diffusivity. The good match between theoretical predictions and experimental data indicates that the model can reliably describe evaporation behavior under these conditions.

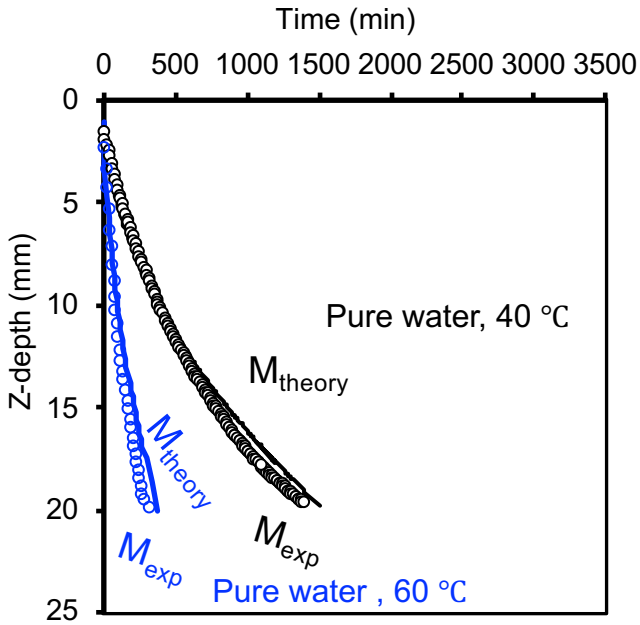

Figure 2.3. These theoretical/experimental curves of pure water.

2.3.2. Theoretical/Experimental curves of aqueous polymer solution

Fig. 2.4 illustrates the process by which a polymer solution (PS) evaporates in a vertical system over time. At the initial time $t = 0$, the polymer solution is fully saturated, and the air-solution interface is located at height z_0. As evaporation proceeds, the interface shifts to a lower position, reaching z_1 at time t_1. Unlike pure water, the presence of the polymer affects the behavior of the evaporation front, leading to the development of non-uniformities along the interface, as shown at time t_2. As the process continues, these undulations become more pronounced, and at time t_3, a nucleus appears and grows upward from the solution,

indicated in the figure. Eventually, at time t_∞, the evaporation front stabilizes at a final position z_s. Throughout this process, evaporation remains unidirectional from the top surface, and the figure highlights how the evaporation dynamics in a polymer solution differ from those in pure water, primarily due to the solute's influence on the interface shape and movement.

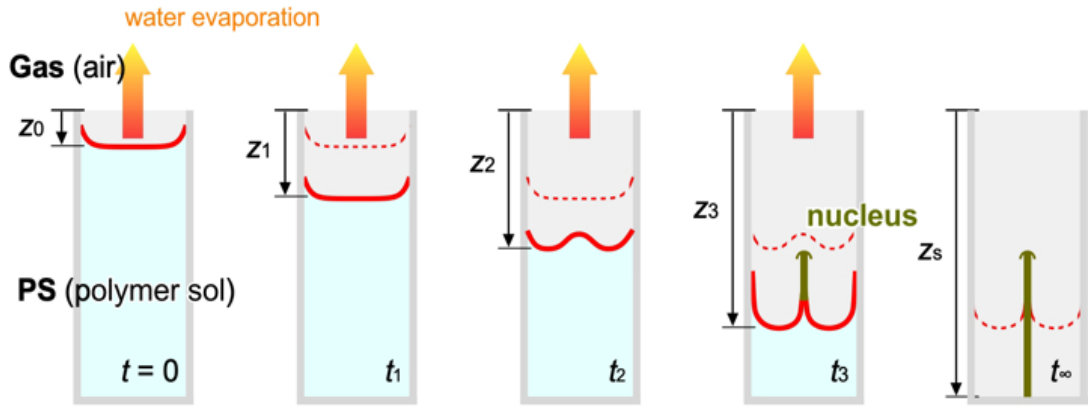

Figure 2.4. The model of evaporation rate for polymer solution in a Hele-Shaw cell.

Theoretical equation[8]

$$\frac{dz}{dt} = \frac{-M_{\text{polymer}} P_{\text{atm}} D_{\text{polymer}} \ln[\frac{(P_{\text{atm}} - P_{\text{water}})}{(P_{\text{atm}} - P_1)}]}{\rho_{\text{polymer}} RTz}$$

$$K_1 = \frac{-\rho_{\text{polymer}} RT}{D_{\text{polymer}} P_{\text{atm}}\, M_{\text{polymer}} \ln[\frac{(P_{\text{atm}} - P_{\text{water}})}{(P_{\text{atm}} - P_1)}]}$$

Where

P_{atm}: ambient atmospheric pressure (mmHg)

P_{water}: vapor pressure of pure water at temperature T (mmHg)

P_0: pressure of water from the mouth of the cell to the meniscus at t = 0 (mmHg)

P_1: pressure of water from the mouth of the cell to the meniscus at t_1 (mmHg)

R: gas law constant (R= 8.314 J mol^{-1} K^{-1})

ρ_{polymer}: the density of polymer solution at T (g cm^{-3}) (input of experimental value)

$M_{polymer}$: the molecular weight of polymer (g mol^{-1})

$D_{polymer}$: the diffusivity of polymer in dilute aqueous solution (cm^2 s^{-1})

$t_{123\ldots\infty}$: time course change (using Get Data Graph Digitizer) (min)

z_0: distance from the mouth of the capillary to the meniscus at $t = 0$ (mm)

z_1: distance from the mouth of the capillary to the meniscus at t_1 (mm)

Besides, Wilke and Chang[14-15] have proposed the following correlation to estimate the diffusivity of polymer ($D_{polymer}$) in dilute aqueous solution according to

$$\frac{D_{\text{polymer}} \propto}{T} = \frac{7.4 \times 10^{-8}(\phi_{water} M_{water})^{1/2}}{V^{0.6}}$$

Where

P_{atm}: ambient atmospheric pressure

V: the solute molar volume at its normal boiling point (for water as solute, $V = 75.6$ (cm^3 gmol^{-1})

ϕ_{water}: the association factor of pure water; $\phi = 2.6$ for water as solvent

$\propto$: the viscosity of pure water (cP) [8]

T: temperature (K)

M_{water}: molecular weight of pure water (g mol^{-1})

$D_{polymer}$: the diffusivity of polymer in dilute solution in pure water (cm^2 s^{-1})

40 °C

$$\frac{D_{\text{polymer}} \times 0.6527}{313.15} = \frac{7.4 \times 10^{-8}(2.6 \times 18)^{\frac{1}{2}}}{75.6^{0.6}}$$

$$\rightarrow D_{polymer} = 1.81 \times 10^{-5} \text{ (cm}^2\text{/s)}$$

60 °C

$$\frac{D_{\text{polymer}} \times 0.6527}{333.15} = \frac{7.4 \times 10^{-8}(2.6 \times 18)^{\frac{1}{2}}}{75.6^{0.6}}$$

$$\rightarrow D_{polymer} = 2.70 \times 10^{-5} \text{ (cm}^2\text{/s)}$$

The viscosity of pure water is 0.6527 cP at 40 °C, 0.466 cP at 60 °C. The corresponding polymer diffusivities are 1.81×10^{-5} and 2.70×10^{-5} ($cm^2\ s^{-1}$), respectively. To clearly understand these parameters, **Table 2.1** is shown.

Based on theoretical value and experimental value of the density of polymer solution, we have this below equation

40 ℃

$$K_1 = \frac{-0.99845 \times 8.314 \times 313.15}{1.81.10^{-5} \times 760 \times 1.92 \times 10^6 \ln[\frac{(704.7)}{(760 - P_1)}]}$$

$$K_1 = \frac{-0.09828643}{\ln[\frac{(704.7)}{(760 - P_1)}]}$$

From the *Z*-positions in the time course were plotted using "Get Data Graph Digitizer" software, we have the value of z and t, z_0 was measured based on real model (z_0 = 1 mm). Due to we can clarify P_1 and K_1

$$P_1 = 760 - \frac{704.7}{e^{\frac{-0.09828643}{t}\left(\frac{z^2 - z_0^2}{2}\right)}} \quad (2)$$

After we got K_1, we can determine z_1 as the below equation

$$z_1 = \sqrt{\frac{2t}{K_1} + z_0^2}$$

60 ℃

$$K_1 = \frac{-0.98965 \times 8.314 \times 333.15}{2.70.10^{-5} \times 760 \times 1.92 \times 10^6 \ln[\frac{(610.6)}{(760 - P_1)}]}$$

$$K_1 = \frac{-0.06955385}{\ln[\frac{(610.6)}{(760 - P_1)}]}$$

From the *Z*-positions in the time course were plotted using "Get Data Graph Digitizer" software, we have the value of *z* and *t*, z_0 was measured based on real model (z_0 = 1 mm). Due to we can clarify P_1 and K_1

$$P_1 = 760 - \frac{610.6}{e^{\frac{-0.06955385}{t}\left(\frac{z^2 - z_0^2}{2}\right)}} \quad (3)$$

After we got K_1, we can determine z_1 as the below equation

$$z_1 = \sqrt{\frac{2t}{K_1} + z_0^2} \quad (*)$$

Explanation step-by-step (Theoretical evaluation by input of experimental value)

40 ℃

$$K_1 = \frac{-0.99845 \times 8.314 \times 313.15}{1.81.10^{-5} \times 760 \times 1.92 \times 10^6 \ln[\frac{(704.7)}{(760 - P_1)}]}$$

$$K_1 = \frac{-0.09828643}{\ln[\frac{(704.7)}{(760 - P_1)}]} \quad (1')$$

K_1 is still depended on P_1

Combine (1') and (*)

$$t = \frac{-0.09828643}{ln[\frac{(704.7)}{(760 - P_1)}]}\left(\frac{z^2 - z_0^2}{2}\right)$$

60 ℃

$$K_1 = \frac{-0.98965 \times 8.314 \times 333.15}{2.70.10^{-5} \times 760 \times 1.92 \times 10^6 \ln[\frac{(610.6)}{(760 - P_1)}]}$$

$$K_1 = \frac{-0.06955385}{\ln[\frac{(610.6)}{(760 - P_1)}]} \quad (2')$$

K_1 is still depended on P_1

Combine (2') and (*)

$$t = \frac{-0.06955385}{\ln[\frac{(610.6)}{(760 - P_1)}]}\left(\frac{z^2 - z_0^2}{2}\right)$$

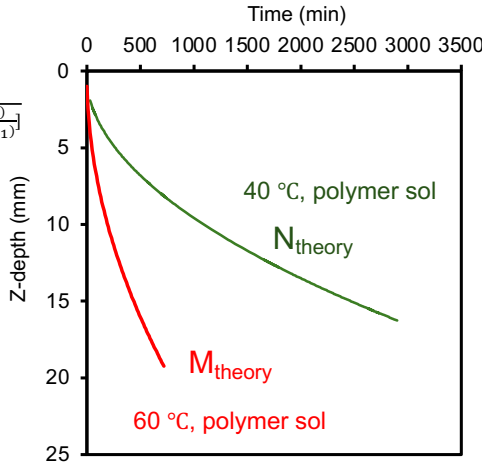

From the *Z*-positions in the time course were plotted using Get Data Graph Digitizer, we determine the value of *z* and *t*, z_0 was measured based on real model.

→ P_1 = … → K_1 = …(based on equation 1')

Note:

z_0 = 1 mm
t: 0 ~ 2900 mins (40 ℃)
t: 0 ~ 720 mins (60 ℃)

$$z_1 = \sqrt{\frac{2t}{K_1} + z_0^2}$$

The actual experimental setup showing pure water and polymer solution at 40 °C (**Fig. 2.5A**) and 60 °C (**Fig. 2.5B**). The experimental data were analyzed using ImageJ software. The formation of a nucleus at 40 °C significantly alters the evaporation process, leading to longer drying times and deviations from the theoretical model. At 60 °C, the system behaves more predictably, aligning with the evaporation behavior of pure water. The separation of drying stages (M, and N) provides a more detailed framework for understanding solvent evaporation in polymer solutions. We evaluate based on temperature dependence of evaporation.

At 60 °C, both theoretical and experimental evaporation curves for polymer solution align closely with those of pure water, indicating a similar evaporation mechanism. At 40 °C, deviations occur due to the formation of a nucleus (N), which affects the evaporation dynamics. This suggests structural changes in polymer solution at lower temperatures. The total evaporation time for polymer solution at 40 °C is around 3000 minutes, significantly longer than the 750 minutes required at 60 °C. This difference is attributed to the lower diffusivity and evaporation coefficient at 40 °C, as well as the influence of nucleus formation **(Fig. 2.6A)**. To better understand the evaporation process at 40 °C, the drying system is divided as shown in **Fig. 2.6B, C, and D)**.

(M, sky blue): Meniscus, theoretical and experimental results align closely, suggesting that these models effectively describe the evaporation process of polymer solution.

(N, green): Nucleus, a concentrated region that forms during drying, affecting mass transport.

The experimental curve significantly deviates from the theoretical prediction, indicating that this model may not accurately capture the evaporation behavior under these conditions. The position P_1 is determined by time (t) and height (z) (as described by **Equation 2, and 3**), indicating that these parameters significantly influence the evaporation dynamics and phase transitions. The given equation describes K_1 as a function of polymer density, gas constant, temperature, polymer diffusivity, atmospheric pressure, and the logarithmic ratio of vapor pressures. A higher temperature increases vapor pressure (P_{water}), reducing the denominator in the logarithmic term and leading to a higher K_1, which accelerates evaporation. At 40 °C, the presence of the nucleus (N) likely reduces effective diffusivity ($D_{polymer}$), slowing down evaporation compared to 60 °C. The formation of a nucleus at 40 °C significantly alters the evaporation process, leading to longer drying times and deviations from the theoretical model. At 60 °C, the system behaves more predictably, aligning with the evaporation behavior of pure water. The separation of drying stages (M, and N) provides a more detailed framework for understanding solvent evaporation in polymer solutions. A fitting curve was developed to better match the experimental observations of N_{exp} and N_{theory}, since a noticeable deviation was observed between the theoretical prediction and experimental data. This fitted model provides a more accurate description of the nucleus behavior throughout the drying process. The

good agreement between the experimental data and the fitting curve confirms the reliability of the model in representing the evaporation dynamics (**Fig. 2.6D**). Besides, P_1 and K_1 are important factors affecting drying process. Notably, before 150 minutes, the polymer slows down evaporation more than the theoretical prediction. At 150 minutes, the polymer behavior aligns well with the theoretical model. However, after 150 minutes, the polymer's ability to retain water decreases, leading to a faster evaporation rate than expected (**Fig. 2.6E, and F**).

Table 2.1. Comparison between 40 ℃, and 60 ℃.

	40 ℃				**60 ℃**	
	Pure water	**Polymer sol**			**Pure water**	**Polymer sol**
		M_{theory}	N_{theory}	Fitting Curve		
P_{atm} (mmHg)	760					
R (J/mol K)	8.314					
T (K)	313.15				333.15	
P_{water} (mmHg)	55.3				149.4	
M (g/mol)	18	1920000			18	1920000
z_0 (mm)	1					
ρ (g/cm^3)	0.992	0.99845			0.983	0.98965
D (cm^2/s)	0.324	1.81×10^{-5}			0.4772	2.70×10^{-5}
P_1 (mmHg)	(only use P_{atm} and P_{water})	49.746	51.882	Change according to time	(only use P_{atm} and P_{water})	138.36
$t_{123...}$ (min)	Time course change					
K_1	0.13	12.632	22.03	Change according to time	0.5248	3.903
z_1 (mm)	Measurement					

Pure water:

-The significant reduction in evaporation time at the higher temperature aligns with the observed increase in vapor pressure and diffusivity.

-The higher K value at 60 ℃ reflects the increased evaporation speed due to the combined effects of higher vapor pressure, greater diffusivity, and reduced density.

Polymer sol:

At 40 ℃, the presence of the nucleus (N) reduces the effective diffusivity, slowing down evaporation compared to 60 ℃.

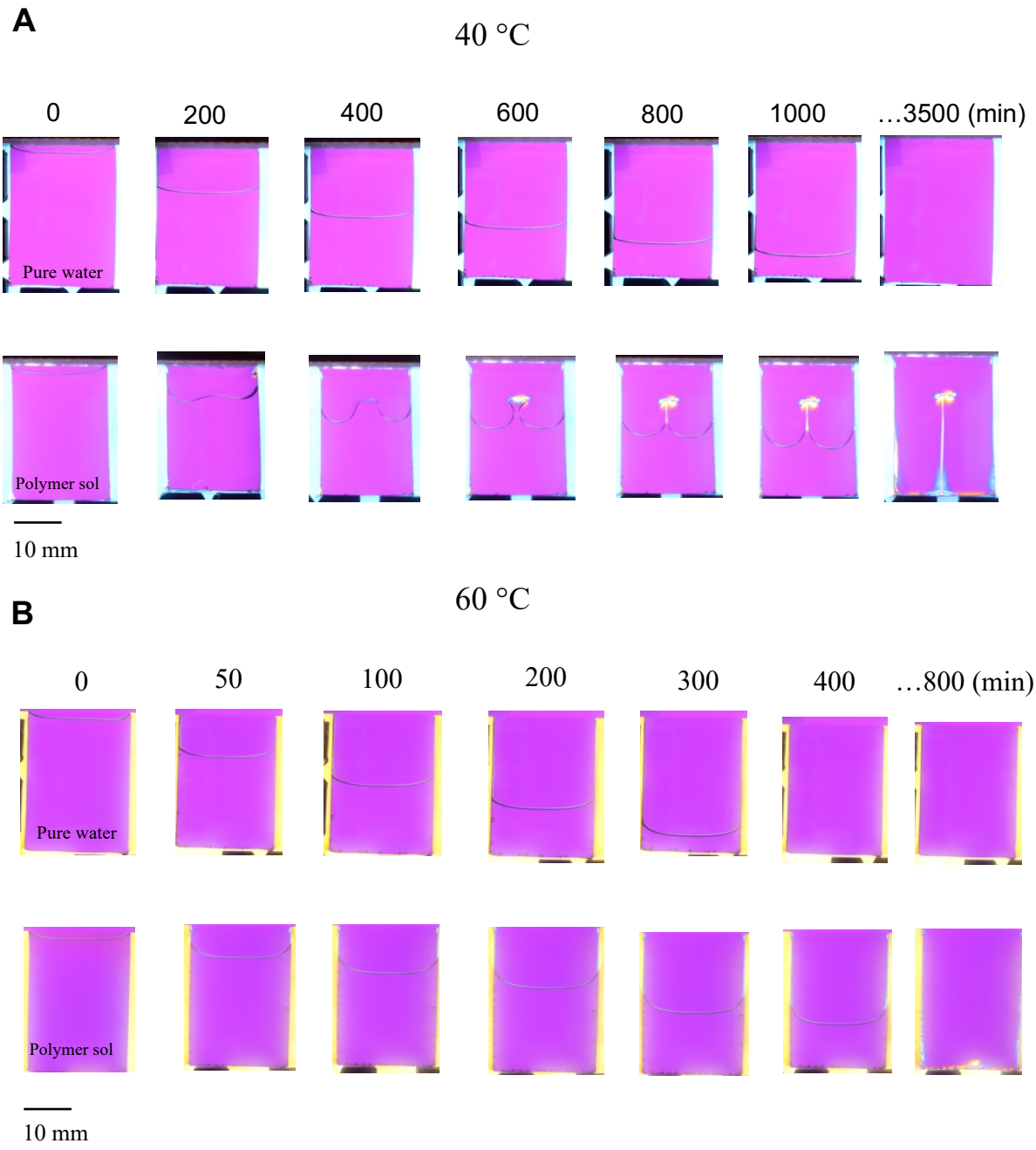

Figure 2.5. The actual model of pure water and polymer solution during evaporation process at 40 °C (A) and 60 °C (B).

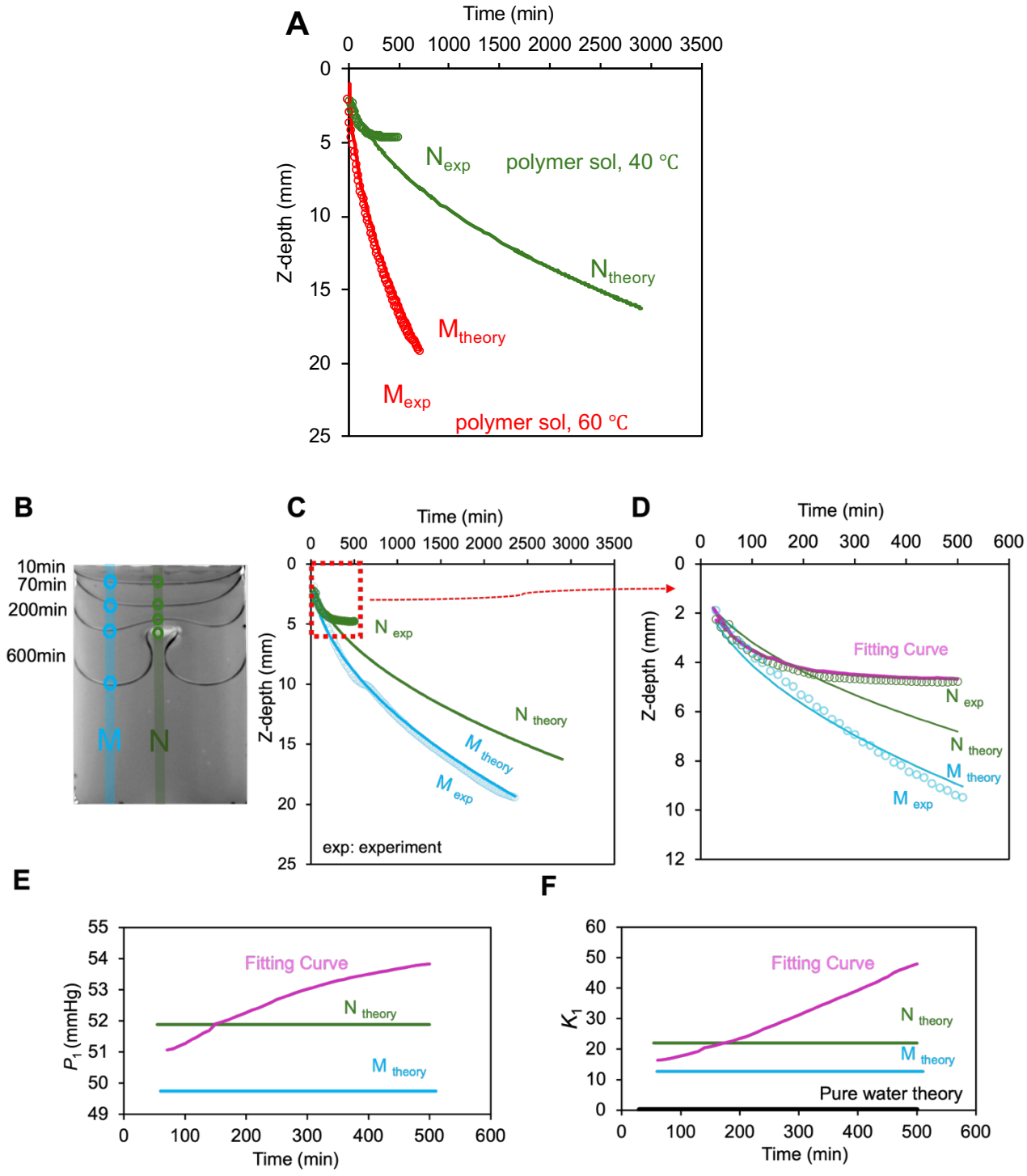

Figure 2.6. These theoretical/experimental curves of polymer solution at 40 and 60 °C (A), and comparation of interface positions at 40 °C (B, C, and D). Two important parameters affecting drying process at 40 °C (E, and F). Initial λ-carrageenan concentration: 1.5 wt.%. Cell dimensions: 15 mm × 1 mm × ~23 mm. The relative humidity was estimated to be 14.2 ± 2.5% RH.

2.3.3. Comparation between theoretical/experimental results

As shown in **Fig. 2.7**, the experimental evaporation curve of polymer solution exhibits a nonlinear trend, in contrast to the evaporation behavior of pure water. This deviation is attributed to the formation of a nucleus during the evaporation process. **Fig. 2.7A** presents experimental measurements for four representative cases, including pure water at 40 °C, pure water at 60 °C, polymer solution at 40 °C, and polymer solution at 60 °C. The results clearly demonstrate that the presence of polymer significantly increases the capillary pressure across the entire saturation range compared to pure water. Additionally, elevating the temperature from 40 °C to 60 °C enhances this effect in both types of liquids. Among the tested conditions, the polymer solution at 60 °C exhibits the highest capillary pressure, indicating a pronounced synergistic influence of polymer concentration and thermal effects on the capillary behavior. These trends suggest that the interfacial properties of the solution are strongly affected by both composition and temperature, likely due to temperature-induced reductions in surface tension and increases in viscosity, as well as molecular-level interactions within the polymer network. **Fig. 2.7B** shows the corresponding theoretical predictions based on the evaporation and capillarity model. The theoretical curves successfully replicate the relative ordering of the four cases observed in the experimental data, capturing the systematic increase in capillary pressure with both polymer addition and temperature elevation. Although slight discrepancies are observed—potentially due to model simplifications or experimental uncertainties—the theoretical trends are in good agreement with the measured data, thereby validating the physical assumptions used in the model. Notably, under conditions involving polymer solution at elevated temperatures, nucleation phenomena were consistently observed during the drying process. These nucleation events are likely driven by enhanced capillary forces and flow confinement effects, which are intensified by both the viscous nature of the polymer solution and the thermal energy input.

Fig. 2.7C and D illustrate the evaporation behavior of pure water at two different temperatures, 40 °C and 60 °C. At 40 °C (**Fig. 2.7C**), the experimental data deviates significantly from the theoretical prediction based on the nucleation model (N_{theory}). This discrepancy is particularly evident in both the evaporation rate constant K_1 and the evaporation pressure P_1, prompting the construction of a fitting curve to better represent the actual behavior. Over time, both K_1 and P_1 show a steady increase, which may be attributed to gradual changes in interfacial conditions or temperature distribution, possibly affecting the nucleation dynamics. In contrast, at 60 °C (**Fig. 2.7D**), the experimental data aligns closely with the theoretical model based on M_{theory}, and no significant deviation is observed throughout the duration of evaporation. Both K_1 and P_1 remain nearly constant, suggesting a stable and uniform evaporation process at higher temperatures, likely due to enhanced thermal energy that overcomes interfacial resistance and stabilizes the phase transition mechanism. These findings confirm that P_1 plays a critical role in the

evaporation process, and the temperature-dependent deviation between experimental and theoretical nucleation rates justifies the need for fitted models, particularly under moderate thermal conditions such as 40 °C.

Overall, the results in **Fig. 2.7** emphasize the critical role of solution composition and temperature in governing capillary pressure behavior during evaporation. This understanding is fundamental to controlling nucleation dynamics and designing self-assembled polymeric membranes with hierarchical structures.

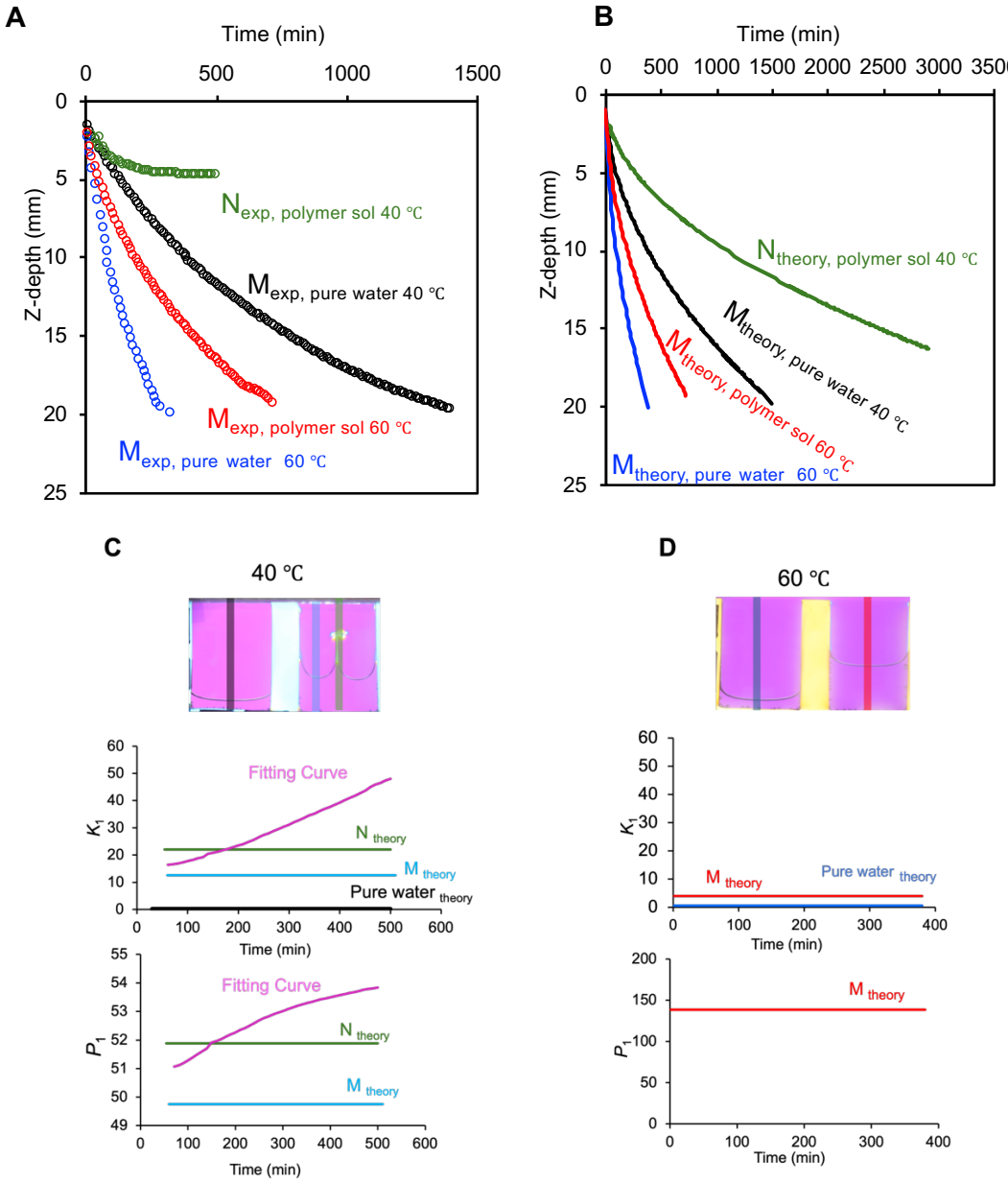

Figure 2.7. The theoretical/experimental curves of pure water and λ-carrageenan at 40 and 60 °C (A, B, C and D). Initial λ-carrageenan concentration: 1.5 wt.%.

2.4. Conclusion

The evaporation behavior of pure water and polymer solution at 40 °C and 60 °C reveals critical differences in drying dynamics. For pure water, the theoretical and experimental evaporation curves are consistent across both temperatures, demonstrating predictable evaporation kinetics. The evaporation time is significantly shorter at 60 °C (approximately 400 minutes) compared to 40 °C (around 1500 minutes), primarily due to increased vapor pressure, higher diffusivity, and enhanced mass transfer at the elevated temperature. In contrast, polymer solution exhibits notable deviations between theoretical and experimental curves at 40 °C, attributed to positional changes within the drying system. These deviations suggest structural transformations during solvent evaporation, including the formation of a nucleus (N1), which alters the drying process by affecting mass transport and phase distribution. This structural complexity extends the evaporation time to approximately 3000 minutes at 40 °C, much longer than that of pure water. However, at 60 °C, the evaporation behavior of polymer solution aligns more closely with that of pure water, indicating a reduced influence of structural rearrangements at higher temperatures. Overall, the findings highlight the significant impact of temperature on evaporation dynamics and structural evolution, particularly in polymer-based systems. The results emphasize the need to consider material-specific transformations when modeling and optimizing drying processes for complex fluids like polymer solution.

References

[1] https://chem.libretexts.org/Bookshelves/Physical_and_Theoretical_Chemistry_Textbook_Maps/Supplemental_Modules_(Physical_and_Theoretical_Chemistry)/Physical_Properties_of_Matter/States_of_Matter/Properties_of_Liquids/Vapor_Pressure
[2] https://www.doubtnut.com/qna/32512261
[3] https://dtrx.de/od/diff/
[4] 5https://www.chegg.com/homework-help/questions-and-answers/vapor-pressure-pure-water-60-c-1494-mmhg-vapor-pressure-60-c-mixture-598-g-sucrose-c12h22o-q106177517
[5] https://labchem-wako.fujifilm.com/us/product/detail/W01W0103-0969.html
[6] https://www.fishersci.com/shop/products/lambda-carrageenan-high-viscosity-tci america/C331325G?fbclid=IwY2xjawJQd6RleHRuA2FlbQIxMAABHaPOZVDqVX_w0DUJQ2RyJbKcTmKAG5RG-VO0g-AZ2LNvxxsIoeKZjYaOQQ_aem_GI56-6xPuJXWb16o5yLtCg
[7] https://www.vip-ltd.co.uk/Expansion/Density_Of_Water_Tables.pdf
[8] Stanley Middleman, An Introduction to mass and heat transfer, principles of analysis and design, John Wiley & Sons, Inc, University of California, San Diego, **1998**.
[9] Danglad-Flores, J.; Eickelmann, S.; Riegler, H. Evaporation behavior of a thinning liquid film in a spin coating setup: Comparison between calculation and experiment. *Eng. Rep.* **2021**, *3*, e12390.
[10] Chang, J.; Cai, J.; Tan, B. Numerical simulation of meniscus evaporation in microchannel based on diffuse interface method. Heat Mass Transf. **2022**, *58*, 1949–1962.
[11] Ruckenstein, E.; Gourisankar, V. S.; Surface restructuring of polymeric solids and its effect on the stability of the polymer—water interface. *J. Colloid Interface Sci*. **1986**, *109*, 557-566.
[12] Reinhard Miller, R.; Joos, P.; Fainerman, V. B. Dynamic surface and interfacial tensions of surfactant and polymer solutions. *Adv. Colloid Interface Sci*. **1994**, *49*, 249-302.
[13] Andrade, J. D.; Chen, W. -Y. Probing polymer surface and interface dynamics. *ECASIA* **1986**.
[14] https://wiki.anton-paar.com/be-en/water/
[15] Wilke, C.; Chang, P. Correlation of diffusion coefficients in dilute solutions. *AIChE*, **1955**, *1*, 264.
https://wiki.anton-paar.com/be-en/water/

Chapter 3

Multiple nuclei formation through symmetry breaking and asynchronous nucleation

3.1. Introduction

In non-equilibrium drying environments in nature, geometric patterns occur through self-organization, such as the spirals seen in flowers. While the growth of these patterns has been explained, understanding of the effects of symmetry/asymmetry on macroscopic geometric structures is still lacking.[1-9] From a soft matter perspective, generation of patterns under physicochemically controlled environments, such as the Saffman-Taylor instability that induces viscous fingering patterns, is feasible.[10-20] Usually, the typical fingering patterns are discussed using a fluid sandwiched between two substrates without boundaries.[14] Through the exploration of transient phenomena, we have identified and studied a phenomenon known as "meniscus splitting".[13-26] Unlike previously reported dissipative structures that transiently exhibit geometric patterns, we successfully identified the environments that support dissipative structures with the formation of polymeric membranes. By evaporating a polymer solution/dispersion in a top-open space with a narrow gap, the polymer is deposited to bridge the gap at specific positions and divide the evaporating meniscus into multiple segments (**Fig. 3.1**). The local polymer concentration at the evaporative interface increases significantly, leading to interface fluctuations during solvent evaporation. The critical condition is that the gap must be less than a capillary length,[27-28] which is typically ~2 mm, and the splitting phenomenon occurs on various hydrophilic/hydrophobic substrates such as glass, plastics, and metals.[29-34] By adjusting the initial polymer concentration, drying temperature, and relative humidity, we observed splitting with a characteristic interval length of approximately 10 mm between the nuclei. This length was largely consistent across different types of polysaccharides, resulting in the formation of self-assembled microfibers or microparticles[35-40]. Furthermore, the deposited polysaccharide membranes are useful as anisotropic soft materials that respond to the water vapor in the air or to the variations in the water pH and in the type of cations in the water.[40-47]

In this chapter, we report that meniscus splitting has physical significance, particularly under conditions for the formation of multiple nuclei. Previous studies for the typical fingering patterns have discussed the averaged characteristic wavelength or treated as the system using symmetric geometries. These treatments are based on the setting of arbitrary positions in infinite space. By contrast, we focus on the asymmetry generated by a space with clear finite dimensions. In particular, the meniscus splitting into two segments is compared to the splitting into three segments. **Fig. 3.1A** illustrates the splitting of the meniscus into three segments through the generation of two nuclei. While multiple nucleations have been reported in previous work, the underlying mechanisms of this process remain unclear. To validate this process, we focused on the stepwise changes in the interfacial fluctuation, highlighting the identification of boundaries (period I) and subsequent stages. Two primary periods were identified: the first nucleation (N1) with symmetry breaking (period II) and the second nucleation (N2) with asynchronous nucleation (period

III). Spatial off-center shifts of the nuclei are commonly observed in experiments, and it is important to consider this phenomenon. As the cell width increased, the position of the nucleus shifted along the width direction (X-direction), and the meniscus split into two or three unequal segments rather than splitting into equal segments (**Fig. 3.1B**). The shift of the X-position of N1 from the center along the X-direction signifies symmetry breaking. Additionally, the splitting of the meniscus into three segments has distinct implications compared to the splitting into two segments. The difference in the depth (position along Z-direction) between N1 and N2 suggests asynchronous deposition. During the three periods, a critical distance for the interval between the nuclei appears to emerge. Based on these results, nucleation is accompanied by symmetry breaking and asynchronous nucleation. To elucidate the positions of the nuclei in physical spaces, the effect of the cell width on the aqueous chitosan dispersions was examined. Notably, the nucleation phenomena were statistically analyzed by assessing the probability of the number of split interfaces, positions of one-nucleus/two-nuclei, and distributions of the nuclei.

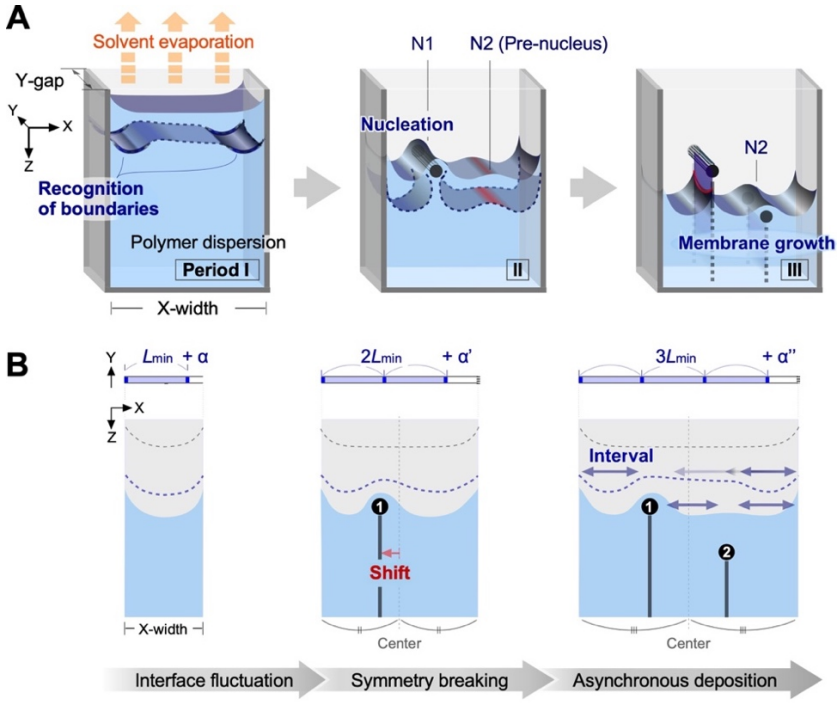

Figure 3.1. Schematic of meniscus splitting through symmetry breaking. **A.** Aqueous polymer dispersion in a Hele-Shaw cell is affected by sidewalls acting as boundaries during evaporation. This occurs due to the interface fluctuations of the polymer, which increase the area for water evaporation. An inhomogeneous concentration at the interface leads to the generation of the first nucleus (N1). In cells with a sufficient width, a second nucleus (N2) forms to bridge the gap. **B.** Hypothesis suggesting that the spatial constraint imposed by cell width influences nuclei positions and stepwise nucleation. As the cell width increases, interface fluctuations, symmetry breaking, and asynchronous nucleation become increasingly prominent. L_{min} indicates the minimum length for the intervals observed in experiments, while *a* denotes lengths shorter than L_{min}.

3.2. Materials and Methods

3.2.1. Materials

Chitosan, poly(D-glucosamine) with a molecular weight (M_w) of 50–190 kDa, was acquired from Merck KGaA (Darmstadt, Germany). The chitosan was 75–85% deacetylated, and the viscosity of the aqueous dispersion was 200–800 cP (1 wt% in 1% acetic acid). This dispersion is known as deacetylated chitin which is categorized as a low-molecular-weight polymer. Acetic acid (99.7%, FUJIFILM Wako Pure Chemical Corporation, Osaka, Japan) was utilized as received. Following the dissolution of the chitosan powder in an aqueous dispersion containing acetic acid, a tiny amount of impurities and air bubbles were eliminated through centrifugation for 30 min at 25 °C and 21,800 × g using a CF15RN centrifuge (Eppendorf Himac Technologies Co., Ltd, Japan) equipped with an angle rotor (Angle Rotor T15A36, Eppendorf Himac Technologies Co., Ltd, Japan).

3.2.2. Drying experiments for statistical analysis

The aqueous dispersion at ~25 °C was transferred into a top-side open cell, specifically the Hele-Shaw cell. These cells were then placed in an oven at a constant temperature under atmospheric pressure using the air circulator of a forced convection system (AS ONE, OFWP-600V). Given that the volume of the oven (600 mm × 497 mm × 500 mm, ~150 L) with the air circulator exceeded that of the samples (< 1 mL), the relative humidity in the oven was regulated by the designated temperature.

3.2.3. Drying experiments for spatiotemporal analysis

The sample in the cell was placed in a ~1 L observation box under controlled temperature and humidity using a temperature-controlled air circulation pump. The internal temperature of the box was controlled using two methods: the first involved connecting a heat pen to a circulating tube, and the second involved attaching a rubber heater to the inner walls of the box. The relative humidity in the box was controlled by maintaining a constant temperature and ensuring air circulation. The correlation between the temperature and relative humidity was verified, confirming the ability to sustain consistent humidity during the drying experiments. Throughout the drying process, the samples were observed through glass windows, and images were captured at certain time intervals (10 min). The interfacial positions (X, Z) were determined by establishing the top corner of the cell as the coordinate origin (O).

3.2.4. *Characterization of aqueous polymer dispersions*

Interfacial tension was determined through pendant drop shape analysis using a contact angle meter (DMs-401, Kyowa Interface Science) at 40 °C and 80% relative humidity. The mass densities of the samples were assessed using a benchtop density meter (DMA4501, Anton Paar). The characterization was conducted at consistent temperatures.

3.3. Results and Discussion

3.3.1. Effect of initial chitosan concentration on deposition nucleation

For the drying experiment, aqueous dispersions of chitosan with a molecular weight (M_w) of 50–190 kDa were poured into a top-side open cell designed as a Hele-Shaw cell with a width of 15 mm. The sample was positioned under atmospheric pressure in a 1-L box with an air circulator at a constant temperature of approximately 40 °C and a constant relative humidity of 20–30% (**Fig. 3.2**). The drying process was observed using cross-polarized light with a first retardation plate ($\lambda = 530$ nm) to monitor the time evolution of the interface position. **Fig. 3.3A** shows the time evolution of the Z-position of the evaporative meniscus on the green line in the inset image (Z_t). Nucleation initiates near the center of the X-width, leading to the splitting of the meniscus into two segments. For Z_t, the time evolution appeared to be smooth immediately before and after nucleation (approximately 5 h). After the nucleus position is fixed, the rate of change in Z_t gradually decreases for 10–15 h. This deceleration occurs because the evaporative interface expands around the nucleus while the bottom of the split interface does not move. Thermal energy is used for solvent evaporation by depositing the condensed polymer at a specific position.

Next, to elucidate the effect of the initial chitosan concentration on meniscus splitting, the spatial position of the evaporative interface and the deposition nucleus were statistically analyzed by performing more than 20 trials for each condition. The probability of nucleation increased significantly when the chitosan concentration C_0 reached 2.0 wt% (**Fig. 3.3B**), and formation of vertical membranes was clearly enhanced for $C_0 \geq 2.0$ wt% **(Fig. 3.3C**). This drastic change indicates that C_0 is a key factor for the splitting phenomena, which also requires appropriate physical parameters, such as the evaporation rate.[47-49] For example, the chitosan concentration increases from 1 to 3 wt% when the volume is reduced to one-third, but the probability of nucleation is ~0%. Statistical analysis suggests that nucleation requires the combination of a chitosan concentration close to the saturating concentration and a high evaporation rate.

Fig. 3.3D shows the distribution of the nucleation positions (X_N, Z_N) following the drying of the chitosan dispersion at varying initial concentrations in a cell with a width of 15 mm. The position data were collected and plotted without any normalization. Nucleation was not observed for the samples with the

initial concentrations of 1.0- and 1.5-wt%. It is considered that even if pre-nuclei are formed in the 1.0- and 1.5-wt% polymer dispersions, they do not bridge the gap to form the nuclei because the evaporation rate is not high enough in the middle of the cell-depth. By contrast, the nucleation positions for the samples with the initial concentrations of 2.0-, 2.5-, and 3.0-wt% are estimated as (7.5 ± 0.8, 6.6 ± 0.5), (7.5 ± 0.2, 6.2 ± 0.4), and (7.5 ± 0.2, 4.5 ± 0.4), respectively. While X_N was mostly located close to the center for all C_0, Z_N decreased with increasing C_0. This finding supports the hypothesis that the polymer bridges the gap and splits the meniscus into two when the dispersion approaches the saturated concentration. Additionally, the X_N were found at the positions between 5 and 10 mm without no X_N at either 0–5 or 10–15 mm ranges, suggesting that the cell walls exert a repulsive force. The balance of the interfacial tension and the capillary force is discussed below. The presence of a single nucleus suggests that the evaporative interface experiences fluctuations involving multiple clusters, akin to the pre-nucleus, which accumulate around the center of the cell width.

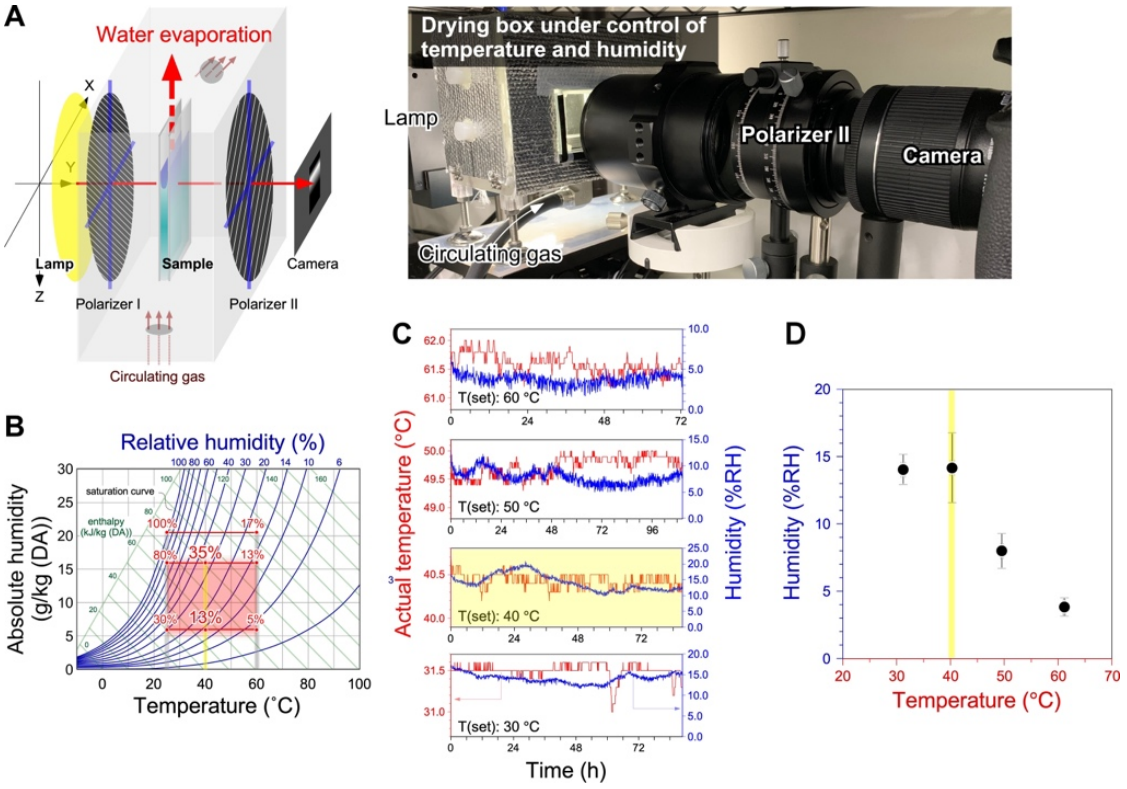

Figure 3.2. Experimental setup for drying tests and observations under cross-polarized light. **A.** The polarizers were set to 45° and 135°. **B.** Standard Mollier diagram for the estimation of the relationship between the temperature and humidity. DA = dry air. **C.** Time course of the actual temperature and relative humidity (RH) in a drying box at a given set temperature. **D.** Relationship between the temperature and RH in a drying box. By measuring the time course of the actual temperature and humidity in the drying box, the RH at 40 °C was estimated to be 14.2 ± 2.5% RH.

Fig. 3.2 presents a comprehensive analysis of the drying conditions to ensure accuracy and reproducibility. These measurements, based on the actual data from the drying box, provide a robust foundation for the experimental conditions and reinforce the reliability of the reported results.

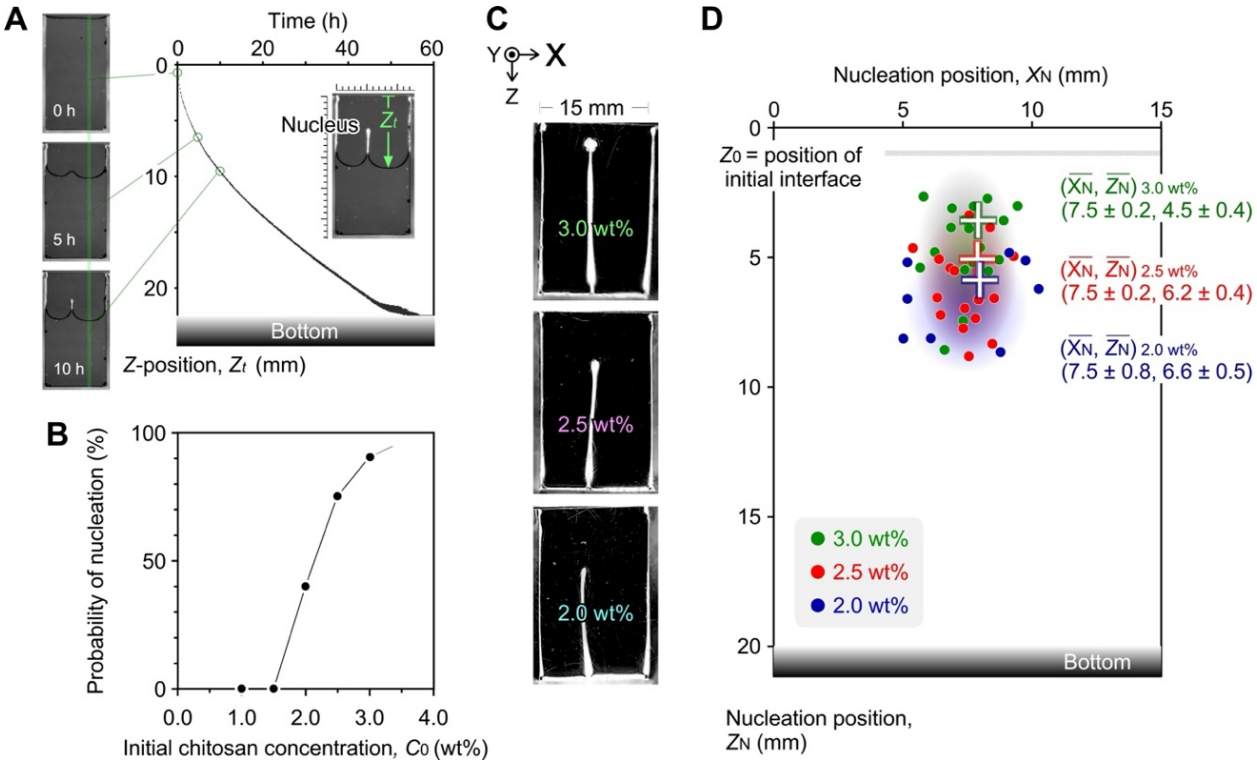

Figure 3.3. Effect of the initial chitosan concentration on deposition nucleation. **A.** Time evolution of the air-liquid interface and nucleation process. **B.** Nucleation probability as a function of initial polymer concentration, based on at least 20 trials for each condition. **C.** Photograph of the deposited vertical membrane formed by drying polymer dispersion with different initial chitosan concentrations from a top-side-open cell (15, 0.5, ~23 mm). Initial acetic acid concentration: 1.0 vol%. Drying temperature: 40 °C. **D.** Statistical analysis of the nucleus position (X_N, Z_N). Circles represent *XZ*-positions observed in individual trials, while crosses denote the average *XZ*-positions.

3.3.2. Effect of cell width on deposition nucleation

To elucidate the effect of cell *X*-width on nucleation, we conducted a statistical analysis of the spatial positions of the nuclei. The results of the analysis are presented in **Fig. 3.4A** and show that the number of nuclei and the number of split interfaces increase with increasing *X*-width. Specifically, when a nucleus originated from the cells with an *X*-width exceeding 15 mm, its position was not fixed at the center but rather was shifted away from the center, indicating a symmetry-breaking process. Moreover, under similar conditions, the occurrence of two nuclei was observed with a significant probability, as demonstrated through a statistical analysis involving over 20 trials for each X-width (**Fig. 3.4B**). This clearly indicates

that a single condition allows multiple possible outcomes for the number of menisci formed during the splitting. For instance, cells with a width greater than 15 mm can yield two menisci with a probability of approximately 60% and three menisci with a probability of approximately 40%. The possibility of different outcomes implies that the evaporative interface contains fluctuating polymers which play a crucial role in deposition nucleation. This scenario is further supported by the symmetry-breaking phenomenon following boundary identification, as shown in **Fig. 3.1A**. The phenomenon of multiple nucleation likely arises due to the accelerating inhomogeneity facilitating pre-nuclei generation with increasing interface length, similar to the observations reported in our previous studies.[47-50]

The nucleation positions (X_N and Z_N) in a cell with a width of 18 mm were analyzed by classifying the cases into the categories of single and double nuclei (**Fig. 3.4C and Fig. 3.5**). For the two nuclei with three split interfaces, the positions of the nuclei ($X_{N1/2}$, $Z_{N1/2}$) and ($X_{N2/2}$, $Z_{N2/2}$) were estimated as statistical averages. Here, the position of the first nucleus, $N_{1/2}$, is defined as being located on the left, with the closer corner at the top serving as the origin. If $N_{1/2}$ appeared to the right of the image center, the left and right sides were interchanged, and the analysis was conducted using the upper-left corner as the origin. The positions for N1/2 and N2/2 were (6.7 ± 0.3, 3.7 ± 0.3) and (11.6 ± 0.3, 11.5 ± 1.3), respectively. The two X_N positions are located close to the third segment of the cell width. This implies that the cell width of 18 mm leads to splitting into three interfaces rather than two interfaces with a probability exceeding 50%. The initial interface does not split from the center ($X = 9$) but rather from the X-positions near the trisection of the cell X-width ($X = 6$ or 12). This indicates that the primary fluctuation at the interface plays a crucial role in determining the nucleation positions. Moreover, sequential growth is a distinctive feature of the development of two nuclei and three menisci. The Z-position of the second nucleus, $Z_{N2/2}$, is notably different from that of the first nucleus ($Z_{N2/2}$ - $Z_{N1/2}$ = 7.8 mm). This discrepancy arises because the first nucleus enhances the attraction of the polymer clusters towards itself, while the second pre-nuclei concurrently reduce this attraction. The gradual increase in the viscosity during drying delays the deposition of the second nucleus. As a result of the deceleration of the growth from the pre-nucleus to the nucleus, $Z_{N2/2}$ was widely distributed. Consequently, symmetry breaking along the X-axis leads to asynchronous deposition along the Z-axis during solvent evaporation.

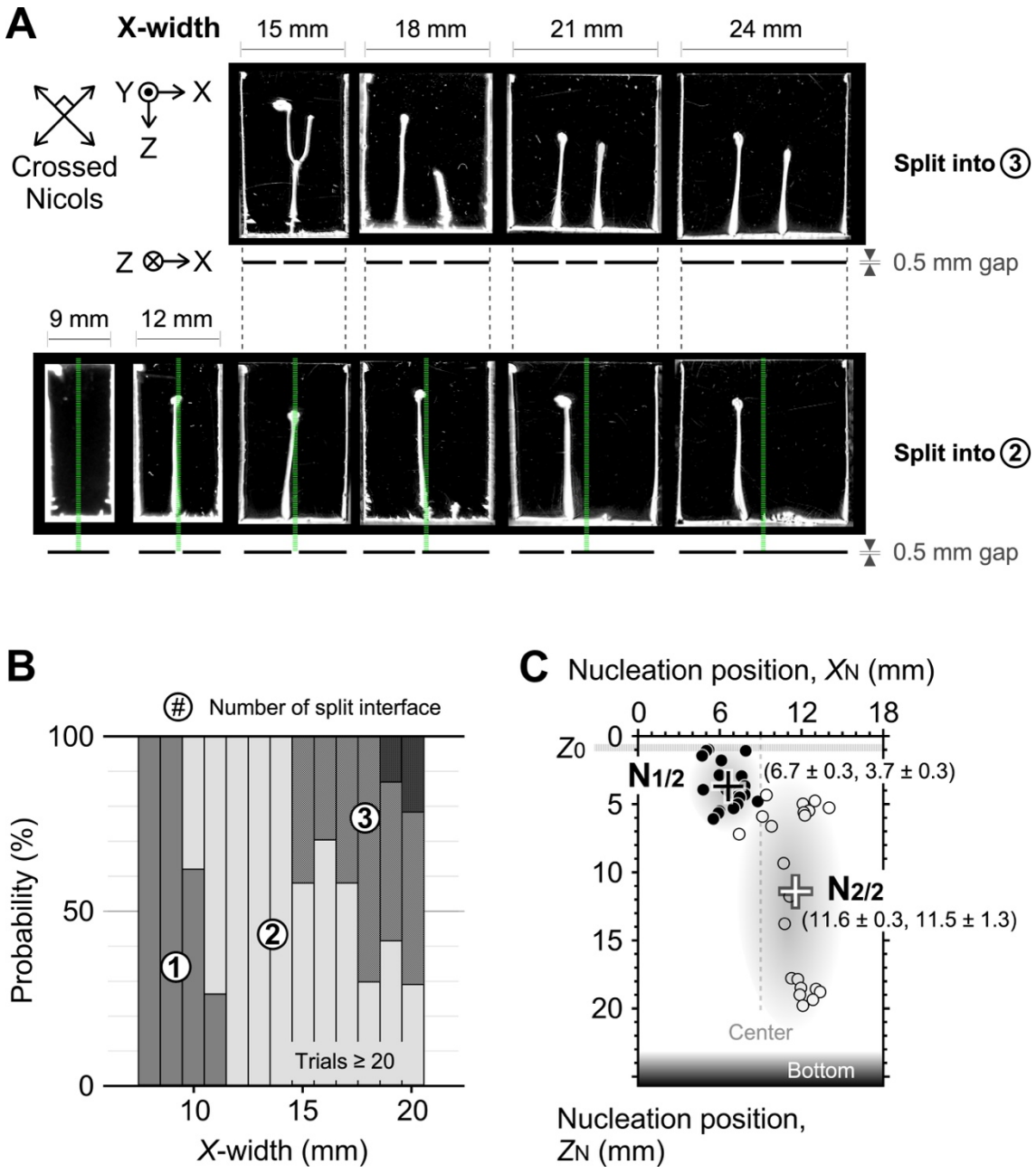

Figure 3.4. Effect of cell width on deposition nucleation. **A.** Images of polymer deposition in cells with specified widths. The green dotted line represents the center of the cell width, while the black horizontal line below the image corresponds to the length of the split interface. Initial chitosan concentration: 2.5 wt%. Initial acetic acid concentration: 1.0 vol%. Cell dimensions: *X*-width × 0.5 mm × ~23 mm. Drying temperature: 40 °C. Numbers within circles denote the number of split interfaces observed. **B.** Probability of split interface formation as a function of cell width, based on more than 20 trials. **C.** Statistical analysis of nucleation positions (X_N, Z_N) for cases of single and dual nuclei formation in a cell with the dimensions of 18 mm × 0.5 mm × ~23 mm. $N_{1/2}$ represents the first nucleus, while $N_{2/2}$ indicates the second nucleus.*

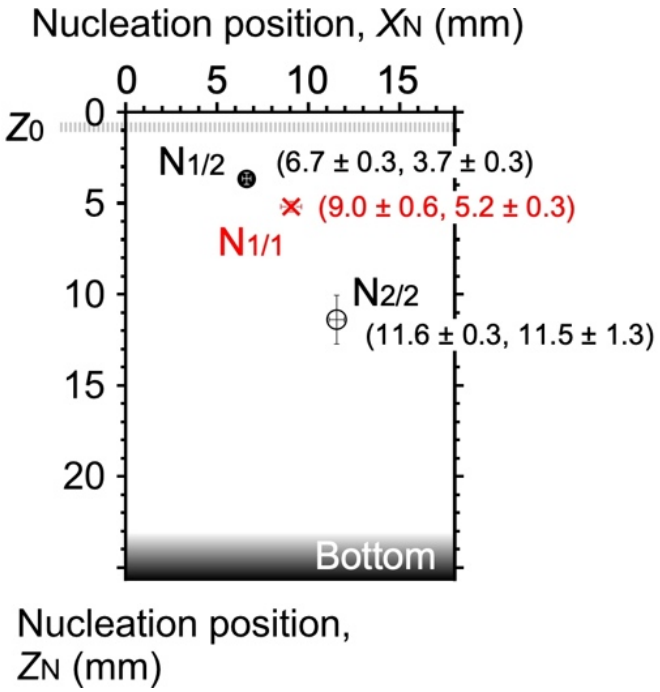

Figure 3.5. Statistical average of the nucleation position (X_N, Z_N) for cases with one nucleus and two nuclei in a cell (dimensions of 18 mm × 0.5 mm × ~23 mm). $N_{1/1}$ represents the nucleus from a single nucleation, while $N_{1/2}$ and $N_{2/2}$ represent the first and second nuclei, respectively, for the case of two nucleations.*

The preparation of the chitosan dispersion by the meniscus splitting method was conducted Meniscus splitting was performed under the following conditions: initial chitosan concentration of 2.5 wt%, initial acetic acid concentration of 1.0 vol%. The cell had a width of 18 mm, a gap of 0.5 mm, and a depth of ~23 mm. Drying temperature: 40 °C The drying temperature was set to 40 °C, and the relative humidity was estimated to be 14.2 ± 2.5% RH. After pouring the chitosan solution into the cell, the cell was placed in the drying oven. The liquid in the samples was mostly evaporated in approximately three days.

3.3.3. Symmetry breaking in meniscus splitting

A comprehensive analysis of the nucleation of the meniscus splitting into two and three segments was carried out. With an increase in the *X*-width from 10 to 20 mm, the shape of the deposited polymer transitioned from no distinct shape to the I-, Y-, and II-shapes (**Fig. 3.6A**). In particular, the 14-mm-wide cell provided an I-shaped deposition with a shift of the nucleus position from the center. This symmetry breaking was studied by plotting the statistical average $X_{N1/1}$ for one nucleus and $X_{N1/2}$ and $X_{N2/2}$ for two nuclei versus the *X*-width of the cell (**Fig. 3.6B, and Fig. 3.7**). When the *X*-width was less than 9 mm, no nucleation was observed; hence, there are no data points for *X*-width less than 9 mm in the graph. By

contrast, when the *X*-width is greater than 10 mm, one nucleus position was observed that was shifted away from the center, with the degree of the shift increasing with increasing *X*-width. Two nuclei are generated for *X*-widths greater than 15 mm. It is noteworthy that the *X*-positions of $N_{1/2}$ are close to those of $N_{1/1}$. The shift for $N_{1/1}$ indicates symmetry breaking and induces the generation of multiple nuclei. This interpretation is supported by the fact that the *X*-positions of $N_{1/2}$ are closer to the center than the *X*-positions of $N_{1/1}$.

Focusing on the induction time period that precedes the nucleation in an 18-mm-wide cell, the deformation of the interfacial line indicated the presence of a pre-nucleus (**Fig. 3.6C**). Monitoring of the time-evolution on the red (x = 14.0 mm) and black lines (x = 15.5 mm) showed that a small pre-nucleus was transiently generated around the position on the red line. The difference between the red/black positions reached approximately 100 μm, despite being less than 10 μm before and after this time period (2–5 h). This result clearly indicates that the polymer clusters beneath the interface form a pre-nucleus at the *X*-position. However, this pre-nucleus could not become a nucleus owing to insufficient conditions. The mechanism of the evaporative interface (*XY*-plane) is summarized in **Fig. 3.6D**. The polymer clusters have almost equal possibilities of becoming pre-nuclei during the fluctuation period. However, the boundaries of the two sidewalls initially affect the curved interfaces, affecting the initial position of the pre-nuclei and the number of nuclei (N1 and N2). The pre-nucleus indicates the presence of a large polymer cluster but does not bridge the gap. If the pre-nucleus for N3 appears during the induction period, it will disappear because the polymer clusters are attracted to and are integrated into the solidified N1 or N2 with a stronger capillary force.

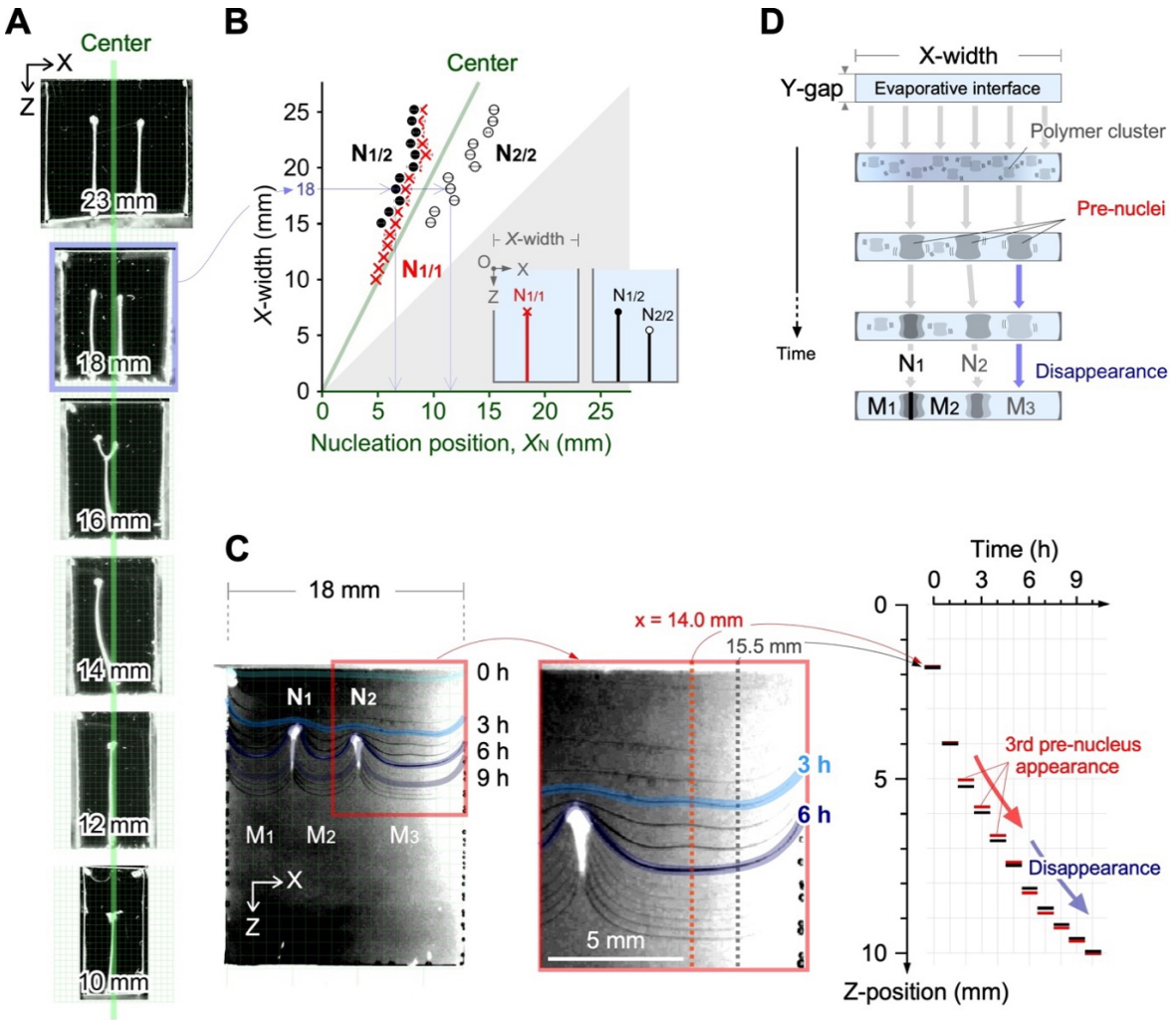

Figure 3.6. Symmetry breaking in meniscus splitting. **A.** Deposited membranes in cells with specified *X*-widths. The green line indicates the center of the cell width. Initial chitosan concentration: 2.5 wt%. Initial acetic acid concentration: 1.0 vol%. Cell dimensions: *X*-width × 0.5 mm × ~23 mm. Drying temperature: 40 °C. **B.** Statistical average of the nucleation position, X_N, as a function of *X*-width. $N_{1/1}$ represents a nucleus for single nucleation. $N_{1/2}$ and $N_{2/2}$ correspond to the first and second nuclei of systems with two nucleations, respectively. More than 15 trials were conducted for each condition. **C.** Time-evolution of meniscus splitting in a cell with a width of 18 mm focusing on area M3, where the appearance and disappearance of the third pre-nucleus (M3) can be observed. **D.** Schematic of the temporal changes at the evaporative interface. During the induction period, polymer clusters fluctuate and form multiple pre-nuclei that do not bridge the gap. Once a nucleus is formed, the growth of subsequent pre-nuclei slows down, leading to asynchronous nucleation.*

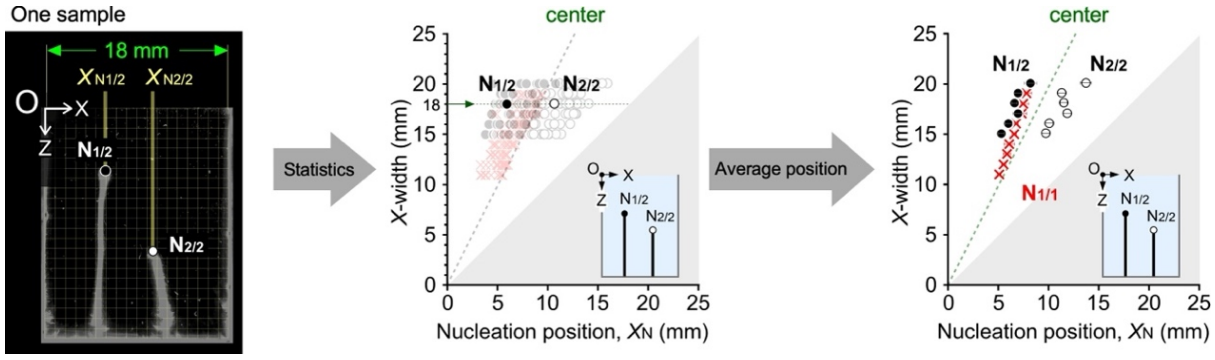

Figure 3.7. Procedure for the statistical analysis.*

3.3.4. Meniscus splitting through symmetry maintaining/breaking for synchronous/asynchronous nucleation

During the splitting process, a characteristic interval along the *X*-direction was observed between the nuclei. Interestingly, the nucleation does not start from the middle of the cell width but rather exhibits a stepwise growth. To discuss the generation of multiple nuclei, the geometric consideration of the conditions that enable the generation of the three menisci is discussed by focusing on the characteristic periods (**Fig. 3.8**): I) The effect of the boundaries by the deformation of the meniscus near the two side walls, II) simultaneous nucleation while preserving symmetry, or relaxation of one pre-nucleus growth with asymmetrical nucleation, and III) membrane growth from nuclei vertically to the initial meniscus as a quasi-stable step. The multiple pre-nuclei grow with intervals above a certain distance and either synchronous or asynchronous nucleation occurs. On the other hand, when the multiple growing pre-nuclei are separated by an interval below a certain distance, the boundaries of the closest two nuclei gradually come closer and the pre-nuclei finally fuse into a single nucleus because of the strong capillary force between them. A branching model would be helpful for understanding the time evolution of the different cases. While synchronous branching preserve symmetry, asynchronous branching induces symmetry breaking.

Based on the experimental results, the concave curvature was deformed by the effect of the two boundaries in period I. The concave curves can be approximated by elliptic curves with diameter D (**Fig. 3.9**), which has the minimum value D_{min}. This value should be defined based on the capillary length, l_{cap}, which is controlled by the interfacial tension. The difference in interfacial tension on a hydrophilic glass surface and a hydrophobic PDMS surface, as shown in **Fig. S1, S2, and S3**, and the density at the evaporative interface also contribute to this value[27]

$$D_{min} \approx 2l_{cap} = 2\sqrt{\frac{\gamma}{g\Delta\rho}} \quad (1)$$

where γ is the interfacial tension, g is the gravitation acceleration, and $\Delta\rho$ is the mass density difference between the two phases. The D_{min} value is approximately twice that of l_{cap} for typical polymer solutions/dispersions ($D_{min} \approx 2l_{cap}$), as follows. l_{cap} provides a rough estimate of the effective distance from the wall and the meniscus curve is approximated as an exponential. When the liquid is confined between two walls, it is affected by both walls. For lower distances between the two walls, the meniscus curve can be approximated as an elliptic curve. This means that the curve transitions from hyperbolic into elliptic when the distance is closing to $2l_{cap}$. Therefore, $2l_{cap}$ is a natural approximation for the critical diameter of a droplet or particle. In the application of this argument in the present study, the pre-nucleus on the interface can act as the second wall. The l_{cap} of water at room temperature was calculated using Equation (1) ($\gamma \approx 70$ mN m^{-1}, $g = 9.8$ m s^{-2}, $\Delta\rho \approx 1000$ kg m^{-3}), resulting in a value of 2.7 mm. Based on this, the typical value for the air-water interface is in the range of 2–3 mm, which is a physical limit set by capillarity.[26-27] Similarly, D_{min} can be estimated to be twice that of l_{cap} and thus equal to 4–6 mm. The value of D_{min} for the meniscus splitting in the 2.5 wt% chitosan sample in 1 v/v% acetic acid at 40 °C was calculated from the experimental values using Equation (1) ($\gamma = 67.6$ mN m^{-1}, $g = 9.8$ m s^{-2}, $\rho_{sol} = 1.00466$ g mL^{-1}, $\rho_{air} = 1.13$ kg m^{-3}), resulting in a value of 5.24 mm. This value is sufficiently close to the actual intervals between the nuclei, L_{min}, in the meniscus splitting and membrane growth.

When the polymer dispersion is dried from a cell with a narrow gap < l_{cap}, the polymer forms clusters for deposition and bridges the gap at multiple X-positions. Rapid drying and the use of polymers with low moisture retention at the interface lead to the formation of a lid in the center of the cell, causing the evaporative interface to expand at the two boundaries. Subsequently, the polymer is deposited as a membrane and grows in the Z-direction without undergoing the processes of period II. To prevent lid formation, various methods can be employed, such as reducing the initial polymer concentration, decreasing the evaporation rate, and increasing the gap size.

By contrast, when the polymer retained sufficient moisture, a clear period II was distinctly observed. The evaporative interface preserved the inhomogeneity of the polymer density while it was affected by the capillary force arising from the boundary wall. This inhomogeneity enhances the generation of a wavy interface, facilitating mass/heat flows beneath the interface. Near the interfacial curves at approximately $2l_{cap}$, the polymer remained stable in the *X*-position and filled the gap. Two scenarios arise: preserving symmetry through synchronous nucleation and breaking symmetry leading to asynchronous nucleation. To maintain symmetry, the polymer clusters at two *X*-positions simultaneously form independent nuclei with an interval exceeding D_{min}. However, real-world processes often lead to symmetry breaking. The polymer density beneath the interface became more inhomogeneous during the initial polymer deposition on N1. Upon N1 generation, the dense polymer around N2 is attracted to N1, causing the rate of the increase in the

polymer density around the N2 to decrease. This amplification of inhomogeneity triggers symmetry breaking.

In the drying of the polymer dispersion from a cell with a width of $3D_{min}+a$, splitting into four interfaces was seldom observed. This is because the pre-nuclei within D_{min} are repelled by interfacial tension. As a result, we observed pre-nuclei disappearance or fusion with the adjacent nucleus. As an example, as shown in **Fig. 3.6C**, the splitting into three rather than four nuclei can be explained by the effect of D_{min} (18 mm/3 = 6 mm > D_{min}, 18 mm/4 = 4.5 mm < D_{min}). One of the pre-nuclei could not become a nucleus and relaxed and disappeared because the interval adjacent to the nucleus was less than D_{min}. It is difficult for nucleation to occur with an interval of less than D_{min}. Thus, the condition of $3D_{min} < X\text{-width} < 4D_{min}$, such as 18 mm, allows one meniscus to settle into three split menisci.

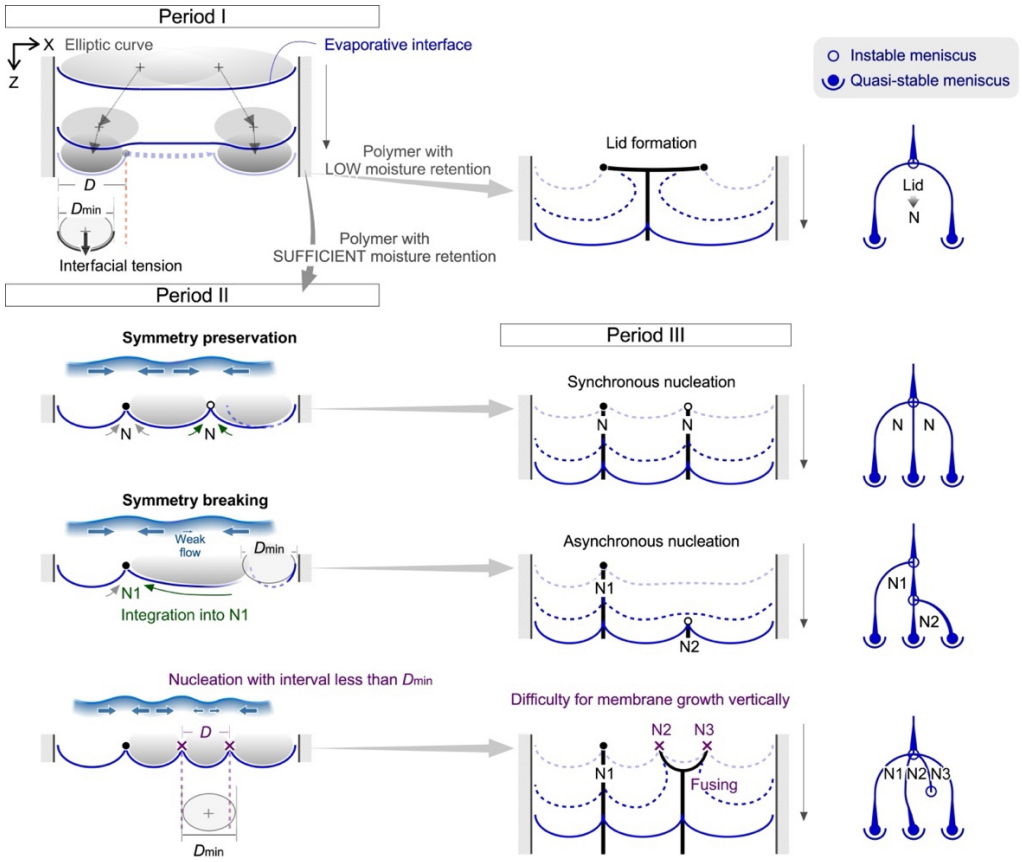

Figure 3.8. Meniscus splitting through symmetry preservation/breaking for synchronous/asynchronous nucleation. Schematics of the splitting process into three menisci with a high probability. Period I: Initial meniscus deformation near the two boundaries, forming an elliptic curve. Period II: Instable meniscus showing both symmetry preservation and symmetry breaking. Period III: Membrane growth as a quasi-stable process. D represents the diameter of the ellipse fitting the interface, while D_{min} is the minimum diameter at which the interface can form. N1 and N2 represent the first and second nuclei, respectively. The schematics on the right show the branching model for each case.

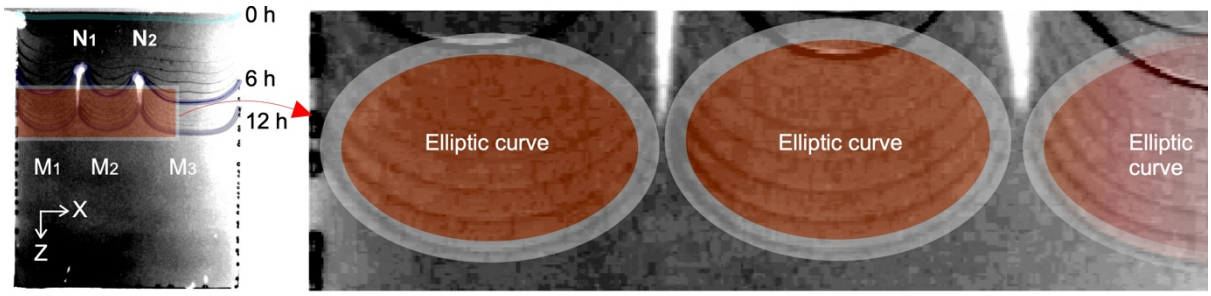

Figure 3.9. Time-lapse observation of meniscus splitting. Initial chitosan concentration: 2.5 wt%. Initial acetic acid concentration: 1.0 vol%. Cell dimensions: 18 mm, 0.5 mm, ~23 mm. Drying temperature: 40 °C.*

3.4. Conclusion

In conclusion, meniscus splitting with multiple nucleations was demonstrated by focusing on deviations from symmetry and synchronicity. Using an aqueous chitosan dispersion, these phenomena were statistically analyzed and explored in detail by controlling the initial polymer concentration and the width of the Hele-Shaw cell. The study revealed that single nucleation with a shift away from the center of the cell width clearly indicated the symmetry breaking of the splitting, and the position of the deposited nucleus was asymmetric. This asymmetry is also reflected in asynchronous nucleation during the generation of two nuclei. These features arise from the non-equilibrium condition at the evaporative interface which undergoes drying into the upper layer and wetting from underneath. The condensed polymer at the interface could undergo hydration and dehydration. Initially, after evaporation begins, multiple pre-nuclei can grow, and some are selected or integrated into several points with an interval greater than twice the capillary length. Considering that the interface curve can be fitted by an elliptical arc, the length of the major axis of the elliptic arc is the interval between the nuclei. The interfacial tension between the air and dispersion is a significant factor affecting this interval. This simple exploration of the splitting process contributes to the fundamental understanding of the symmetry breaking and asynchronous generation of dissipative structures. In addition, by precisely controlling the drying conditions of the dispersions, the characteristic polymer deposition through solvent evaporation can be elucidated, similar to the crystal growth of small molecules. These insights pave the way for the practical applications of symmetry breaking in designing and optimizing polymer-based materials and processes.[42-43, 49] Furthermore, the physical demonstrations carried out in this study are beneficial for the development of understanding of pattern formation by using neural networks,[51, 52] data sciences,[53] numerical simulations,[54] based on mathematical sciences.

References

[1] Zhang, Q.; Amooie, M. A.; Bazant, M. Z.; Bischofberger, I. Growth Morphology and Symmetry Selection of Interfacial Instabilities in Anisotropic Environments. *Soft Matter* **2021**, *17*, 12021209.
[2] Zhang, Q. et al. Dendritic Patterns from Shear-Enhanced Anisotropy in Nematic Liquid Crystals. *Sci. Adv.* **2023**, *9*, eabq6820.
[3] Palmer, A. R. Symmetry Breaking and the Evolution of Development. *Science* **2004,** *306*, 828–833.
[4] Li, B.; Jia, F.; Cao, Y. P.; Feng, X. Q.; Gao, H. Surface Wrinkling Patterns on a Core-Shell Soft Sphere. *Phys. Rev. Lett.* **2011**, *106*, 234301.
[5] Deegan, R. D.; Bakajin, O.; Dupont, T. F.; Huber, G.; Nagel, S. R.; Witten, T. A. Contact Line Deposits in an Evaporating Drop. *Phys. Rev. E* **2000**, *62*, 756–765.
[6] Sang, Y.; Liu, M. Symmetry Breaking in Self-Assembled Nanoassemblies. *Symmetry* **2019**, *11*, 950.
[7] Gibb, C. J.; Hobbs, J.; Nikolova, D. I.; Raistrick, T.; Berrow, S. R.; Mertelj, A.; Osterman, N.; Sebastián, N.; Gleeson, H. F.; Mandle, R. J. Spontaneous Symmetry Breaking in Polar Fluids. *Nat. Commun.* **2024**, *15*, 5845.
[8] Herczyński, A.; Zenit, R. Symmetry and Symmetry-Breaking in Fluid Dynamics. *Symmetry* **2024**, *16*, 621.
[9] Stoop, N.; Lagrange, R.; Terwagne, D.; Reis, P. M.; Dunkel, J. Curvature-Induced Symmetry Breaking Determines Elastic Surface Patterns. *Nat. Mater.* **2015***, 14*, 337–342.
[10] Tagliazucchi, M.; Weiss, E. A.; Szleifer, I. Dissipative Self-Assembly of Particles Interacting Through Time-Oscillatory Potentials. *Proc. Natl Acad. Sci. U. S. A.* **2014**, *111*, 9751–9756.
[11] Fialkowski, M.; Bishop, K. J. M.; Klajn, R.; Smoukov, S. K.; Campbell, C. J.; Grzybowski, B. A. Principles and Implementations of Dissipative (Dynamic) Self-Assembly. *J. Phys. Chem. B* **2006**, *110*, 2482–2496.
[12] Kumar, P.; Horváth, D.; Tóth, Á. Self-Assembly to Synchrony of Active Gels. *Soft Matter* **2023**, *19*, 4137–4143.
[13] Bihi, I.; Baudoin, M.; Butler, J. E.; Faille, C.; Zoueshtiagh, F. Inverse Saffman-Taylor Experiments with Particles Lead to Capillarity Driven Fingering Instabilities. *Phys. Rev. Lett.* **2016**, *117*, 034501.
[14] Song, W. et al. Spontaneous fingering between miscible fluids. *Colloids and Surfaces A* **2020**, *584*, 123943.
[15] Anne-Déborah C. Nguindjel, Pieter J. de Visser, Mitch Winkens and Peter A. Korevaar. Spatial programming of self-organizing chemical systems using sustained physicochemical gradients from reaction, diffusion and hydrodynamics. *Phys. Chem. Chem. Phys.*, **2022**, *24*, 23980-24001.
[16] Eslami, A.; Basak, R.; Taghavi, M. S. Multiphase Viscoplastic Flows in a Nonuniform Hele-Shaw Cell: A Fluidic Device to Control Interfacial Patterns. *Ind. Eng. Chem. Res.* **2020,** *59*, 4119-4133.
[17] Suzuki, R. X.; Tada, H.; Hirano, S.; Ban, T.; Mishra, M.; Takeda, R.; Nagatsu, Y. Anomalous patterns of Saffman–Taylor fingering instability during a metastable phase separation. *Phys. Chem. Chem. Phys.*, **2021**, *23*, 10926-10935.
[18] Islam, T.u.; Gandhi, P. S. Viscous Fingering in Multiport Hele Shaw Cell for Controlled Shaping of Fluids. *Sci Rep* **2017**, *7*, 16602.
[19] Suzuki, R. X.; Nagatsu, Y.; Mishra, M.; Ban, T. Fingering pattern induced by spinodal decomposition in hydrodynamically stable displacement in a partially miscible system. *Phys. Rev. Fluids* **2019**, *4*, 104005.
[20] Gallaire, F.; Brun, P-. T. Fluid dynamic instabilities: theory and application to pattern forming in complex media. *Phil. Trans. R. Soc. A* **2017**, *375*: 20160155.
[21] Rudge, J. F.; McKenzie, D. A Crystallographic Approach to Symmetry-Breaking in Fluid Layers. *J. Fluid Mech.* **2024**, 989.

[22] Dickinson, E. Structure and Rheology of Colloidal Particle Gels: Insight from Computer Simulation. *Adv. Colloid Interface Sci.* **2013**, *199–200*, 114–127.
[23] Eljaouhari, A. A.; Müller, R.; Kellermeier, M.; Heckmann, K.; Kunz, W. New Anisotropic Ceramic Membranes from Chemically Fixed Dissipative Structures. *Langmuir* **2006**, *22*, 11353–11359.
[24] Liu, X.; Farahi, G.; Chiu, G. L.; Papic, Z.; Watanabe, K.; Taniguchi, T.; Zaletel, M. P.; Yazdani, A. Visualizing Broken Symmetry and Topological Defects in a Quantum Hall Ferromagnet. *Science* **2022***, 375*, 321–326.
[25] Okeyoshi, K.; Okajima, M. K.; Kaneko, T. Milliscale Self-Integration of Megamolecule Biopolymers on a Drying Gas–Aqueous Liquid Crystalline Interface. *Biomacromolecules* **2016**, *17*, 2096–2103.
[26] Okeyoshi, K. DRY & WET: Meniscus Splitting from a Mixture of Polysaccharides and Water. *Polym. J.* **2020**, *52*, 1185–1194.
[27] Aarts, D. G. A. L. Capillary Length in a Fluid−Fluid Demixed Colloid−Polymer Mixture. *J. Phys. Chem. B* **2005***, 109*, 7407–7411.
[28] de Gennes, P. G.; Brochard-Wyart, F.; Quéré, D. *Capillarity and Wetting Phenomena: Drops, Bubbles, Pearls, Waves*; Springer, 2003.
[29] Okeyoshi, K.; Yamashita, M.; Budpud, K.; Joshi, G.; Kaneko, T. Convective Meniscus Splitting of Polysaccharide Microparticles on Various Surfaces. *Sci. Rep.* **2021**, *11*, 767.
[30] Yong, J.; Chen, F.; Yang, Q.; Huo, J.; Hou, X. Superoleophobic surfaces. *Chem. Soc. Rev.*, **2017**, *46*, 4168-4217.
[31] Antonov, D.V.; Islamova, A.G.; Strizhak, P.A. Hydrophilic and Hydrophobic Surfaces: Features of Interaction with Liquid Drops. *Materials* **2023**, *16*, 5932.
[32] Feng, W.; Ueda, E.; Levkin, P. A. Droplet Microarrays: From Surface Patterning to High-Throughput Applications. *Adv. Mater*. **2018**, *30*, 1706111.
[33] Mondal, B.; Mac Giolla Eain, M.; Xu, Q. F.; Egan, V. M.; Punch, J.; Lyons. A. M. Design and Fabrication of a Hybrid Superhydrophobic–Hydrophilic Surface That Exhibits Stable Dropwise Condensation. *ACS Appl. Mater. Interfaces*. **2015**, *7*, 23575-23588.
[34] Fei, L.; He, Z.; LaCoste, D. J.; Nguyen, H. T.; Sun, Y. A Mini Review on Superhydrophobic and Transparent Surfaces. *Chem. Rec*. **2020**, *20*, 1257.
[35] Bai, L.; Liu, L.; Esquivel, M.; Tardy, B. L.; Huan, S.; Niu, X.; Liu, S.; Yang, G.; Fan, Y.; Rojas. O. J. Nanochitin: Chemistry, Structure, Assembly, and Applications. *Chem. Rev.* **2022**, *122*, 11604-11674.
[36] Zargartalebi, H.; Hejazi, S. H.; Sanati-Nezhad, A. Self-assembly of highly ordered micro- and nanoparticle deposits. *Nat Commun* **2022**, *13*, 3085.
[37] Li, M.; Jiang, L.; Li, X.; Li, T.; Yi, P.; Li, X.; Zhang, L.; Li, L.; Wang, Z.; Zhang, X.; Wang, A.; Li, J. Wide-Size Range and High Robustness Self-Assembly Micropillars for Capturing Microspheres. *ACS Appl. Mater. Interfaces* **2024**, *16*, 23904-23913.
[38] Gericke, M. et al. The European Polysaccharide Network of Excellence (EPNOE) research roadmap 2040: Advanced strategies for exploiting the vast potential of polysaccharides as renewable bioresources. *Carbohydr. Polym*. **2024**, *326*, 121633.
[39] Mirza, I.; Saha, S. Biocompatible Anisotropic Polymeric Particles: Synthesis, Characterization, and Biomedical Applications. *ACS Applied Bio Materials* **2020**, *3*, 8241-8270.
[40] Etale, A.; Onyianta, AJ.; Turner, SR.; Eichhorn, SJ. Cellulose: A Review of Water Interactions, Applications in Composites, and Water Treatment. *Chem Rev*. **2023**, *123*, 2016-2048.
[41] Budpud, K.; Okeyoshi, K.; Okajima, M. K.; Kaneko, T. Vapor-Sensitive Materials from Polysaccharide Fibers with Self-Assembling Twisted Microstructures. *Small* **2020**, *16*, e2001993.
[42] Saito, I.; Wu, L.; Hara, M.; Ikemoto, Y.; Kaneko, T.; Okeyoshi, K. Anisotropic Responses with Cation Selectivity in Hierarchically Ordered Polysaccharide Networks. *ACS Appl. Polym. Mater.* **2022**, *4*, 7054–7060.

[43] Nguyen, T. K. L.; Tonomura, Y.; Ito, N.; Yamaji, A.; Matsuba, G.; Hara, M.; Ikemoto, Y.; Okeyoshi, K. Reconstruction of Chitosan Network Orders Using the Meniscus Splitting Method for Designing pH-Responsive Materials. *Langmuir* **2024**, *40*, 11927–11935.

[44] Nguyen, T. D.; Peres, B. U.; Carvalho, R. M.; MacLachlan, M. J. Photonic Hydrogels from Chiral Nematic Mesoporous Chitosan Nanofibril Assemblies. *Adv. Funct. Mater.* **2016**, *26*, 2875–2881.

[45] Okeyoshi, K.; Okajima, M. K.; Kaneko, T. Emergence of Polysaccharide Membrane Walls Through Macro-space Partitioning via Interfacial Instability. *Sci. Rep.* **2017**, *7*, 5615.

[46] Chen, M.; Chen, J.; Liu, S.; He, D.; Wang, Y.; Chen, H.; Jin, D.; Ma, X. Multiprogrammable Anisotropic Soft Material via Magneto-Orientation of Ferromagnetic Nanoplates. *Adv. Funct. Mater.* **2024**, *34*, 2411036.

[47] Wang, R.; Feng, Y.; Li, D.; Li, K.; Yan, Y. Towards the sustainable production of biomass-derived materials with smart functionality: a tutorial review. *Green Chem.*, **2024**, *26*, 9075-9103.

[48] Okeyoshi, K.; Joshi, G.; Okajima, M. K.; Kaneko, T. Formation of Polysaccharide Membranes by Splitting of Evaporative Air-LC Interface. *Adv. Materials Inter.* **2018**, *5*, 1701219.

[49] Joshi, G.; Okeyoshi, K.; Mitsumata, T.; Kaneko, T. Micro-deposition Control of Polysaccharides on Evaporative Air-LC Interface to Design Quickly Swelling Hydrogels. *J. Colloid Interface Sci.* **2019**, *546*, 184–191.

[50] Wu, L.; Saito, I.; Hongo, K.; Okeyoshi, K. Recognition of Spatial Finiteness in Meniscus Splitting Based on Evaporative Interface Fluctuations. *Adv. Materials Inter.* **2023**, *10*, 2300510.

[51] G. Rajchakit, R. Sriraman, N. Boonsatit, P. Hammachukiattikul, C. P. Lim, P. Agarwal, Global exponential stability of Clifford-valued neural networks with time-varying delays and impulsive effects. *Adv. Differ. Equ.* **2021**, *2021*, 208.

[52] G. Rajchakit, R. Sriraman, N. Boonsatit, P. Hammachukiattikul, C. P. Lim, P. Agarwal, Exponential stability in the Lagrange sense for Clifford-valued recurrent neural networks with time delays. *Adv. Differ. Equ.* **2021**, *2021*, 256.

[53] X. Wang, J. Shi, G. Zhang, Bifurcation and pattern formation in diffusive Klausmeier-Gray-Scott model of water-plant interaction. *J. Math. Anal. Appl*. **2021**, *497*, 124860.

[54] E. N. M. Cirillo, R. Lyons, A. Muntean, S. A. Muntean, Pattern formation in three–state systems: Toward understanding morphology formation in the presence of evaporation. *arXiv* **2024**, 2405.16459v1.

∗ Data were partially taken by the Laboratory's members.

Chapter 4

Anisotropic swelling/deswelling chitosan hydrogel using meniscus splitting method

4.1. Introduction

As natural polymers, polysaccharides are expected to be alternative materials in the wide fields of food packaging, functional foods, drug delivery, cosmetics, agriculture, and others toward a sustainable society. In contrast to synthetic polymers, such as polyvinyl alcohol and polyacrylamide, natural polysaccharides, such as cellulose and chitosan, are widely researched as safe sources for human bodies and the global environment.[1–4] Chitosan is a product of deacetylated chitin, which is extracted from the exoskeletons of crustaceans and insects and fungal cell walls. Unlike most polysaccharides, chitosan is a cationic polymer with a positive charge that has attracted the attention of numerous researchers in various biomedical fields, such as wound healing, hemodialysis membranes, drug and gene delivery systems, implant coating, and tissue engineering/regeneration.[5–6] In the side chain, amino and hydroxyl groups can be employed as cross-linkable groups. Amino groups can be protonated to ammonium groups below pH 6.4, rendering chitosan a pH-responsive soft material.[7–8] However, hierarchically architectured microstructures of chitosan with anisotropy from bundles of nanofibers have not been utilized with pH-responsiveness. To use these self-assembled structures and their pH-responsiveness, a preparation methodology is required.

Recently, several methods, such as pre-stretching and drying,[9] directional freezing,[10] and electrospinning,[11] have been reported for the preparation of polysaccharide-based materials with anisotropic microstructures.[12–13] In contrast to these methods, we originally developed a meniscus splitting method[14–19] for preparing a three-dimensionally ordered polymer membrane by developing viscous fingering phenomena.[20–23] Under the control of temperature and humidity, the evaporative interface of the polymer solution/dispersion from a cell induces the orientation of polymeric microfibers along the contact line of the interface by capillary force. During water evaporation, the concentrated polymer at the interface bridges the millimeter-scale gap between the two substrates and forms vertical membranes. The limitation for the bridging distance is basically ~2 mm, depending on the capillary length.[23] Notably, the dried membranes exhibit microstructures that are oriented parallel to the gap direction and layered microstructures in the thickness direction. These three-dimensionally ordered anisotropic architectures have been demonstrated in several types of polysaccharides, such as pectin, sacran, and xanthan.[14–19, 24–25]

In this chapter, we reconstructed a chitosan network with a three-dimensional order and designed a chitosan hydrogel that exhibited anisotropic swelling/deswelling with pH changes. The network was prepared in two steps: I) an acidic aqueous solution of chitosan was dried using the meniscus splitting method to obtain microscopically oriented and layered structures in a dried state, and II) the dried chitosan membrane was immersed in pH buffer solutions to control the intermolecular crosslinking points in the membrane. Considering that pH control is an important strategy in the field of biomedicine, sol-gel

transitions via pH changes in aqueous solutions should be clarified. To confirm the composition/decomposition of the crosslinking points, the pH dependence of the hydrogels was studied in three dimensions. Using the tendency that intermolecular hydrogen bonding among the hydroxy groups in the side chain works as crosslinking points,[26–28] the oriented structures of chitosan fibers in the dried membrane were maintained during in situ crosslinking. Based on the membrane preparation with orientation control, the microstructures reflected anisotropic swelling/deswelling as pH-sensitive hydrogels. To clarify the anisotropic nano- and microstructures in the dried membranes, we conducted microscopic observations using polarized optical microscopy, scanning electron microscopy (SEM), wide- and small-angle X-ray scattering (WAXS, and SAXS), and polarized attenuated total reflection infrared spectroscopy.

4.2. Materials and Methods

4.2.1. Materials

Chitosan, as poly(D-glucosamine) with a Mw of 50–190 kDa, was purchased from Merck KGaA, Darmstadt, Germany. The product was 75–85% deacetylated, and the viscosity of the aqueous solution was 200–800 cP (1 wt% in 1% acetic acid). This is the deacetylated chitin, poly(D-glucosamine), which is categorized as that with a low molecular weight. Acetic acid (99.7%, FUJIFILM Wako Pure Chemical Corporation, Osaka, Japan) was used as received. After the chitosan powder was dissolved in an aqueous solution containing acetic acid, a small amount of impurities and air bubbles were removed using centrifugation using a centrifuge (CF15RN, Eppendorf Himac Technologies Co., Ltd, Japan) and an angle rotor (Angle Rotor T15A36, Eppendorf Himac Technologies Co., Ltd, Japan), in a condition (21,800 × g, 25 ℃, 30 min). McIlvaine buffer solutions composed of citric acid (Merck KGaA, Darmstadt, Germany) and disodium phosphate (Kanto Chemical, Tokyo, Japan) were prepared using chemicals without purification.

4.2.2. Drying experiments

The aqueous solution at ~25 ℃ was poured into a topside open cell, which is a type of Hele-Shaw cell. The cells were placed in an oven at constant temperature under atmospheric pressure using the air circulator of a forced convection system (AS ONE, OFWP-600V). Considering that the volume of the oven (600 mm × 497 mm × 500 mm, ~150 L) with an air circulator was larger than the volume of the samples (< 1 mL), the RH in the oven was controlled by the set temperature.

4.2.3. Characterizations

Wide-angle X-ray scattering (WAXS) measurements were performed with a Nano-viewer (Rigaku Co., Tokyo, Japan) using a Cu–Ka radiation source. The wavelength of the X-ray beam used was 0.154 nm, and the scattered X-rays were detected by a 2D detector, PILATUS 1M (Detris A.G., Baden, Switzerland). Small-angle X-ray scattering (SAXS) measurements were conducted using an FR-E instrument equipped with a two-dimensional detector, R-axis IV (Rigaku), with an imaging plate (Fujifilm). An X-ray beam from Cu Kα radiation 0.154 nm, 0.3-mm collimated) was used, and the camera length was set to 300 mm. The samples were packed in glass capillary tubes (Hilgenberg) with a diameter of 1.0 mm and a thickness of 0.01 mm, and were subsequently measured in an open system, in a dry state. After measurement in the dry state, pure water was loaded into the capillaries, and 10 minutes later, the samples were measured in a wet state. IR spectra (in the mid-IR region from 800 to 4000 cm^{-1}) were obtained using the IR beamline BL43IR at the SPring-8 synchrotron facility (Hyogo, Japan). An FTIR microspectrometer (Bruker model Hyperion2000 IR microscope with Vertex 70 FTIR spectrometer) was used with IR synchrotron radiation. The wavenumber resolution was 3 cm^{-1}, and the accumulated number was 200. Attenuated total reflectance (ATR) spectra were obtained by attaching the ATR objective (20× and NA = 0.6 objective with Ge ATR crystal) onto the Hyperion2000 microscope. Polarized spectra were obtained using a BaF_2 substrate wire-grid polarizer.

4.2.4. Characterizations

To verify the macroscopic orientation, the samples were photographed using linear-crossed polarizers. To determine the orientation direction, a first-order retardation plate with λ = 530 nm was placed in the light path between a polarizer and the sample. Microscopic observations were performed using a microscope (BX53-P, Olympus) equipped with a CCD camera (DP74, Olympus). The swelling behavior of the hydrogels in terms of L_x, L_y, and L_z was monitored using a microscope, and the thickness (L_x) was checked using a micrometer to ensure the reliability of the measurements. To characterize the submicron-scale structures of the membranes, the samples were observed using field-emission SEM (S-5200, Hitachi). The samples were coated with Os using an ion sputterer (Neoc-Pro, Meiwafosis Co., Ltd., Japan).

4.3. Results and Discussion

4.3.1. Preparation of chitosan membrane with anisotropic structure

The meniscus splitting method enabled the aqueous chitosan solution to form a membrane (**Fig. 4.1**). Chitosan was initially dispersed in an aqueous mixture containing acetic acid and deposited by bridging the gaps and forming a membrane during drying. Acetic acid was used to disperse chitosan that was not

dispersed in pure water (chitosan: 2.5 wt%, acetic acid: 1 v/v%). The chitosan solution was poured into a Hele-Shaw cell with 1 mm gap. The gap size for the polymer bridging and the membrane formation is optimized, based on the principle of capillary action[23] and experimental demonstrations (**Fig. 4.2**). In the condition, the probability of the meniscus splitting for the membrane formation was high enough, > 90% and reproducible. The membrane having the orientation parallel to the Y-direction was confirmed in range of 0.5–2.0 mm. During this process, the solutions were heated at 40 ℃, where both water and acetic acid were evaporated (**Fig. 4.1A**). The heating temperature at 40 ℃ stably provides membrane formation with the layered structure (**Fig. 4.3**). The liquid phase showed pink color, the same color in the background and did not show blue or yellow color, suggesting that it is the isotropic state in this scale. Next, polarized light microscopic observation of the membrane revealed that the polarizers and first order retardation plate (λ = 530 nm) were directionally set, as shown **Fig. 4.1B**. Under polarized optical microscopy with crossed polarizers, the sample exhibited a blue interference color. The molecular director within the sample was aligned horizontally, at approximately 45 degrees to the polarizer and analyzer axes. Assuming positive birefringence, the slow optical axis lies along the director orientation (horizontal direction), while the fast axis is oriented vertically, perpendicular to it. The observed blue color results from optical retardation caused by birefringence, where the ordinary and extraordinary rays accumulate a phase difference as they pass through the anisotropic material. The retardation corresponds to constructive interference in the blue region of the visible spectrum, leading to the blue appearance under crossed polarizers. Unlike cast films on the bottom or sidewalls with no signals of orientation (**Fig. 4.4**), the membrane formed from two air–liquid phases, which is shown in blue. This result strongly suggests that the membrane has a structure that is oriented parallel to the Y-gap axis. This is because the polymer orients along the contact line in the Y-gap direction, where the capillary force works strongly, similar to other polysaccharides previously reported.[14, 17] The polarized microscopic image in the XZ-plane showed strong yellow collar, suggesting that the polymer aligns parallel to the Z-direction.

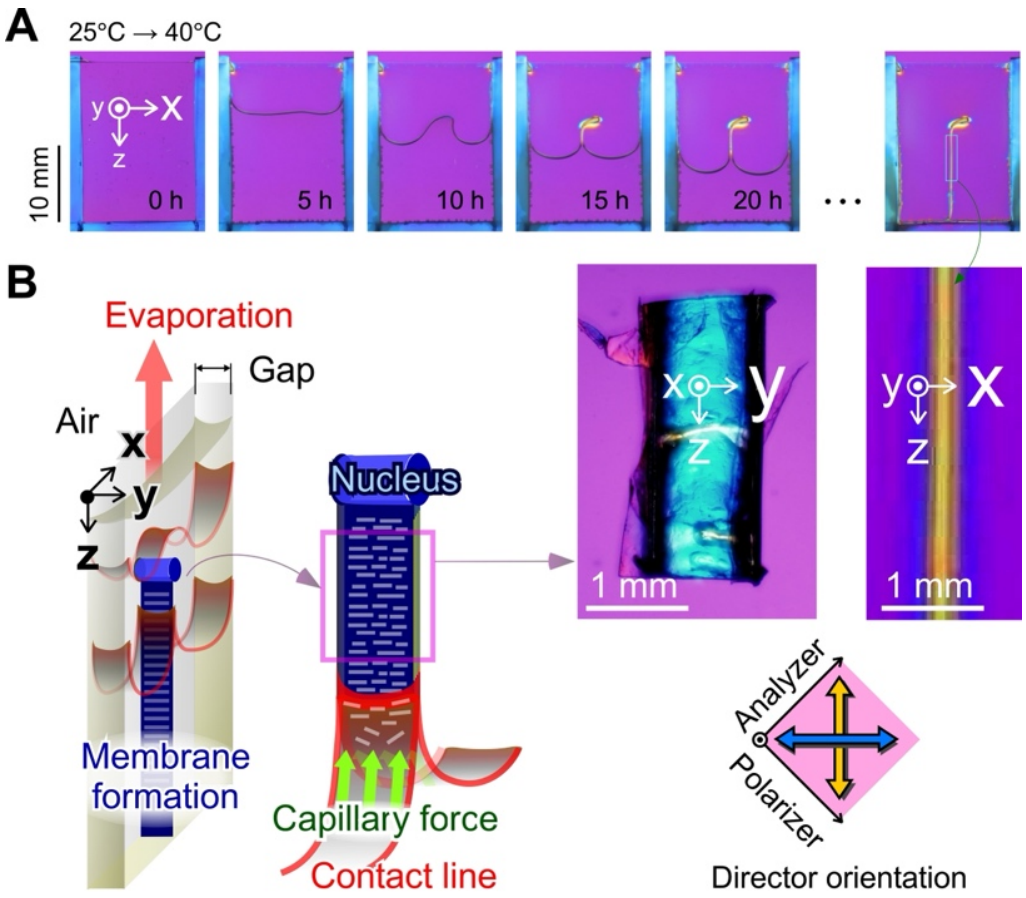

Figure 4.1. Preparation of chitosan membranes using the meniscus splitting method. A. Time course change of chitosan solution from a Hele-Shaw cell (15 mm-width, 1 mm-gap, ~20 mm-depth) observed through crossed Nicols with a retardation plate (λ = 530 nm). B. Polarized microscopic images show the dried membrane in YZ-plane and XZ-plane. Director orientation is common for all images.*

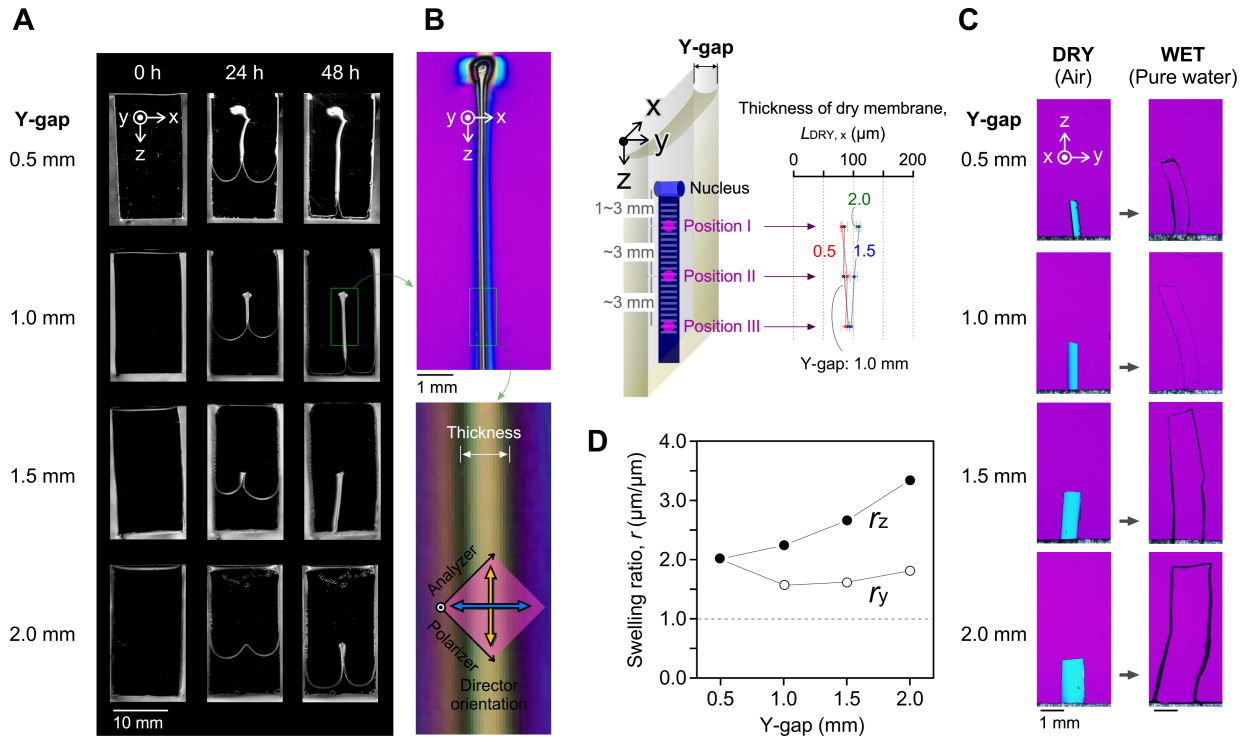

Figure 4.2. Chitosan membrane formation and polarized microscopic images by meniscus splitting method with controlling the cell gap. A. Membrane formation from a Hele-Shaw cell (12 mm, Y-gap, ~20 mm) with given gap distance (0.5, 1.0, 1.5, and 2.0 mm). Initial chitosan concentration: 2.5 wt%. Initial concentration of acetic acid: 1 v/v%. Drying temperature: 40˚C. **B.** Polarized optical microscopic images of membranes in XZ-plane and thickness of dried membrane, $L_{DRY, x}$ at given positions (I, II and III) in each gap-condition. **C.** Polarized optical microscopic images of membranes in YZ-plane under air and under pure water. All samples in B and C were observed through crossed Nicols with a retardation plate (530 nm) in the same direction as represented. **D.** Swelling ratio, $r = L_{WET}/L_{DRY}$ in pure water at ~25°C. Subscript in r means each direction (Y, and Z). For example, $r_y = L_{WET, y}/L_{DRY, y}$. L_y means the length of sample in the Y-direction. The axes are common for all panels.

The thickness of the dried membrane at given positions, less than 10 mm from the nucleus-top showed similar values in each gap-condition (**Fig. 4.2A-B**). By using the membranes from cell with 0.5, 1.0, and 1.5 mm-gap, the swelling ratio in pure water was measured. The value for 1.0 mm-gap was in range of ±20% similar with the values for 0.5 and 1.5 mm. It would be estimated that the membrane formed from a cell with 1.0 mm-gap would reproducibly show similar ratios (**Fig. 4.2C-D**).

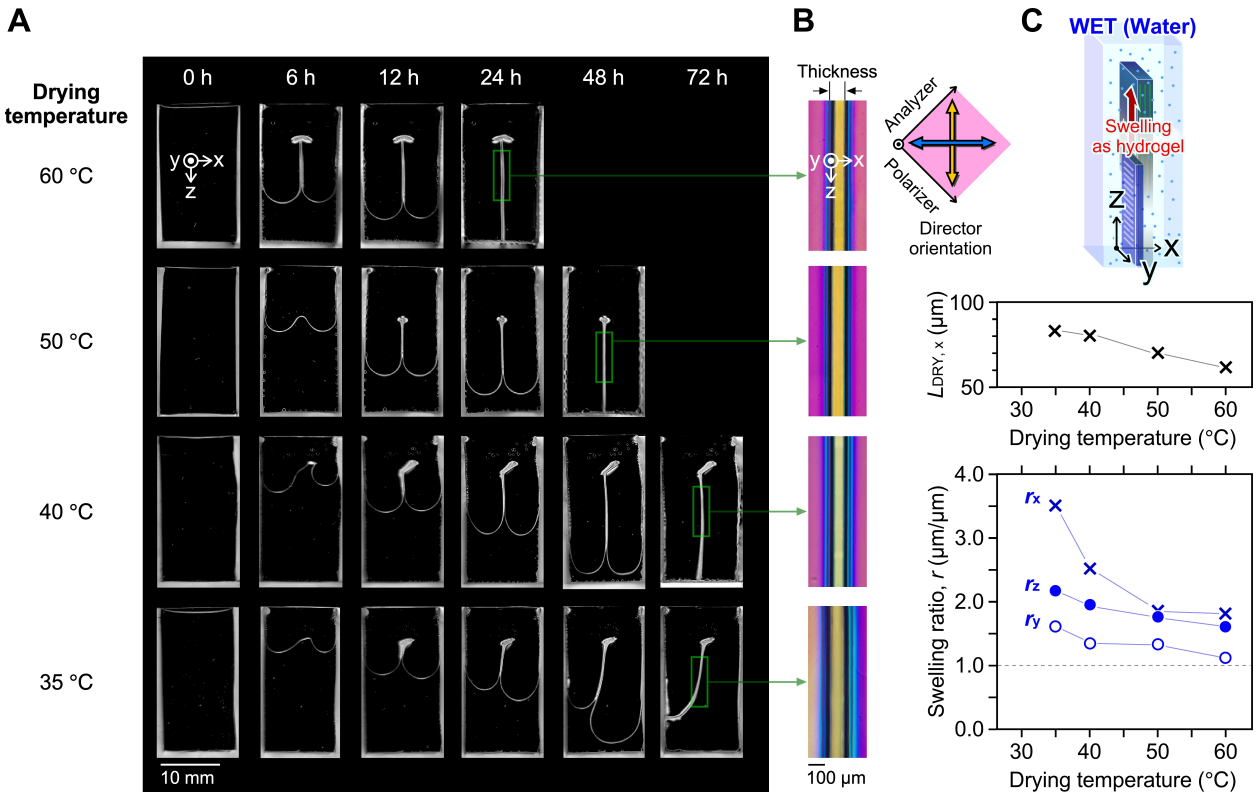

Figure 4.3. Effect of drying temperature on membrane formation through meniscus splitting. A. Photograph of deposited vertical membrane by drying chitosan solution. Initial concentration of chitosan: 2.5 wt%. Initial concentration of acetic acid: 1 v/v%. Drying from a Hele-Shaw cell (12 mm-width, 1 mm-gap, ~20 mm-depth). Drying temperature: 35, 40, 50, and 60 ˚C. **B.** Polarized optical microscopic images of membranes under air in XZ-plane through crossed Nicols with a retardation plate (λ = 530 nm). **C.** Thickness of dried membrane, $L_{DRY, x}$ at given positions and swelling ratio in pure water in each direction as a function of drying temperature.

By checking the effect of the drying temperature on the membrane formation through meniscus splitting, the layered structure was qualitatively confirmed (**Fig. 4.3A**). In the drying temperature range of 35—60 ℃, the polymeric orientation could be suggested by the polarized microscopic observation (**Fig. 4.3B**). To verify the layered structures for absorbing water, the membrane's thickness ($L_{DRY, x}$) and the swelling ration in each direction were measured (**Fig. 4.3C**). As an increase of the drying temperature from 35 ℃ to 60 ℃, the $L_{DRY, x}$ decreased to ~70%. This trend is also sawn in the swelling ratios, especially, r_x. It is suggested that the number of layer parallel to the XZ-plane increases.

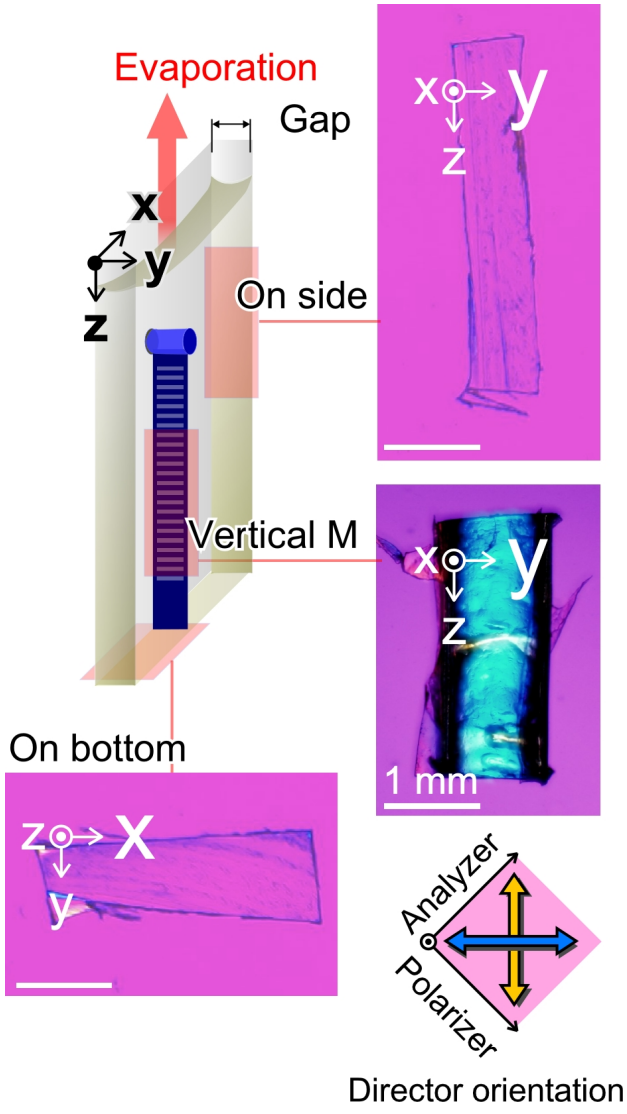

Figure 4.4. Polarized microscopic image of the chitosan casted film through crossed Nicols with a retardation plate (λ = 530 nm). The sample was prepared by drying a 2.5 wt% chitosan solution at 40 ℃ from a cell with a 1-mm gap.

4.3.2. Nano- and molecular structures in the chitosan dry membrane

To clarify the nano- and molecular structures of the chitosan membrane, samples were analyzed using WAXS, and SAXS. **Fig. 4.5A** shows a schematic illustration of the membrane as a dried sample and its chemical structure with hydrogen bonds as the intermolecular interaction. The membrane has a hierarchical architecture: nanofibers and microfibers as the molecular and nanofiber bundles, respectively, as in previous reports.[29–31] As shown in **Fig. 4.5B**, the WAXS profile indicates that characteristic periodicities exist at the nanometer scale. The profile was calibrated, centered, and integrated along the meridional and equatorial

directions. The equatorial peaks indicate the distances along the intersheet and interchain directions. The arrow in the 2D WAXS profile was analyzed as the 1D WAXS profile, showing the orientation functions (001), (100), and (101) in the meridian but not in the equator. This result strongly indicates that the fibrillar crystals were detected in the meridian direction. In addition, this signal was a marker of the distance between the two hydroxyl groups along the central axis of the chitosan helix. **Fig. 4.5C** shows SAXS profiles of chitosan membrane measured in air. The chitosan membrane exhibited a large peak at $2\theta \sim 2.2°$ and two smaller intense peaks at $2\theta = 4–6°$, which correspond to the periodicity of 3.87 and 1.94–1.24 nm in equatorial direction, respectively. These periodicities would be originated from the diameter of chitosan nanofibers. Besides, these suggest the presence of anisotropic lamellar stacking structure oriented parallel to Z-direction. In contrast, the peaks observed in air disappeared in the pure water environment (**Fig. 4.6**). This could be due to plenty of water molecules penetrating the periodic structures, thereby resulting in anisotropic swelling.

To clarify the anisotropy of molecular structures, the dried sample was evaluated using infrared (IR) spectroscopy through polarized light at 50% relative humidity (RH) (**Fig. 4.5D**). The two significant peaks at approximately 3361 and 3288 cm^{-1} were attributed to the O–H and N–H stretching vibrations, respectively, of the functional groups, which are involved in hydrogen bonding between chitosan molecules. The peaks at 2880 and 2924 cm^{-1} indicated alkane C–H stretching. The characteristic peaks at 1564, 1409, and 1100 cm^{-1} are attributed to the N–H bending vibration of amine II, alcoholic C–O stretching, and alkane C–H bending, respectively. All bands, except those at 3288, 3361, and 2880–2924 cm^{-1}, in the direction parallel to the Y-axis were stronger than those in the direction parallel to the Z-axis. These results can be attributed to the fact that the chitosan nanofibers in the bundled state exposed more side chains parallel to the Y-axis.

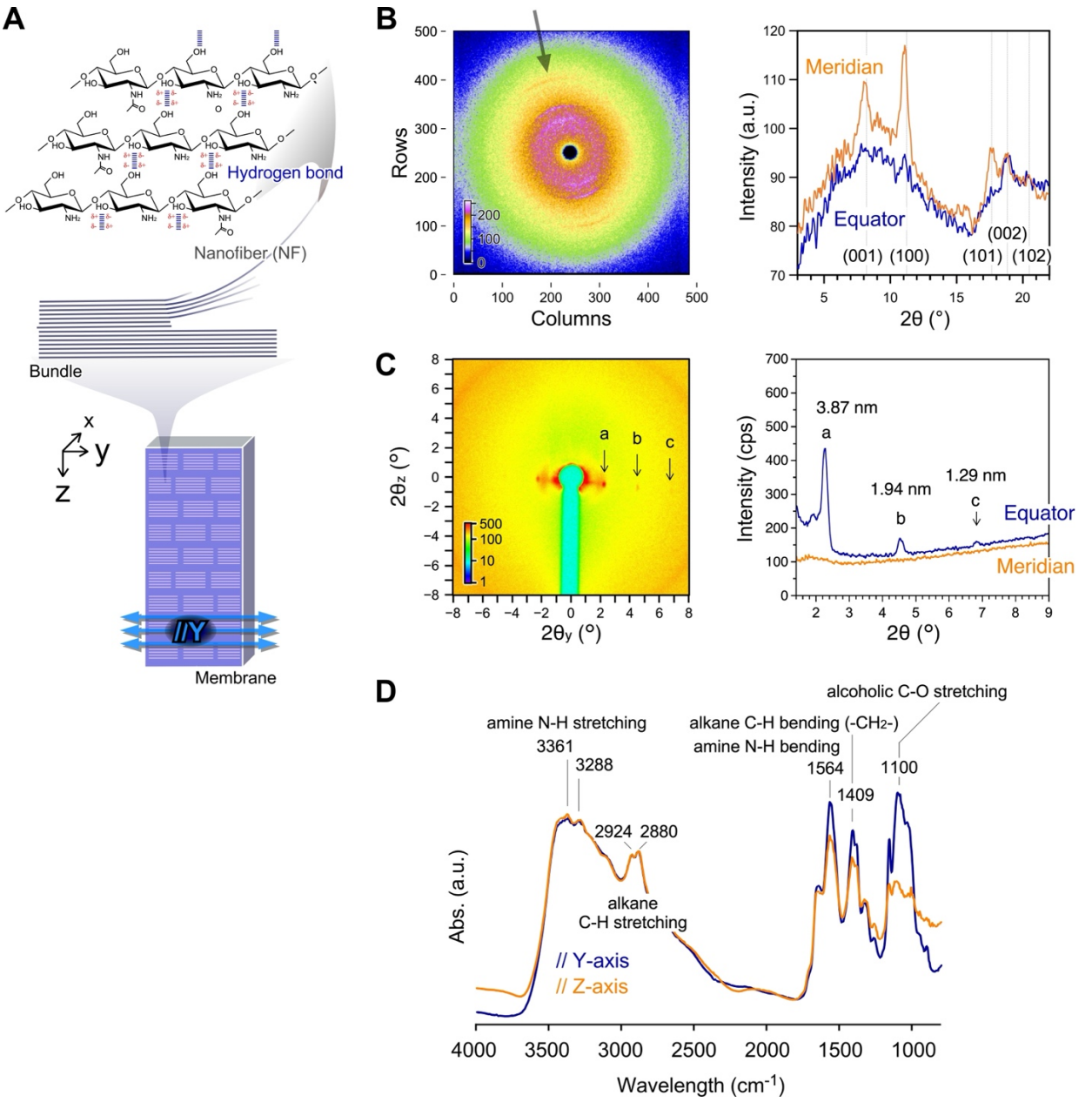

Figure 4.5. Nano- and molecular structures in the chitosan dry membrane prepared using the meniscus splitting method. A. Schematic illustration of the chitosan membrane prepared using the meniscus splitting method and its chemical structure. Y-axis is the gap direction, and Z-axis is the depth direction in the cell. The XYZ-axis is common with the preparation using meniscus splitting from Hele-Shaw cells. **B.** WAXS profiles of the membrane under an air environment. The arrow indicates the position of strong intensity. **C.** SAXS profiles of dry membrane under air environment. The arrow indicates the position of strong intensity. Room temperature: ~25 ℃. Relative humidity: ~50%. **D.** IR spectra of the membrane through polarized light. Spectra in blue and yellow are detected when the polarizer is parallel to the cell gap (Y-direction) and cell depth directions (Z-direction), respectively. Room temperature: ~25 ℃. Relative humidity: ~50%.*

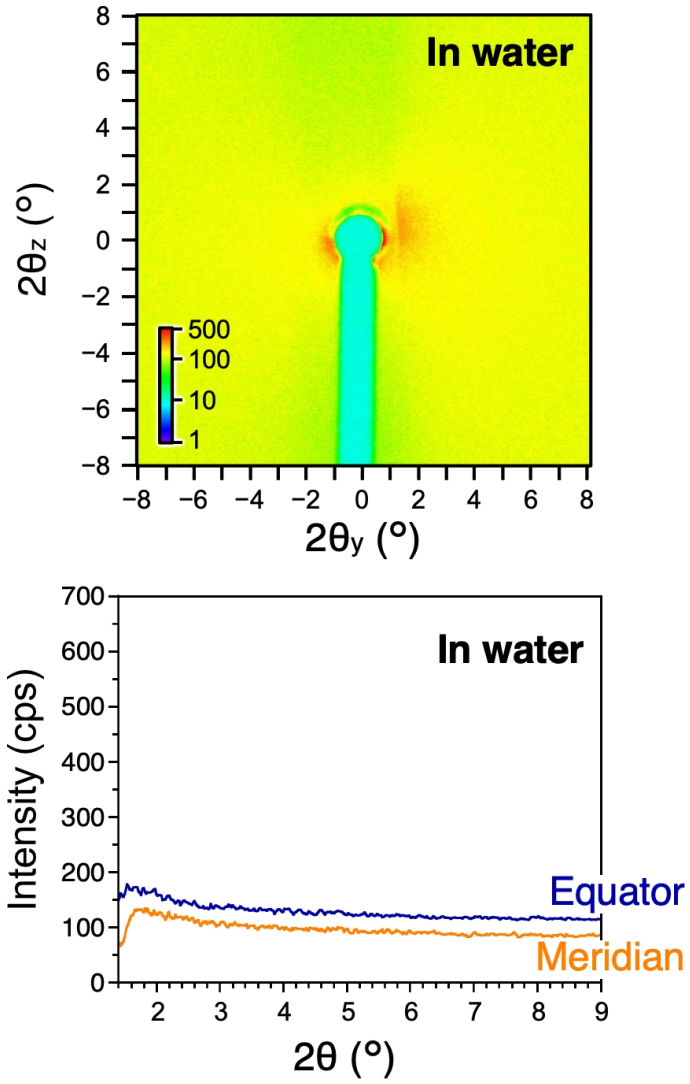

Figure 4.6. SAXS profiles of chitosan membrane under water environment. Room temperature: ~25 °C.*

4.3.3. Preparation of chitosan anisotropically hydrogel and its microstructures

Considering that chitosan cannot disperse in pure water but can disperse in an acetic acid aqueous solution, the dried chitosan membrane with an oriented structure should have the potential to show ordered swelling. The thickness of the dried membrane was in range of 90–110 μm. The uniformity of the thickness could be confirmed in parts of 10 mm height in the middle (**Fig. 4.2**). By rewetting the membrane with pure water, and without any additional crosslinker from air, the membrane behaved as a hydrogel with anisotropic swelling (**Fig. 4.7A**). The swelling ratios, L_{WET}/L_{DRY} in X-, Y- and Z-direction were 3.1, 1.3, and 1.8, respectively. During drying of the chitosan solution, chemical crosslinkers or crosslinking points were not purposely introduced. Notably, the membrane rapidly and anisotropically swelled in pure water

while maintaining its hydrogel shape. This behavior suggests that the oriented structure in the Y-gap direction affected the swelling direction. Certain hydroxyl groups on the chitosan side chains can function as crosslinking points for hydrogen bonds to behave as a hydrogel. During anisotropic swelling from the dry state in air to the wet state in pure water, the intensity of the blue color decreased, but the sample retained its size in the Y-direction. These results clearly indicate that numerous water molecules can anisotropically interpenetrate in the striped structures along the Y-direction but not along the Z-direction. As a result, the membrane remarkably swelled in the Z-direction.

To study the microstructures in the DRY/WET states, the samples were observed using SEM (**Fig. 4.7B**). A WET (water) sample was prepared by freeze drying. In contrast to the DRY sample, the WET sample had striped patterns with microgrooves parallel to the Y-axis. This tendency was also confirmed with analytical data from the FFT (**Fig. 4.7B**, inset). Microgrooves were generated during the sample preparation under reduced pressure, enabling mechanical stress. By analyzing the gray values of the green line on the images, the interval size between the microgrooves (Δz) were measured. The average value of Δz was 2.1 μm, and the groove width was < 0.3 μm. The striped shape with values clearly signifies that the periodic microstructures in the Z-direction were maintained in the membrane. Such submicron-scale periodicity was also confirmed in the cross section of the DRY membrane as layers of the YZ plane stacked in the X-direction (**Fig. 4.7C** and **Fig. 4.8**). Considering that the layer-to-layer distance varied 0.3–0.5 μm, the chitosan fibers were easily self-assembled at this submicron-scale, as well as the chitin.[31] Conversely, the twisted plywood structures typically observed in chitin were not clearly observed, and the chitosan membrane may contain twisted structures. This consideration is based on the fact that the membrane has two strong two-oriented structures parallel to the Y- and Z-axes.

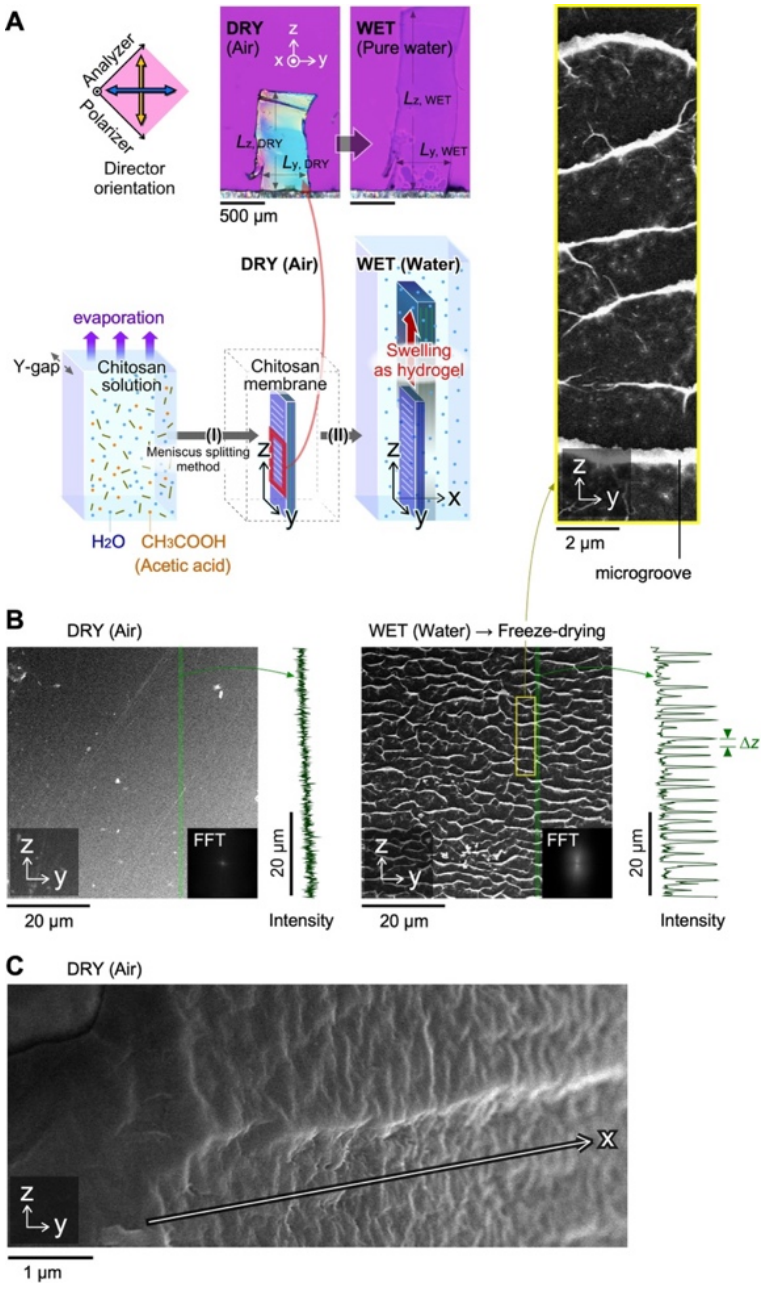

Figure 4.7. Chitosan hydrogel anisotropically swelling in pure water and its microstructures. A. Polarized optical microscopic images in air and in pure water. The process of the chitosan solution for the preparation of the DRY membrane and WET hydrogel. (I) Drying the aqueous chitosan solution includes acetic acid to form chitosan membrane using meniscus splitting. (II) Addition of pure water to the membrane. **B.** SEM images of the heat-dried sample prepared using the meniscus splitting method as DRY (air) and freeze-dried sample as WET (water). Inset: Fast Fourier Transformation (FFT) analytical data of SEM images. Charts indicate surface asperity on the YZ-plane of samples by analyzing the intensity of the gray value along the green line in the SEM images. Zoomed-in image in yellow-outlined area shows typical periodicity. **C.** SEM images of the heat-dried sample, focusing on the cross-section in the X-direction.

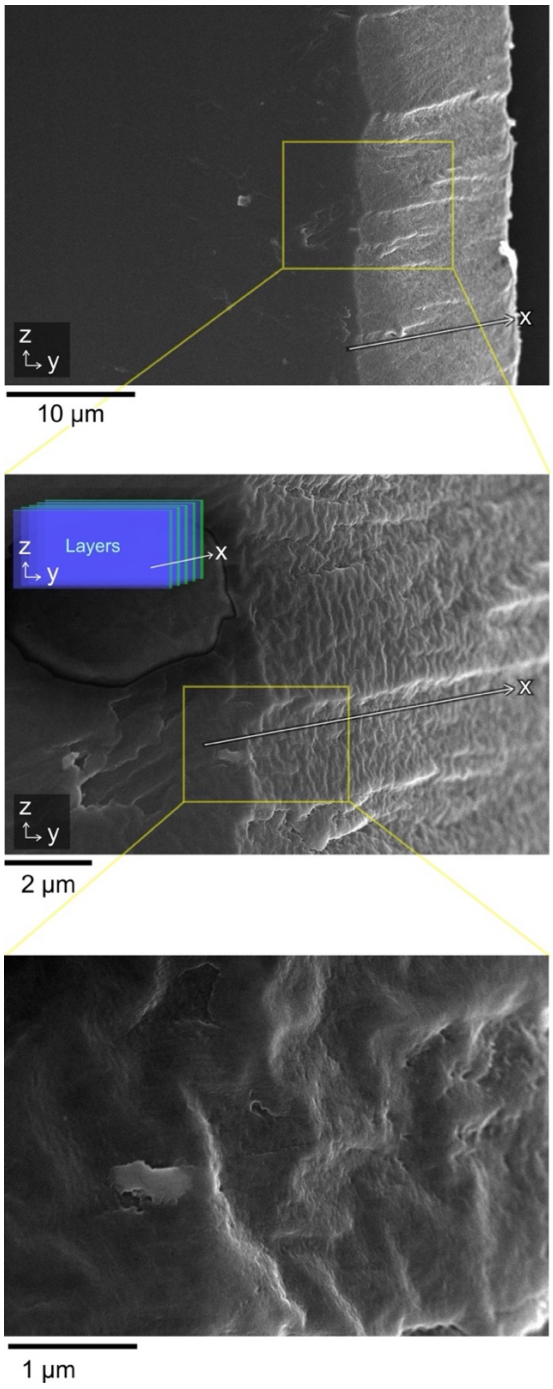

Figure 4.8. SEM images for the heat-dried sample prepared using the meniscus splitting method.

4.3.4. Chitosan hydrogel with an anisotropic pH response

To three-dimensionally understand anisotropic swelling, the dried membrane was directly immersed into each buffered solution with a wide pH range (2.2–8.0) at ~25 ℃. **Fig. 4.9A** shows typical images at a given pH and the pH dependence of the equilibrium swelling ratio. The ratio, *r*, is defined as the ratio of the length in the wet state to that in the dry state, L_{WET}/L_{DRY}. Swelling ratios in each direction are defined as $r_x = L_{WET,\,x}/L_{DRY,\,x}$, for example. In this pH range, r_x was significantly higher than r_y and r_z. For example, the r_x at pH 5.0 was 2.1 ($L_{WET,\,x}$ = 72 μm, $L_{DRY,\,x}$ = 34 μm). This remarkable r_x increase might be due to the greater change in the intervals between the layers, as confirmed by the SEM images (**Fig. 4.8**). All the swelling ratios (r_x, r_y, and r_z) in acidic conditions with pH 2.2–4.0 showed higher values, and the polarized microscopic images showed no signals for orientation in the Y-direction. Under acidic conditions, protonation enables water molecules to penetrate the interspaces among the fibers and chains in the fibers. Consequently, certain crosslinking points, owing to hydrogen bonds, can be decomposed. Considering that the p*K*a of chitosan is approximately 6.4, the protonation/deprotonation equilibrium condition affects the swelling ratio in the pH range of 5.0–7.0.

The repeatability of swelling/deswelling as a hydrogel was confirmed for the use of the membrane under a physiological pH condition, such as the pH of 7.4 in blood. In the cyclic pH changes between 8.0 and 2.2, the gels showed no reversibility. After swelling from pH 8.0 to 2.2, the gel once again immersed at a pH of 8.0 did not deswell to its original ratio and maintained a similar ratio to that at pH 2.2 (**Fig. 4.9B**). Following the repeated tests of pH-changes between pH 8.0 and 2.2, certain crosslinking points irreversibly decomposed at a pH of 2.2, and the sample continued swelling close to the equilibrium state of pH 8. This irreversible tendency was also confirmed in the pH cyclic changes between 5.0 and 2.2. Under acidic conditions, such as a pH of 2.2, protonation of the chitosan chain strongly induced the decomposition of hydrogen bonds between the hydroxy groups and an exchange of citric acid. Notably, in the cyclic pH changes between pH 8.0 and 5.0, the chitosan gels exhibited reversibility both in the Y- and Z-directions (**Fig. 4.9C, Table 4.1 and Fig. 4.10**). In contrast to the r_y changes (1.0 and 1.1), the r_z changes were approximately 1.2 and 1.3. The small increases of the r_z as the pH change from 5 to 8 would be because that the decrease of citric acid concentration and the increase of the Na_2HPO_4 in the buffer. The increase of PO_4^{3-} concentration would intervene the intermolecular complex between the hydroxy groups in the pH 8.0 condition. These results suggest that water molecules can penetrate in and out of the intervals of the oriented main chitosan chains but some of the hydrogen bonds remain without dissociation. This reversibility of the anisotropic swelling is due to the rigid chains parallel to the Y-direction.

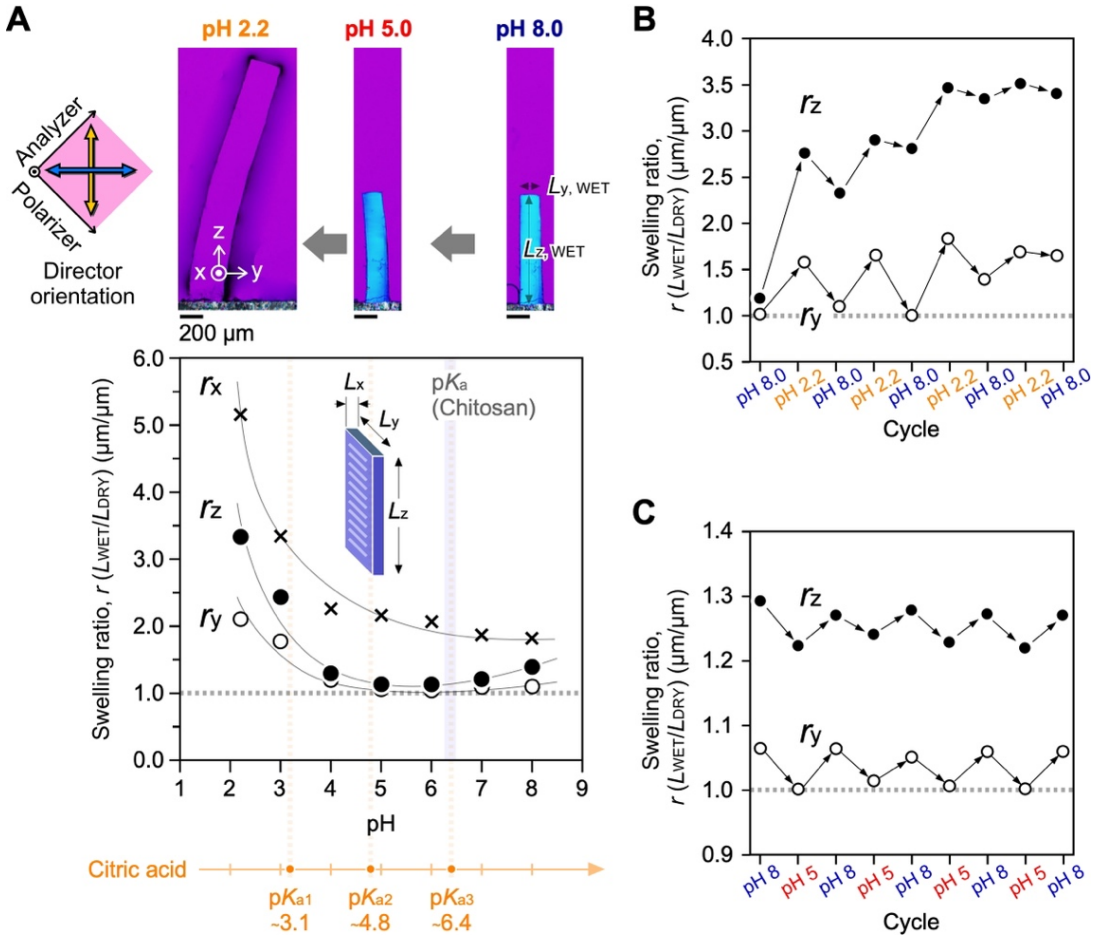

Figure 4.9. Chitosan hydrogel with an anisotropic pH response. **A.** pH-dependence of the swelling ratio in three dimensions. L_x, L_y, and L_z represent the sample length in each direction. Swelling ratio in each direction, r indicates the L_{WET}/L_{DRY}. For example, $r_x = L_{WET,\,x}/L_{DRY,\,x}$. DRY signifies a condition under air atmosphere at approximately 25 °C. The DRY samples were equilibrated in initial pH buffer solutions as the WET state. **B.** Repeat tests of pH changes between pH 8.0 and 2.2. **C.** Repeat tests of pH changes between pH 8.0 and 5.0. Buffer solutions comprised citric acid and disodium phosphate.

Table 4.1. Composition of pH buffer solution.

pH (21°C)	**Citric acid 0.1 M**	**Na_2HPO_4 0.2 M**
2.2	19.60 mL	0.40 mL
3.0	16.22 mL	3.78 mL
4.0	12.38 mL	7.62 mL
5.0	9.80 mL	10.20 mL
6.0	7.50 mL	12.50 mL
7.0	3.56 mL	16.44 mL
8.0	0.56 mL	19.44 mL

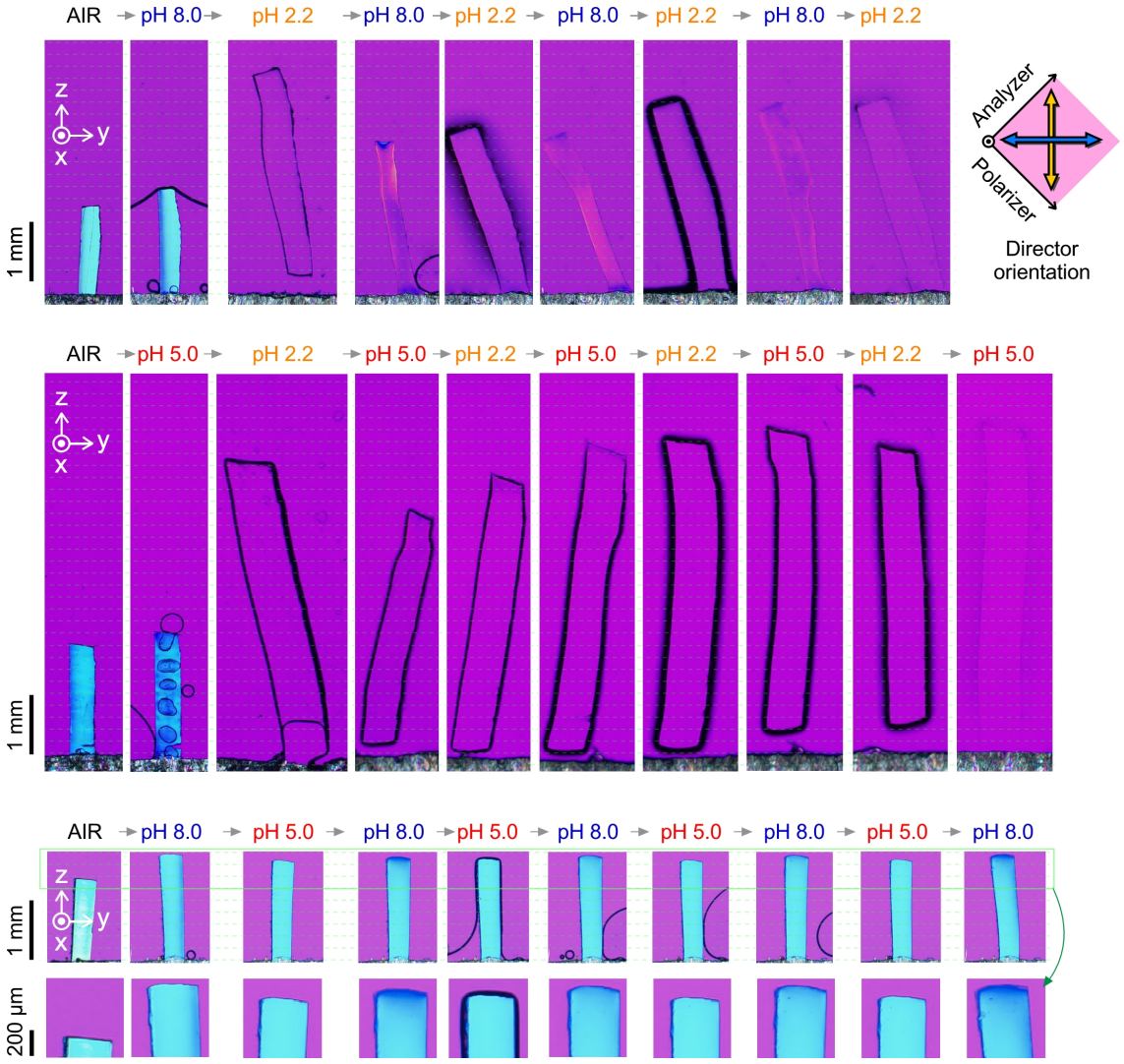

Figure 4.10. Polarized optical microscopic images of chitosan hydrogels during cyclic pH changes (pH 8 ⇄ pH 2.2, pH 5 ⇄ pH 2.2, and pH 8 ⇄ pH 5). Images were taken through crossed Nicols with a retardation plate (λ = 530 nm) in air and in aqueous buffer solutions at the given pH.

4.3.5. The chitosan membrane functioning as a pH-responsive hydrogel with anisotropy

Fig. 4.11 summarizes the structures of the chitosan membranes at multiple scales prepared using the meniscus splitting method and the anisotropic swelling/deswelling behaviors of the hydrogel in buffered solutions. Considering that the membrane was prepared by drying an aqueous chitosan solution containing concentrated acetic acid, the chitosan chains or crystalline structures could accumulate from the dispersed state to the oriented state on the evaporative interface. This orientation process, driven by capillary force,

is similar to that of other polysaccharides with self-assembled microfibers.[14–19] Dried chitosan membranes have an oriented structure with molecular, nano-, and submicron structures. Hierarchical architecture is the basic skeleton for the in situ crosslinking and anisotropic swelling of hydrogels. Regarding the reversibility of swelling/deswelling, the crosslinking points in the chitosan membranes were primarily affected by the concentration of citric acid in the buffer solutions. The acid dissociation constant (p*K*a) for chitosan is approximately 6.4, and those for citric acid with three carboxylic acid groups are approximately 3.1, 4.8, and 6.4. The pH condition also affects the increase in the protonated amino groups that induce the increase of the osmotic pressure in the network. Based on the correlation between the protonated or deprotonated states of chitosan and citric acid, the swelling ratios were affected by the formation of electrostatic attraction between the protonated amino groups of chitosan and the deprotonated carboxyl groups of citric acid. Thus, it exhibited an irreversibly swollen state because most of the hydrogen bonds among the chitosan chains were exchanged with acids.

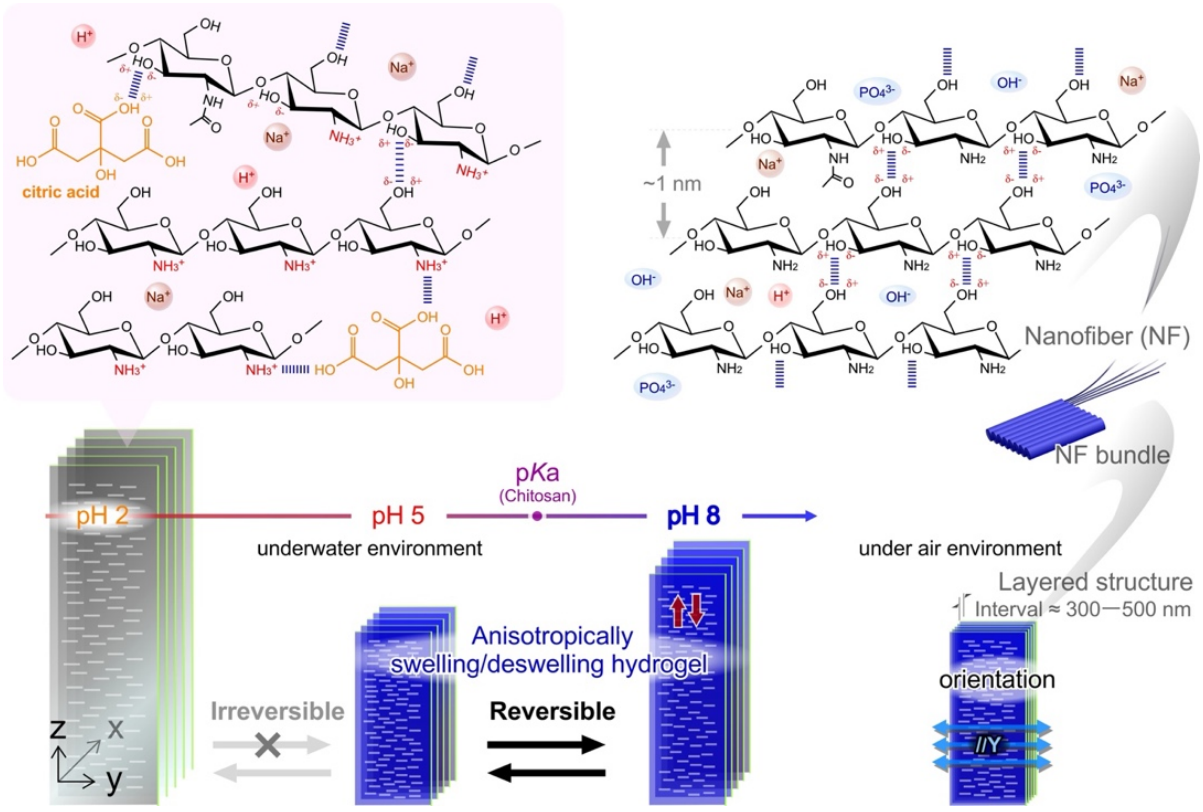

Figure 4.11. Schematic illustration of the chitosan membrane functioning as a pH-responsive hydrogel with anisotropy. Chitosan hydrogel prepared using meniscus splitting shows reversible swelling and deswelling between pH 5 and 8. It shows an irreversible swollen state following the repetition of exchanging outer buffer solution between pH 2.2 and 8. pH was controlled by citric acid and disodium phosphate concentrations.

4.4. Conclusion

A chitosan membrane with a three-dimensionally ordered structure was successfully prepared using the meniscus splitting method. This membrane was capable of functioning as a hydrogel with an anisotropic pH response over a wide pH range of 2.2–8.0. This reconstruction of anisotropy from the aqueous solution was confirmed using polarized optical microscopy and SEM, indicating a macroscopic orientation in the membrane. This anisotropic structure directly affected the anisotropic swelling of the hydrogel in aqueous environments. Through in situ intermolecular crosslinking via hydrogen bonding among the hydroxyl groups on the side chain, the swelling ratio was three-dimensionally controlled under acidic to alkaline conditions. The ratio was strongly affected by the acidic conditions. One is the increase in the osmotic pressure as an increase in the protonated amino groups arranged along the direction parallel to the gap direction (//Y). The other is caused by intermolecular crosslinking with intermediate citric acids. Based on the pH-responsive swelling ratio, this material can be applied in an aqueous environment with a pH signal, irreversible in the pH range of 2–5 and reversible in the pH range of 5–8. The decrease in pH from normal cells to cancer cells can be a switching signal not only for mass transporters, such as nanogels and micelles, but also for tissue engineering using stimuli-responsive soft materials. The anisotropic pH response of the chitosan networks under physiological conditions would be useful in wound dressing materials or materials for skin cell renewal.

References

[1] Lu, X.; Jiao, H.; Shi, Y.; Li, Y.; Zhang, H.; Fu, Y.; Guo, J.; Wang, Q.; Liu, X.; Zhou, M.; Ullah, W. M.; Sun, J.; Liu, J. Fabrication of bio-inspired anisotropic structures from biopolymers for biomedical applications: A review. *Carbohydr. Polym.* **2023**, *308*, 120669.

[2] Pelláa, G. C. M.; Lima-Tenóriob, K. M.; Tenório-Netob, T. E.; Guilhermea, R. M.; Muniza, C. E.; Rubira, F. A. Chitosan-based hydrogels: From preparation to biomedical applications. *Carbohydr. Polym*. **2018**, *196*, 233–245.

[3] Shi, Q.; Liu, H.; Tang, D.; Li, Y.; Li, X.; Xu, F. Bioactuators based on stimulus-responsive hydrogels and their emerging biomedical applications. *NPG Asia Materials* **2019**, *11*, 64.

[4] Cheng, G.; Dai, J.; Dai, J.; Wang, H.; Chen, S.; Liu, Y.; Liu, X.; Li, X.; Zhou, X.; Deng, H.; Li, Z. Extracellular matrix imitation utilizing nanofibers-embedded biomimetic scaffolds for facilitating cartilage regeneration. *Chem. Eng. J*. **2021**, *410*, 128379.

[5] de Sousa, V. R.; da Cunha, S. M. A.; de Sousa, V. B.; de Araújo, N. G.; Lisiane Navarro de Lima, S. N. L.; Menezes, R. R. A Review on Chitosan's Uses as Biomaterial: Tissue Engineering, Drug Delivery Systems and Cancer Treatment. *Materials* **2020**, *13*, 4995.

[6] Vinay Kumar, V.; Sharma, N.; Janghu, P.; Pasrija, R.; Umesh, M.; Chakraborty, P.; Sarojini, S.; Thomas, J. Synthesis and characterization of chitosan nanofibers for wound healing and drug delivery application. *JDDST* **2023**, *87*, 104858.ư

[7] Heras-Mozos, R.; Gavara, R.; Hernández-Muñoz, P. Chitosan films as pH-responsive sustained release systems of naturally occurring antifungal volatile compounds. *Carbohydr. Polym*. **2022**, *283*, 119137.

[8] Fu, J.; Yanga, F.; Guo, Z. The chitosan hydrogels: from structure to function. *New J. Chem*. **2018**, *42*, 17162-17180.

[9] Ye, D.; Lei, X.; Li, T.; Cheng, Q.; Chang, C.; Hu, L.; Zhang, L. Ultrahigh Tough, Super Clear, and Highly Anisotropic Nanofiber-Structured Regenerated Cellulose Films. *ACS Nano* **2019**, *13*, 4843−4853.

[10] Chen, Y.; Zhou, L.; Chen, L.; Duan, G.; Mei, C.; Huang, C.; Han, J.; Jiang, S. Anisotropic nanocellulose aerogels with ordered structures fabricated by directional freeze-drying for fast liquid transport. *Cellulose* **2019**, *26*, 6653–6667.

[11] Cheng, G.; Yin, C.; Tu, H.; Jiang, S.; Wang, Q.; Zhou, X.; Xing, X.; Xie, C.; Shi, X.; Du, Y.; Deng, H.; Li, Z. Controlled Co-delivery of Growth Factors through Layer-by-Layer Assembly of Core−Shell Nanofibers for Improving Bone Regeneration. *ACS Nano* **2019**, *13*, 6372−6382.

[12] Wang, N.; Wang, X. X.; Yan, K.; Song, W.; Fan, Z.; Yu, M.; Long, Y. Z. Anisotropic Triboelectric Nanogenerator Based on Ordered Electrospinning. *ACS Appl. Mater. Interfaces*, **2020**, *12*, 46205−46211.

[13] Hecht, M.; Soberats, B.; Zhu, J.; Stepanenko, V.; Agarwal, S.; Greiner, A.; Würthner. F. Anisotropic microfibres of a liquid-crystalline diketopyrrolopyrrole by self-assembly-assisted electrospinning. *Nanoscale Horiz*. **2019**, *4*, 169-174.

[14] Okeyoshi, K.; Okajima, M. K.; Kaneko, T. Emergence of Polysaccharide Membrane Walls Through Macro-space Partitioning Via Interfacial Instability. *Sci. Rep*. **2017**, *7*, 5615.

[15] Okeyoshi, K.; Joshi, G.; Okajima, M. K.; Kaneko, T. Formation of Polysaccharide Membranes by Splitting of Evaporative Air-LC Interface. *Adv. Mater. Inter*. **2018**, *5*, 1701219.

[16] Okeyoshi, K.; Shinhama, T.; Budpud, K.; Joshi, G.; Okajima, M. K.; Kaneko, T. Micelle-mediated Self-assembly of Microfibers Bridging Millimeter-scale Gap to Form Three-dimensional-ordered Polysaccharide Membranes. *Langmuir* **2018**, *34*, 13965−13970.

[17] Okeyoshi, K.; Yamashita, M.; Sakaguchi, T.; Budpud, K.; Joshi, G.; Kaneko, T. Effect of Evaporation Rate on Meniscus Splitting with Formation of Vertical Polysaccharide Membranes. *Adv. Mater. Inter*. **2019**, *6*, 1900855.

[18] Joshi, G.; Okeyoshi, K.; Mitsumata, T.; Kaneko, T. Micro-deposition Control of Polysaccharides on Evaporative Air-LC Interface to Design Quickly Swelling Hydrogels. *J. Colloid Interf. Sci*. **2019**, *546*, 184−191.

[19] Okeyoshi, K.; Yamashita, M.; Budpud, K.; Joshi, G.; Kaneko, T. Convective meniscus splitting of polysaccharide microparticles on various surfaces. *Sci. Rep*. **2021**, *11*, 767.

[20] Brzoska, J. B.; Brochard-Wyart, F.; Rondelez, F. Exponential Growth of Fingering Instabilities of Spreading Films Under Horizontal Thermal Gradients. *Europhys. Lett*. **1992**, *19*, 97−102.

[21] Lajeunesse, E.; Martin, J.; Rakotomalala, N.; Salin, D. 3D Instability of Miscible Displacements in a Hele-Shaw Cell. *Phys. Rev. Lett*. **1997**, *79*, 5254−5257.

[22] Kataoka, E. D.; M. Troian, M. S. Patterning liquid flow on the microscopic scale. *Nature* **1999**, *402*, 794–797.

[23] de Gennes, P. G.; Brochard-Wyart, F.; Quéré, D. Capillarity and Wetting Phenomena: Drops, Bubbles, Pearls, Waves; *Springer*, 2003.

[24] Wu, L.; Saito, I.; Hongo, K.; Okeyoshi, K. Recognition of Spatial Finiteness in Meniscus Splitting Based on Evaporative Interface Fluctuations. *Adv. Mater. Inter*. **2023**, *10*, 2300510.

[25] Saito, I.; Wu, L.; Hara, M.; Ikemoto, Y.; Kaneko, T.; Okeyoshi, K. Anisotropic Responses with Cation Selectivity in Hierarchically Ordered Polysaccharide Networks. *ACS Appl. Polym. Mater*. **2022**, *4*, 7054−7060.

[26] Lin, F.; Wang, Z.; Chen, J.; Lu, B.; Tang, L.; Chen, X.; Lin, C.; Huang, B.; Zeng, H.; Chen, Y. A bioinspired hydrogen bond crosslink strategy toward toughening ultrastrong and multifunctional nanocomposite hydrogels. *J. Mater. Chem. B* **2020**, *8*, 4002-4015.

[27] Jiang, S.; Qiao, C.; Liu, R.; Liu, Q.; Xu, J.; Yao, J. Structure and properties of citric acid cross-linked chitosan/poly(vinyl alcohol) composite films for food packaging applications. *Carbohydr. Polym*. **2023**, *312*, 120842.

[28] Zhuang, L.; Zhi, X.; Du, B.; Yuan, S. Preparation of Elastic and Antibacterial Chitosan-Citric Membranes with High Oxygen Barrier Ability by in Situ Cross-Linking. *ACS Omega* **2020**, *5*, 1086−1097.

[29] Lizundia, E.; Nguyen, -D. T.; Winnickc, J. R.; MacLachlan, J. M. Biomimetic photonic materials derived from chitin and chitosan. *J. Mater. Chem. C* **2021**, *9*, 796-817.

[30] Dang, T. T. N.; Chau, T. L. T.; Duong, V. H.; Le, T. H.; Thi Thi Van Tran, T. T. V.; Le, Q. T.; Vu, P. T.; Nguyen, D. C.; Nguyen, V. L.; Nguyen, -D. T. Water-soluble chitosan-derived sustainable materials: towards filaments, aerogels, microspheres, and plastics. *Soft Matter* **2017**, *13*, 7292-7299.

[31] Fabritius, -O. H.; Sachs, C.; Triguero, R. P.; Raabe, D. Influence of Structural Principles on the Mechanics of a Biological Fiber-Based Composite Material with Hierarchical Organization: The Exoskeleton of the Lobster Homarus americanus. *Adv. Mater*. **2009**, *21*, 391–400.

*Data were partially taken by Matsuba Go, Hara Mitsuo, Ikemoto Yuka, Ito Nobuaki, and Kobayashi Shoko.

Chapter 5

General Conclusion

The evaporation behavior of pure water and polymer solution was analyzed at 40 °C and 60 °C. Theoretical and experimental results for pure water demonstrated consistent evaporation curves, with evaporation times of approximately 1500 minutes at 40 °C and 400 minutes at 60 °C. In contrast, polymer solution at 40 °C exhibited deviations between theoretical and experimental curves due to positional changes within the cell, indicating structural transformations during solvent evaporation.

A deeper analysis of meniscus splitting with multiple nucleations revealed the effects of symmetry misalignment and asynchrony in an aqueous chitosan dispersion. The study controlled initial polymer concentration and Hele-Shaw cell width to observe these phenomena. A single nucleation event shifting from the cell center indicated symmetry breaking, while the asynchronous formation of two nuclei further emphasized non-equilibrium conditions at the evaporative interface. The condensed polymer at the interface exhibited hydration and dehydration dynamics, leading to pre-nuclei formation and selection influenced by capillary length and interfacial tension.

By controlling dispersion drying conditions, characteristic polymer deposition through solvent evaporation was clarified, resembling small-molecule crystal growth. This approach led to the successful preparation of a chitosan membrane with a three-dimensionally ordered structure using meniscus splitting. The membrane functioned as a hydrogel with an anisotropic pH response across a broad pH range (2.2–8.0). Structural anisotropy, confirmed via polarized optical microscopy and SEM, directly affected swelling behavior in aqueous environments.

Through in situ hydrogen bonding crosslinking, the swelling ratio was three-dimensionally regulated under acidic and alkaline conditions, strongly influenced by acidic pH. This behavior can be exploited for pH-responsive applications, including mass transporters, tissue engineering, and wound dressing materials. The anisotropic pH response of chitosan networks under physiological conditions holds potential for biomedical applications, particularly in skin regeneration and cancer-responsive drug delivery systems.

Topics for further research

1. Optimization of Evaporation-Controlled Membrane Fabrication
    - Future studies can refine the solvent evaporation process by varying environmental parameters such as temperature, humidity, and airflow.
    - Investigating the role of different polymer concentrations and cell geometries may allow for enhanced control over membrane morphology and structural anisotropy.
2. Expansion of pH-Responsive Applications
    - The anisotropic pH response observed in the chitosan membrane suggests potential for smart materials that adapt to environmental stimuli.

- Further research could explore how these membranes function in real-world conditions, such as in drug delivery, biosensors, and responsive coatings.

3. Integration with Advanced Technologies
    - The prepared chitosan membranes could be combined with nanomaterials or bioactive compounds to enhance their functionality.
    - Potential applications in smart drug carriers or cancer-responsive hydrogels could be explored by integrating functional nanoparticles or enzymes.
4. Environmental and Sustainable Material Development
    - Given the biocompatibility and biodegradability of chitosan, its applications in eco-friendly packaging, water purification, or agricultural materials warrant further study.
    - Research on alternative crosslinking methods that minimize the use of chemical reagents could enhance sustainability.

List of Accomplishments

Publications in peer-reviewed Scientific journals

1. Nguyen, T. K. L.; Okeyoshi, K, et al. Time course changes of interface positions of polymer solution in meniscus splitting. In Preparation.

2. Nguyen, T. K. L.; Hatta, T.; Ogura, K.; Tonomura, Y.; Okeyoshi, K. Symmetry breaking in meniscus splitting: Effects of boundary conditions and polymeric membrane growth. *Adv. Sci*. **2025**, *12*, e03807.

3. Nguyen, T. K. L.; Tonomura, Y.; Ito, N.; Yamaji, A.; Matsuba, G.; Hara, M.; Ikemoto, Y.; Okeyoshi, K. Reconstruction of chitosan network orders using the meniscus splitting method for designing pH-responsive materials. *Langmuir* **2024**, *40*, 11927−11935.

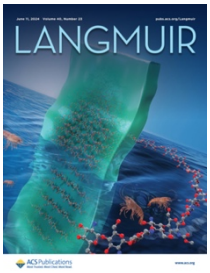

Publications in non-peer-reviewed Scientific journals

Nguyen, T. K. L.; Ikemoto, Y.; Okeyoshi, K. Reconstruction of chitosan network orders using the meniscus splitting method for design of pH-responsive materials. *SPring-8/SACLA Research Frontiers 2024*. Accepted.

International Conferences

1. Nguyen, T. K. L.; Ito, N.; Okeyoshi, K. Anisotropic pH-responsive chitosan hydrogels prepared by meniscus splitting method. *International Symposium on Exponential Biomedical DX 2024 (eMEDX-24)*, December 19th, 2024, Ishikawa, Japan – Poster.

2. Nguyen, T. K. L.; Ito, N.; Okeyoshi, K. Anisotropic pH-responsive chitosan hydrogels prepared by meniscus splitting method. *14th International Gel Symposium*, November 20th, 2024, Okinawa, Japan – Poster.

3. Nguyen, T. K. L.; Okeyoshi, K. Microstructures of anisotropic pH-responsive chitosan hydrogels

prepared by meniscus splitting method. *Materials Research Society*, April 22nd, 2024, Seattle, Washington – Oral.

4. Nguyen, T. K. L.; Ogura, K.; Okeyoshi, K. Preparation of anisotropic of pH-responsive chitosan hydrogels by meniscus splitting method. *The 13th SPSJ International Polymer Conference (IPC 2023)*, July 20th, 2023, Sapporo Convention Center – Hokkaido – Oral.

Domestic Conferences

1. Nguyen, T. K. L.; Ogura, K.; Katsushima, Y.; Okeyoshi, K. Statistical analysis of meniscus splitting and preparation of chitosan-oriented hydrogels. *JST 創発自発的な融合の場第 1 回分子生命反応創発討論会*, February 21st, 2023, Kanazawa University – Poster.

2. Nguyen, T. K. L.; Okeyoshi, K. Preparation of pH-responsive chitosan hydrogels by meniscus splitting method. *72nd Symposium on Macromolecules*, September 26th, 2023, Kagawa University – Oral.

Others (2019. 12 – 2022. 09) Master Propram

1. Nguyen, T. H.; Le, T. N. H.; Nguyen, T. B. T.; Nguyen, T. K. L.; Nguyen, T. N. U.; Vu, N. A. Green synthesis of well-dissolved high-stable silver nanoparticles using hydroxypropylmethyl cellulose as a protective agent. *Science & Technology Development Journal: Natural Sciences*, University of Science, Viet Nam National University Ho Chi Minh City, **2022**, *6*(3), 2181-2192.

2. Nguyen, T. K. L.; Ogura, K.; Katsushima, Y.; Okeyoshi, K. Statistical analysis of meniscus splitting and preparation of chitosan-oriented hydrogels. *13th International Gel Symposium*, September 3rd, 2022, Tomamu – Hokkaido – Poster.

3. Vu, N. A.; Cao, T. H. L.; Nguyen, H. L.; Le, T. T. P.; Nguyen, T. N. U.; Le, V. H.; Nguyen, T. K. L. "Research and fabrication of Chitosan/CNC/TiO2 composite membrane for application in water treatment", *The 12th Scientific Conference of University of Science, Viet Nam National University Ho Chi Minh City*, 2022, Vietnam – Poster.

4. Vu, N. A.; Le, T. T. P.; Nguyen, T. K. L, Bui, K. N.; Tu, T. K. P.; Nguyen, T. N. U. "Fabrication of chitosan/nanocrystalline cellulose/silver biocomposite films with application in environmental remediation", *The 12th Scientific Conference of University of Science, Viet Nam National University Ho Chi Minh City*, 2022, Vietnam – Poster.

5. Nguyen, T. K. L.; Nguyen, T. N. U. "Fabrication of chitosan/nanocellulose membrane containing curcumin by freeze-gelation technique for wound dressing application", *The 12th Scientific Conference of University of Science, Viet Nam National University Ho Chi Minh City*, 2022, Vietnam – Oral.